

EXPERIMENTAL TECHNIQUES

Tejinder S. VIRDEE

EP Division, CERN, 1211 Geneva 23, Switzerland and

Imperial College of Science Technology and Medicine, London SW7 2BZ, U.K.

Abstract

Experimental techniques used in high energy physics experiments are described. Emphasis has been placed on the techniques to be used in the pp experiments at the Large Hadron Collider. The physics underlying the working of some key detectors is outlined. Factors determining the measurement accuracy attainable with these detectors are discussed. The reasoning behind the designs of the ATLAS and CMS experiments is discussed.

1. INTRODUCTION

The aim of Particle Physics is to answer the two following questions: What are the fundamental constituents of matter? What are the fundamental forces that control their behaviour at the most basic level? Experimentally this involves study of hard particle interactions, determining the identity of the resulting particles and measuring their momenta with as high a precision as possible. Some thirty years ago a single detection device, the bubble chamber, was sufficient to reconstruct the full event information. At the current high centre of mass energies no single detector can accomplish this even though the number of particles whose identity and momenta can be usefully determined is limited [electrons, muons, photons, jets, b-jets, taus and missing transverse energy $E_t(\nu)$]. This leads to a familiar onion-like structure of present day high energy physics experiments. Each layer is specialized to measure and identify different classes of particles.

Starting from the interaction vertex the momenta of charged particles is determined in the inner tracker which is usually immersed in a solenoidal magnetic field. Identification of b-jets can be accomplished by placing high spatial resolution detectors such as silicon pixel or microstrip detectors close to the interaction point. Following the tracking detectors are calorimeters which measure the energies and identify electrons, photons, single hadrons or jets of hadrons. Only muons and neutrinos penetrate through the calorimeters. The muons are identified and measured in the outermost sub-detector, the muon system which is usually immersed in a magnetic field. The presence of neutrinos is deduced from the apparent imbalance of transverse momentum or energy.

These lectures rely heavily on previous literature [1-9]. The emphasis is placed on their use at the future Large Hadron Collider. Hence illustrative examples from ATLAS and CMS are used. These examples are described in detail in Technical Design Reports of various sub-detectors [10,11]. Examples will also be taken from some of the many other experiments, planned or ongoing, using novel techniques.

2. INTERACTION WITH MATTER

2.1 Energy Loss by Charged Particles

Moderately relativistic charged particles, other than electrons, lose energy in matter through the Coulomb interaction with the atomic electrons. The energy transferred to the electrons causes them either to be ejected from the parent atom (*ionisation*) or to be excited to a higher level (*excitation*). The energy loss is given by the Bethe-Bloch equation :

$$-\frac{dE}{dx}\Big|_{ion} = N_A \frac{Z}{A} \frac{4\pi\alpha^2(\hbar c)^2}{m_e c^2} \frac{Z_i^2}{\beta^2} \left[\ln \frac{2m_e c^2 \gamma^2 \beta^2}{I} - \beta^2 - \frac{\delta}{2} \right] \quad (1)$$

where E is the kinetic energy of the incident particle with velocity β and charge Z_i , I ($\approx 10 \times Z$ eV) is the mean ionization potential in a medium with atomic number Z . The notable features of this formula are:

- $1/m_e \Rightarrow$ energy is lost essentially to electrons
- $1/\beta^2 \Rightarrow$ slower particles lose more energy. The slower particles have a longer time in the vicinity of atomic electrons during which to interact.
- at low β the increase in energy loss does not continue down to $\beta = 0$. In a head-on collision the electron can acquire an energy $2m\gamma^2$. If this is insufficient to excite electrons to higher states then the particle cannot lose energy. If $I \approx 2m\gamma^2$ then the 1st term $\rightarrow 0$.
- energy loss is $\propto Z_i^2$
- the energy loss minimum occurs at $\beta\gamma \approx 4$ (said to be minimum ionizing particles or mips)
- relativistic rise – the relativistic expansion of the electric field means that for relativistic particles interaction with electrons further and further away is possible. The relativistic rise does not continue forever as the polarization of the medium starts screening electrons in the more distant atoms.

A very useful quantity is *areal density* measured in units of g.cm^{-2} . The energy loss of relativistic particles of unit electric charge per unit areal density is found to be roughly the same in all materials with

$$\frac{1}{\rho} \frac{dE}{dx} \approx 1.5 - 2 \frac{\text{MeV}}{\text{g.cm}^{-2}}$$

where ρ is the density of the medium. The energy loss rate in liquid hydrogen, gaseous helium, carbon, aluminium, tin and lead is shown in Fig. 1 [4]. It can be seen that the above approximation is valid for all solids.

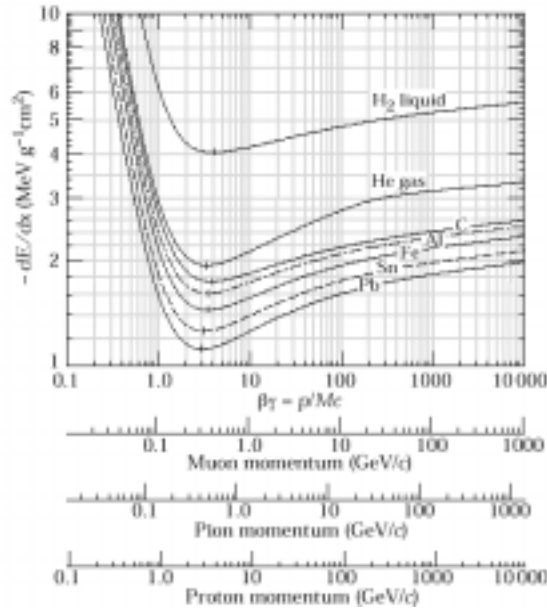


Figure 1: Energy loss rate in liquid hydrogen, gaseous helium, carbon, aluminium, tin and lead.

2.2 Energy Loss by Electrons

Above about 1 GeV radiative processes dominate energy loss by electrons and photons. In the intense electric field of nuclei relativistic electrons radiate photons (*bremstrahlung*), and photons can be converted into electron-positron pairs (*pair creation*).

In dealing with electrons and photons at high energies striking blocks of material (e.g. calorimeters) it is convenient to measure the depth and radial extent of the resulting cascades in terms of *radiation length* (X_0) and *Molière radius* (R_M).

Consider the process of bremsstrahlung. A free electron cannot radiate a photon. However a charged particle emits radiation when it is subjected to acceleration or deceleration. For a given force the acceleration/deceleration is greater the lighter the particle. The Feynman diagram for the bremsstrahlung process is shown in Figure 2. The cross section for the process comprises the coupling constant at the three vertices and the propagator term ($\propto 1/m^2$)

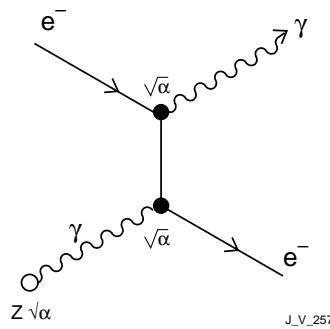


Figure 2: The Feynman diagram for bremsstrahlung

$$\sigma \propto \frac{Z^2 \alpha^3}{m_e^2 c^4}$$

We are interested in $d\sigma/dv$ where v is the energy of the emitted photon. We can make a guess for the expression using dimensional arguments:

$$\frac{d\sigma}{dv} \propto \frac{Z^2 \alpha^3}{m_e^2 c^4} \frac{(\hbar c)^2}{v}$$

Turning this to energy loss per unit distance traversed by the electrons gives

$$-\frac{d\sigma}{dx}|_{rad} = n \int_{v_{min}}^{v_{max}} v \frac{d\sigma}{dv} dv = n \frac{Z^2 \alpha^3 (\hbar c)^2}{m_e^2 c^4} (v_{max} - v_{min})$$

where v_{max} = kinetic energy of electron, $v_{min} \approx 0$ and n is no. of nuclei/unit volume. A numerical factor $[4 \ln(183/Z^{1/3})]$ has to be added describing the effect of the possible range of impact parameters of the electron. At large impact parameters the protons are shielded by atomic electrons. Hence

$$-\frac{dE}{dx}\Big|_{rad} = \left[4n \frac{Z^2 \alpha^3 (\hbar c)^2}{m_e^2 c^4} \ln \frac{183}{Z^{1/3}} \right] E$$

Since $-\frac{dE}{dx} \propto E \Rightarrow \frac{dE}{E} = -B dx \Rightarrow E = E_0 e^{-Bx}$ where A is a constant.

The *radiation length* is defined to be the distance over which the electron loses, on average, all but 1/e of its energy i.e. $X_0 = 1/B$ i.e.

$$X_0 = \left[4n \frac{Z^2 \alpha^3 (\hbar c)^2}{m_e^2 c^4} \ln \frac{183}{Z^{1/3}} \right]^{-1}$$

Infact for Pb, $Z = 82$, $n = 3.3 \cdot 10^{28}$ nuclei/m³, $X_0 \approx 5.3$ mm which is close to the PDG [4] value of 5.6 mm. The radiation length can be approximated as $X_0 \approx \frac{180A}{Z^2} \text{ g.cm}^{-2}$ where A is the mass number

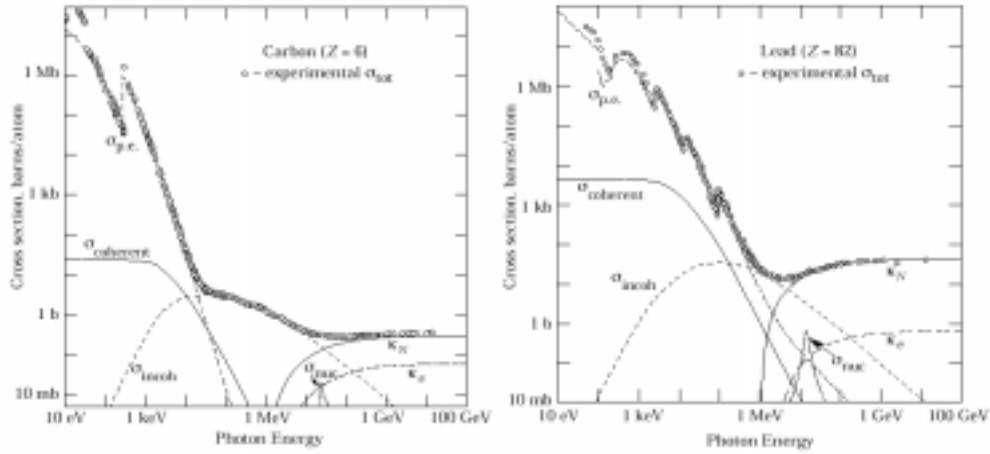


Figure 3: The photon total cross-sections as a function of energy in carbon and lead.

2.3 Energy Loss by Photons

Photons lose energy through photoelectric effect and Compton scattering at low energies and by pair production at relativistic energies. The cross-section for photoelectric effect is given by

$$\sigma_{pe} \approx Z^5 \alpha^4 \left(\frac{m_e c^2}{E_\gamma} \right)^n \quad n = \frac{7}{2} \text{ at } E_\gamma \ll m_e c^2 \text{ and } n \rightarrow 1 \text{ at } E_\gamma \gg m_e c^2$$

with a strong dependence on Z. The cross-section for Compton scattering has been calculated by Klein and Nishina :

$$\sigma_C \approx \frac{\ln E_\gamma}{E_\gamma} \text{ per electron and } \sigma_C^{atom} = Z \sigma_C \text{ per atom}$$

If the energy of the photon is $\gg m_e c^2$ then the dominant energy loss mechanism is pair production and its probability can be deduced, as done in Equation (1) for bremsstrahlung. It is given by:

$$\sigma_{pair} \approx \frac{7}{9} \frac{A}{N_A} \frac{1}{X_0}$$

The probability of a pair conversion in 1 X_0 is $e^{-7/9}$. Since the photon disappears on producing a pair a mean free path length can be defined as

$$L_{pair} = \frac{9}{7} X_0 \text{ independent of energy.}$$

The photon total cross-sections as a function of energy in carbon and lead are shown in Figure 3 [4] which shows the above mentioned dependences.

2.3.1 Critical Energy and Molière Radius

The *critical energy*, ϵ , is defined to be the energy at which the energy loss due to ionisation (at its minimum i.e. at $\beta \approx 0.96$) and radiation are equal (over many trials) i.e.

$$\frac{(dE/dx)_{rad}}{(dE/dx)_{ion}} = \frac{Z\alpha}{\pi m_e c^2} E \beta^2 \frac{\ln 183/Z^{1/3}}{\ln \left[\frac{(2m_e c^2 \beta^2)}{I(1-\beta^2)} \right] - \beta^2} = 1$$

which simplifies to

$$\Rightarrow \epsilon \approx \frac{560}{Z} \text{ (MeV)}$$

The Molière radius gives the average lateral deflection of critical energy electrons after traversal of 1 X_0 and is parameterized as:

$$R_M = \frac{21_{MeV} X_0}{\epsilon} \approx \frac{7A}{Z} \text{ g.cm}^{-2}$$

Table 1: Physical properties of some materials used in calorimeters.

	Z	ρ g.cm ⁻³	I/Z eV	(1/ ρ)dT/dx MeV/g.cm ⁻³	ϵ MeV	X_0 cm	λ_{int} cm
C	6	2.2	12.3	1.85	103	≈ 19	38.1
Al	13	2.7	12.3	1.63	47	8.9	39.4
Fe	26	7.87	10.7	1.49	24	1.76	16.8
Cu	29	8.96		1.40	≈ 20	1.43	15.1
W	74	19.3		1.14	≈ 8.1	0.35	9.6
Pb	82	11.35	10.0	1.14	6.9	0.56	17.1
U	92	18.7	9.56	1.10	6.2	0.32	10.5

2.4 Hadronic Interactions

A high energy hadron striking an absorber interacts with nuclei resulting in multi-particle production consisting of secondary hadrons (e.g. π^\pm , π^0 , K etc.). A simple model treats the nucleus, mass number A, as a black disc with radius R. Then

$$\sigma_{\text{int}} = \pi R^2 \propto A^{2/3} \quad \text{where } R \approx 1.2 \times A^{1/3} \text{ fm}$$

$$\text{infact } \sigma_{\text{inel}} = \sigma_0 A^{0.7} \quad \text{where } \sigma_0 = 35 \text{ mb}$$

In dealing with hadrons it is convenient to measure the depth and radial extent of the resulting cascades in terms of *interaction length* (λ_{int}) which is defined as

$$\lambda_{\text{int}} = \frac{A}{N_A \sigma_{\text{int}}} \propto A^{1/3}$$

The values of the above mentioned parameters for various materials are listed in Table. 1.

3. EXPERIMENTAL MEASUREMENTS: MEASUREMENT OF MOMENTUM

Consider the motion of a charged particle in a uniform solenoidal magnetic field (Fig.4). The radius of curvature, r , is given by:

$$r = \frac{p_T}{0.3B}$$

where r is measured in m, B is the magnetic field strength measured in T and p_T is the momentum perpendicular to B and measured in GeV/c.

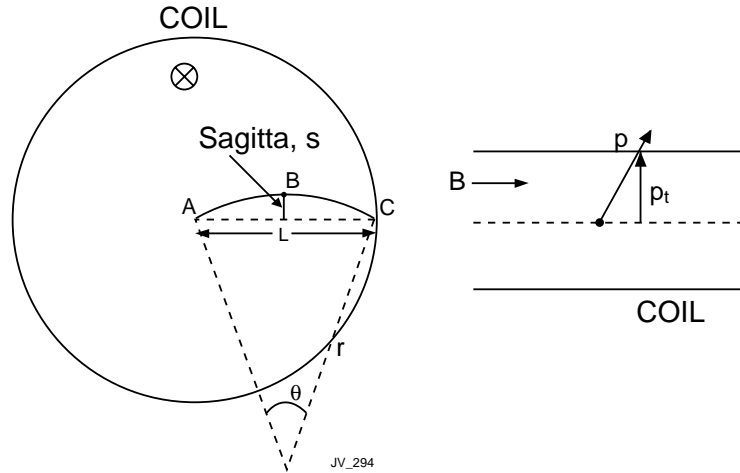


Figure 4: The trajectory of a charged particles in a magnetic field.

The angle θ is given by

$$\sin \frac{\theta}{2} = \frac{L}{2r}$$

If $r \gg L$ then

$$\frac{\theta}{2} \approx \frac{L}{2r} \Rightarrow \theta \approx \frac{0.3BL}{p_T}$$

Therefore the sagitta, s , is given by

$$\begin{aligned}
s &= r - r \cos(\theta/2) \\
&\approx r \left[1 - \left(1 - \frac{1}{2} \frac{\theta^2}{4} \right) \right] \\
&= \frac{r\theta^2}{8} \approx \frac{0.3BL^2}{8p_T}
\end{aligned}$$

As an example $s \approx 3.75$ cm for $p_T=1$ GeV/c, $L=1$ m and $B=1$ T. Suppose the sagitta is measured using points A, B and C. Then

$$\begin{aligned}
s &= x_B - \frac{x_A + x_C}{2} \\
\therefore ds &= dx_B - \frac{dx_A}{2} - \frac{dx_C}{2} \\
&\text{assuming } dx_i \approx \sigma(x) \text{ is the independent single point error} \\
(ds)^2 &= \sigma^2(x) + \frac{\sigma^2(x)}{4} + \frac{\sigma^2(x)}{4} = \frac{3}{2} \sigma^2(x) \equiv \sigma_s^2
\end{aligned}$$

where σ_s is the error on the sagitta. The relative momentum resolution can now be estimated as:

$$\begin{aligned}
\frac{dp_T}{p_T} &= \frac{\sigma_s}{s} = \frac{\sqrt{(3/2)} \sigma_x}{s} \\
\frac{dp_T}{p_T} &= \frac{\sqrt{3}}{2} \sigma_x \frac{8p_T}{0.3BL^2} \quad (2)
\end{aligned}$$

Hence the momentum resolution will degrade linearly with increasing p_T but will improve for higher field and larger radial size of the tracking cavity. The latter improvement is quadratic in L ! The next question that can be asked is the arrangement of N measuring points. Uniform spacing is best for minimizing the effect of multiple scattering (see 3.1.2) and the resolution is given by

$$\frac{dp_T}{p_T} = \frac{\sigma_x p_T}{0.3BL^2} \sqrt{\frac{720}{N+4}}$$

For example, $dp_T/p_T \approx 0.5\%$ for $p_T = 1$ GeV/c, $L = 1$ m, $B = 1$ T, $\sigma_x = 200$ μm and $N=10$. For the best momentum resolution $N/2$ points should be grouped at the centre and $N/4$ points at the two ends of the track. Then

$$\frac{dp_T}{p_T} = \frac{\sigma_x p_T}{0.3BL^2} \sqrt{\frac{256}{N}}$$

leading to an improvement in the momentum resolution by a factor of 0.6.

However in a real tracker the errors due to multiple scattering need to be included.

3.1 Multiple Scattering

The electric field close to an atomic nucleus may give a large acceleration to a charged particle. This will result in a change of direction for a heavy charged particle ($m > m_e$). For small particle-

nucleus impact parameters a single large angle scatter is possible. This is described by Rutherford scattering and the angle θ is given by

$$\frac{d\sigma}{d\Omega} \propto \frac{1}{\sin^4 \theta/2}$$

Larger impact parameters are more probable and the scattering angle will be smaller as the nuclear charge is partly screened by the atomic electrons. Hence in a relatively thick material there will be a large number of random and small deflections. This is described by multiple Coulomb scattering. The relative probability of scattering as a function of scattering angle is illustrated in Fig. 5.

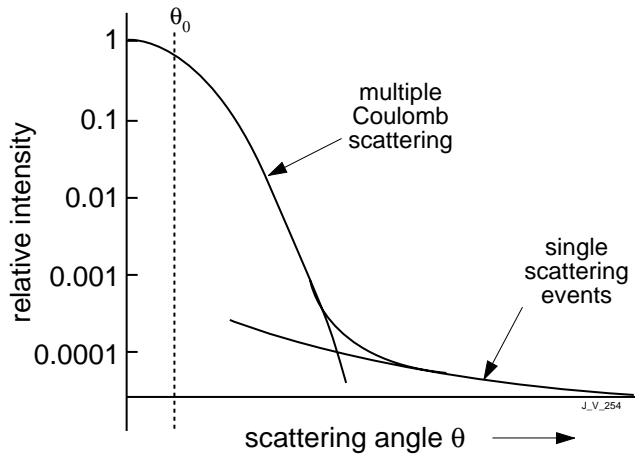


Figure 5: The relative probability of scattering as a function of scattering angle.

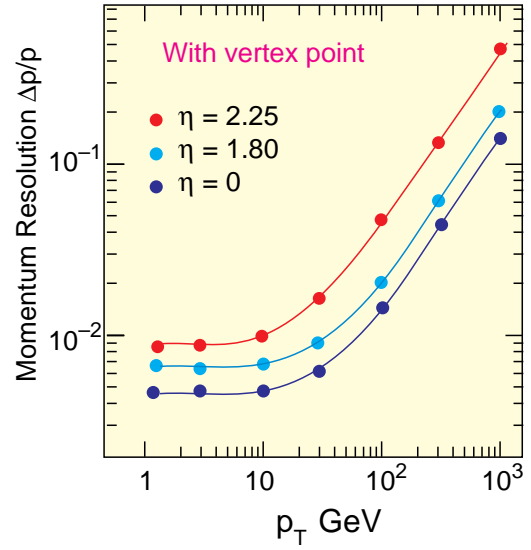


Figure 6: The estimated momentum resolution In CMS as a function of p_T at various η .

The r.m.s. of the scattering angle is given by

$$\theta_0 \approx \frac{13.6 \text{ MeV}}{\beta p c} Z_{inc} \sqrt{\frac{L}{X_0}}$$

where L is the thickness of the material in the tracker and X_0 is the radiation length of the material, Both are measured in m. The apparent sagitta due to multiple scattering is given by

$$s_{ms} = \frac{L\theta_0}{4\sqrt{3}}$$

If the extrapolation error from one measuring plane to the next is larger than the point resolution, i.e. $\theta_0 \Delta r > \sigma_x$, then the momentum resolution will be degraded. The relative momentum resolution due to multiple scattering is then given by

$$\frac{s_{ms}}{s} = \frac{dp}{p} \Big|_{ms} \approx 0.05 \frac{1}{B\sqrt{LX_0}} \quad \text{since } s = \frac{0.3BL^2}{8p} \quad (3)$$

Hence the relative momentum resolution is independent of p and is proportional to $1/B$. For example $dp/p \approx 0.5\%$ for argon gas with $L=1\text{m}$ and $B=1\text{T}$. The estimated momentum resolution

in CMS is illustrated in Fig. 6. The momentum resolution is independent of momentum in the range where the multiple scattering error dominates (up to ≈ 20 GeV/c). The resolution, $\Delta p/p$, above 20 GeV/c is proportional to p .

4 MEASUREMENT OF ENERGY

Neutral and charged particles incident on a block of material deposit their energy through creation and destruction processes. The deposited energy is rendered measurable by ionisation or excitation of the atoms of matter in the active medium. The active medium can be the block itself (*totally active or homogeneous calorimeter*) or a sandwich of dense absorber and light active planes (*sampling calorimeter*). The measurable signal is usually linearly proportional to the incident energy.

An example of the phenomena (bremsstrahlung and pair production) involved in electromagnetic showers is illustrated in Fig. 7 in which a 50 GeV electron is incident on the BEBC Ne/H₂ (70%/30%) bubble chamber in a 3 T magnetic field.

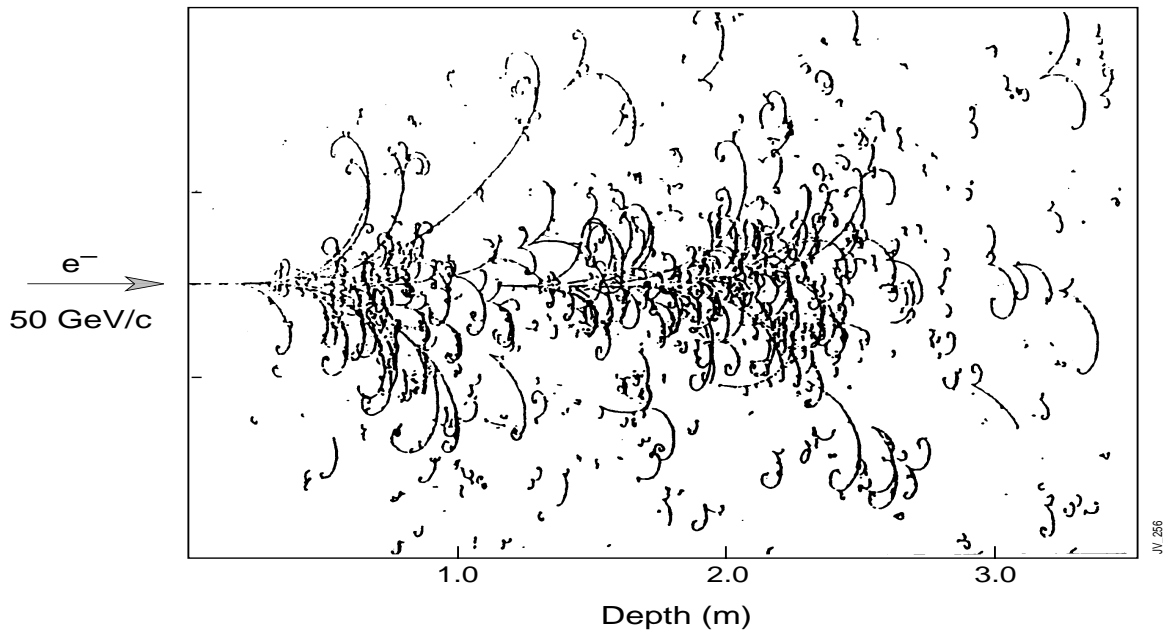


Figure 7: An example of a 50 GeV electron shower in a Ne/H₂ (70%/30) filled BEBC bubble chamber. The radiation length is ≈ 34 cm.

4.1 The Electromagnetic Cascade

4.1.1 Longitudinal Development of the Electromagnetic Cascade

A high energy electron or photon incident on a thick absorber initiates a cascade of secondary electrons and photons via bremsstrahlung and pair production as illustrated in Fig. 8. With increasing depth the number of secondary particles increases while their mean energy decreases. The multiplication continues until the energies fall below the critical energy, ϵ . Ionization and excitation rather than generation of more shower particles dominate further dissipation of energy.

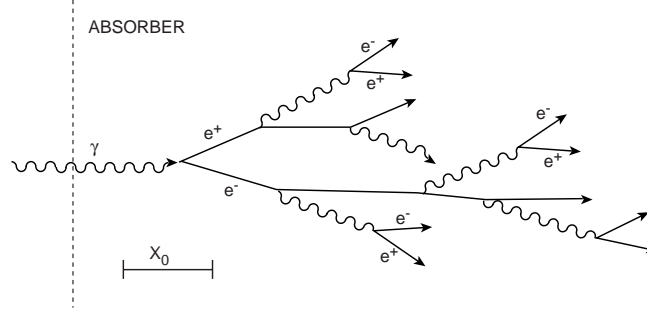


Figure 8: Schematic development of an electromagnetic shower.

Consider a simplified model of development of an electromagnetic shower initiated by an electron or a photon of an energy E . A universal description, independent of material, can be obtained if the development is described in terms of scaled variables

$$t = \frac{x}{X_0} \quad \text{and} \quad y = \frac{E}{\varepsilon}$$

Since in $1 X_0$ an electron loses about $2/3^{\text{rd}}$ of its energy and a high energy photon has a probability of $7/9$ of pair conversion, we can naively take $1 X_0$ as a generation length. In each generation the number of particles increases by a factor of 2. After t generations the energy and number of particles is

$$e(t) = \frac{E}{2^t} \quad \text{and} \quad n(t) = 2^t \quad \text{respectively.}$$

At shower maximum where $e \approx \varepsilon$, the no. of particles is

$$n(t_{\text{max}}) = \frac{E}{\varepsilon} = y \quad \text{and} \quad t_{\text{max}} = \ln \frac{E}{\varepsilon} = \ln y$$

Critical energy electrons do not travel far ($\leq 1X_0$). After the shower maximum the remaining energy of the cascade is carried forward by photons giving the typical exponential falloff of energy deposition caused by the attenuation of photons. Longitudinal development of 10 GeV showers in Al, Fe and Pb is shown in Fig. 9 [12]. It can be noted that the shower maximum is deeper for higher Z materials because multiplication continues down to lower energies. The slower decay beyond the maximum is due to the lower energies at which electrons can still radiate. Both of the above effects are due to lower ε for higher Z materials.

The mean longitudinal profile of energy deposition is given by:

$$\frac{dE}{dt} = Eb \frac{(bt)^{a-1} e^{-bt}}{\Gamma(a)}$$

The maximum of the shower occurs at $t_{\text{max}} = (a-1)/b$. Fits to t_{max} give

$$t_{\text{max}} = \ln y - 0.5 \quad \text{for electron-induced cascades and}$$

$$t_{\text{max}} = \ln y + 0.5 \quad \text{for photon-induced cascades.}$$

The coefficient a can be found using t_{max} and assuming $b \approx 0.5$. The photon induced showers are longer since the energy deposition only starts after the first pair conversion has taken place. The mean free path length for pair conversion of a high energy photon is $X_\gamma = (9/7) X_0$.

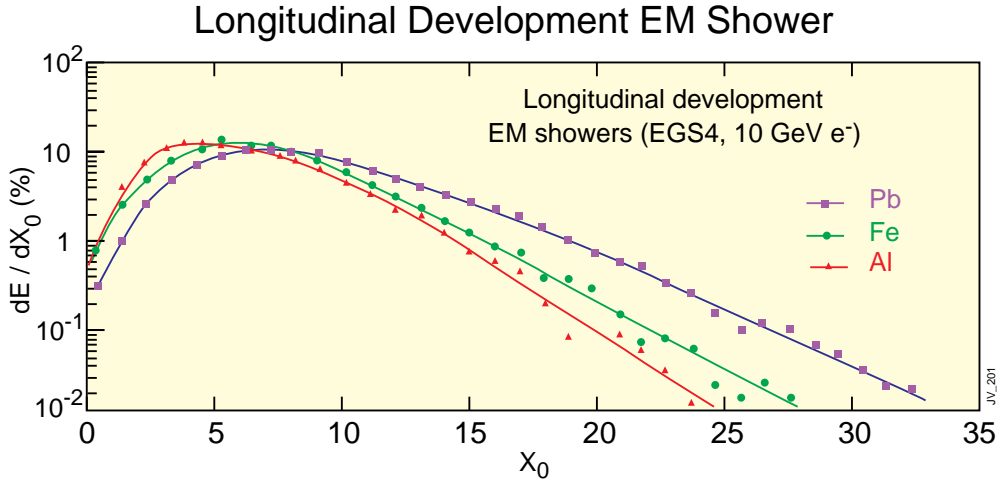


Figure 9: Simulation of longitudinal development of 10 GeV electron showers in Al, Fe and Pb.

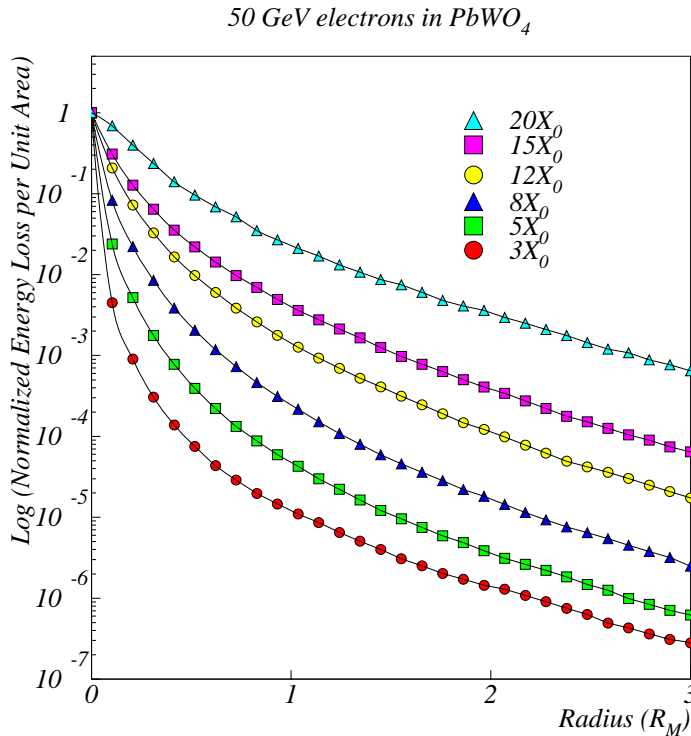


Figure 10: Lateral profile of energy deposition by 50 GeV electrons showers in PbWO_4 at various depths.

4.1.2 Lateral Development of the Electromagnetic Cascade

The lateral spread of an e.m. shower is determined by multiple scattering of electrons away from the shower axis. Also responsible are low energy photons which deposit their energy a long way away from their point of emission, especially when emitted from electrons that already travel at large angles with respect to the shower axis. The e.m. shower begins, and persists, with a narrow core of high energy cascade particles, surrounded by a halo of soft particles which scatter increasingly as the shower depth increases. This is shown in Fig. 10 for 50 GeV electrons incident on lead tungstate [13]. In different materials the lateral extent of e.m. showers scales fairly accurately with the Molière radius. An infinite cylinder with a radius of $\approx 1 R_M$ contains $\approx 90\%$ of

the shower energy. For lead tungstate, and a depth of $26 X_0$, the amount of energy contained in a cylinder of a given radius is shown in Fig. 11. The fact that e.m. showers are very narrow at the start can be used to distinguish single photons from pizeros (see Section 6.6.2).

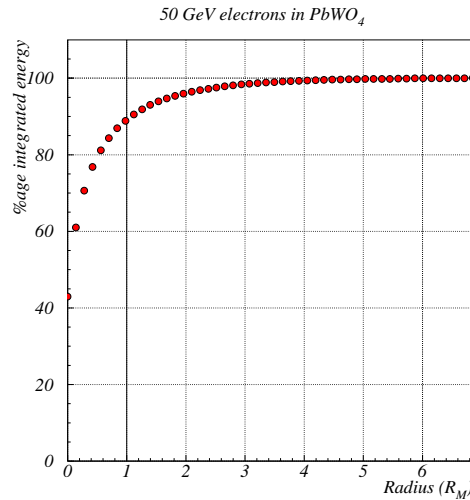


Figure 11: The percentage of energy contained in a cylinder of lead tungstate of different radii.

4.2 The Hadronic Cascade

4.2.1 The Longitudinal Development of the Hadronic Cascade

A situation analagous to that for e.m. showers exists for hadronic showers. The interaction responsible for shower development is the strong interaction rather than electromagnetic. The interaction of the incoming hadron with absorber nuclei leads to multiparticle production. The secondary hadrons in turn interact with further nuclei leading to a growth in the number of particles in the cascade. Nuclei may breakup leading to spallation products. The cascade contains two distinct components namely the electromagnetic one (π^0 's etc.) and the hadronic one (π^\pm , n, etc) one. This is illustrated in Fig. 12.

The multiplication continues until pion production threshold is reached. The average number, n , of secondary hadrons produced in nuclear interactions is given by $n \propto \ln E$ and grows logarithmically. The secondaries are produced with a limited transverse momentum of the order of 300 MeV.

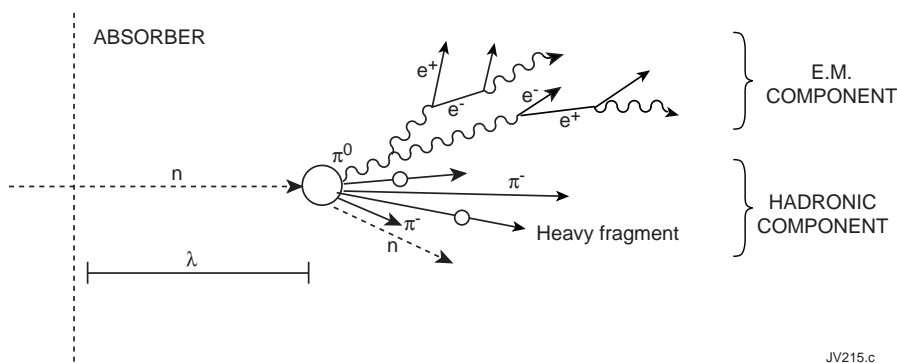


Figure 12: Schematic of development of hadronic showers.

It is convenient to describe the average hadronic shower development using scaled variables

$$v = x/\lambda \quad \text{and} \quad E_{th} \approx 2m_\pi = 0.28 \text{ GeV}$$

where λ is the nuclear interaction length and is the scale appropriate for longitudinal and lateral

development of hadronic showers. The generation length can be taken to be λ . Note $\lambda \approx 35 \text{ A}^{1/3} \text{ g.cm}^{-2}$. Furthermore, if it is assumed that $\langle n \rangle$ secondaries/primary are produced for each generation and that the cascade continues until no more pions can be produced. Then in generation v

$$e(v) = \frac{E}{\langle n \rangle^v}$$

$$e(v_{\max}) = E_{th} \quad \therefore E_{th} = \frac{E}{\langle n \rangle^{v_{\max}}}$$

$$n^{v_{\max}} = \frac{E}{E_{th}} \Rightarrow v_{\max} = \ln(E/E_{th})/\ln\langle n \rangle$$

The number of independent particles in the hadronic cascades compared to electromagnetic ones is smaller by E_{th}/ϵ and hence the intrinsic energy resolution will be worse at least by a factor $\sqrt[3]{(E_{th}/\epsilon)} \approx 6$. The average longitudinal energy deposition profiles are characterised by a sharp peak near the first interaction point (from π^0 s) followed by an exponential fall-off with scale λ . This is illustrated in Fig. 13. The maximum occurs at $t_{\max} \approx 0.2 \ln E + 0.7$ (E in GeV).

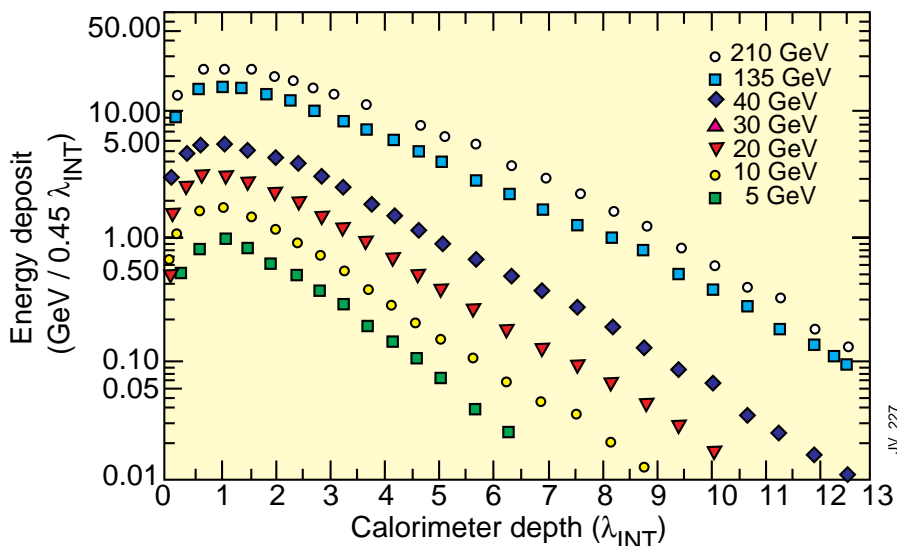


Figure 13: longitudinal profile of energy deposition for pion showers of different energies.

A parameterisation for the depth required for almost full containment (95%) is given by $L_{0.95}(\lambda) \approx t_{\max} + 2\lambda_{att}$ where $\lambda_{att} \approx \lambda E^{0.13}$. Fig. 13 shows that over 9λ are required to contain almost all the energy of high energy hadrons. However there is a considerable variation from one hadronic shower to another as illustrated in Fig. 14 [13]. The peaks arise from energy deposited locally by π^0 s produced in the interactions of charged hadrons. These interactions take place at differing depths from shower to shower. The energy carried by π^0 s also varies considerably from shower to shower.

4.2.2 The Lateral Development of the Hadronic Cascade

The secondary hadrons are produced typically with $\langle p_t \rangle \approx 300 \text{ MeV}$. This is comparable to the energy lost in 1λ in most materials. At shower maximum, where the mean energy of the particles is $E_{th} \approx 280 \text{ MeV}$, the radial extent will have a characteristic scale of $R_\pi \approx \lambda$. High energy hadronic showers show a pronounced core, caused by the π^0 component with a characteristic transverse scale of R_M , surrounded by an exponentially decreasing halo with scale λ . This is illustrated in Figure 12 for a lead/scintillating fibre calorimeter [14].

270 GeV Incident Pions in Copper

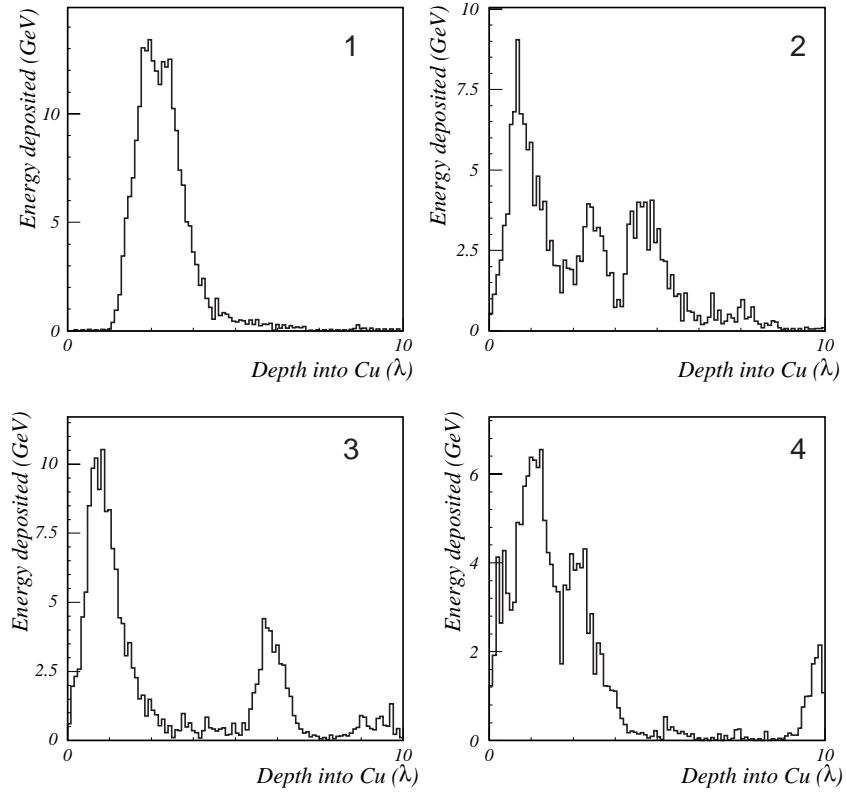


Figure 14: A simulation of the development of four representative pion showers in a block of copper.

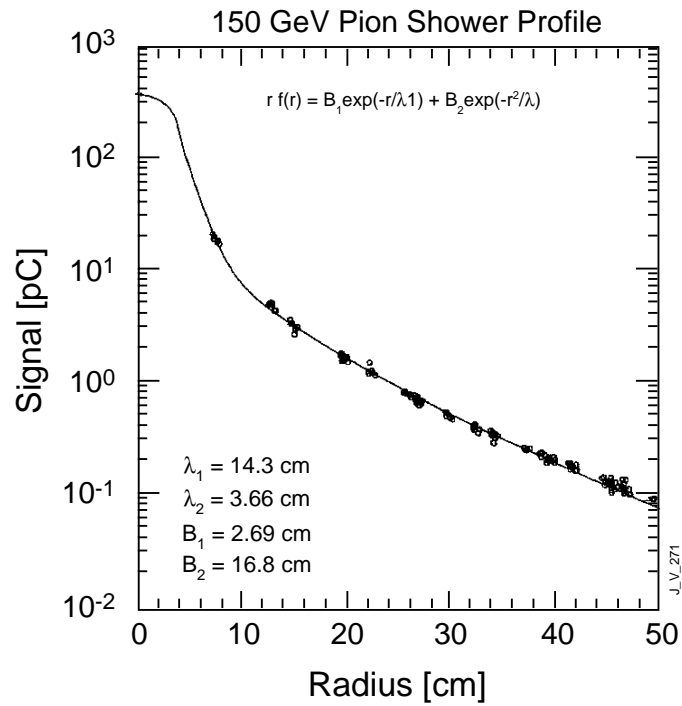


Figure 15: The lateral profile of energy deposition of pion showers.

5. ENERGY RESOLUTION

The energy resolution of calorimeters is usually parameterised as :

$$\frac{\sigma}{E} = \frac{a}{\sqrt{E}} \otimes \frac{b}{E} \otimes c$$

where the r.h.s. is the square root of the quadratic sum of the three terms.

The first term, with coefficient a , is the *stochastic or sampling* term and accounts for the statistical fluctuation in the number of primary and independent signal generating processes, or any further process that limits this number. An example of the latter is the conversion of light into photo-electrons by a photo-device.

The second term, with coefficient b , is the *noise* term and includes:

- the energy equivalent of the electronics noise and
- the fluctuation in energy carried by particles, other than the one(s) of interest, entering the measurement area. This is usually labeled pileup.

The last term, with coefficient c , is the *constant* term and accounts for:

- imperfect quality of construction of the calorimeter
- non-uniformity of signal generation and/or collection
- cell-to-cell inter-calibration error
- the fluctuation in the amount of energy leakage from the front or the rear (though somewhat increasing with energy) the volume used for the measurement of energy,
- the contribution from the fluctuation in the e.m. component in hadronic showers.

The tolerable size of the three terms depends on the energy range involved in the experiment. The above parametrisation allows the identification of the causes of resolution degradation. The quadratic summation implies that the three types of contributions are independent which may not always be the case.

5.1 Intrinsic Electromagnetic Energy Resolution

It is instructive to look at homogeneous calorimeters in which all the energy is deposited in the active medium. If the shower is fully contained then the intrinsic energy resolution is determined by the fluctuation in the number, n , of ions or photons produced. If W is the mean energy required to produce an electron-ion pair (or a photon) then $n = E/W$, and

$$\frac{\sigma}{E} = \frac{\sqrt{n}}{n} = \sqrt{\frac{W}{E}}$$

However the fluctuation is smaller as the total energy deposited (= incident energy) does not fluctuate. The improvement in resolution is characterised by the Fano factor, F , as

$$\frac{\sigma}{E} = \sqrt{F} \times \sqrt{\frac{W}{E}} = \sqrt{\frac{FW}{E}}$$

F is dependent on the nature of processes that lead to energy transfer in the detector including ones that do not lead to ionisation e.g. phonon excitations.

Consider calorimeters used for the spectroscopy of low energy (\approx MeV) gamma rays. The two commonly used detectors are inorganic scintillators (e.g. NaI) and semiconductor detectors (e.g. Ge). The energy resolution of the Ge detector is superior and is measured to be $\sigma \approx 180$ eV for photons carrying 100 keV. The above formula gives $\sigma = \sqrt{(FEW)} \approx 195$ eV where $F_{\text{Ge}}=0.13$ and $W=2.96$ eV. It should be noted that without the Fano factor $\sigma \approx 540$ eV!

Other phenomena may limit the number of signal generating events. Lead glass shower detectors are based on the detection of Cerenkov light, produced by the electrons and positrons with kinetic energies greater than ~ 0.7 MeV. This means that at most $1000 / 0.7 \sim 1400$ independent particles, per GeV of deposited energy, produce Cerenkov light. The resolution is then dominated by the fluctuation in this number and thus cannot be better than $(\sigma/E)_n \geq 3\% / \sqrt{E}$. This is further limited by photo-electron statistics as only about 1000 photo-electrons are generated when using photomultipliers to detect the scintillation light. This leads to an additional loss of resolution given by $(\sigma/E)_{pe} \approx 3\% / \sqrt{E}$.

5.2 Energy Resolution of Sampling Electromagnetic Calorimeters

When the very best energy resolution is not required, sampling calorimeters are employed. The shower energy is measured in active layers, often of low Z , sandwiched in between passive absorber layers of high Z materials. Only a fraction of the shower energy is dissipated in the active medium and the energy resolution is dominated by the fluctuation in this fraction. If the energy loss in an active layer is much smaller than that in the absorber layer then the number of independent charged particles crossing an active layer can be approximated by $n=E/\Delta E_{abs}$ where ΔE_{abs} is the energy lost by a minimum ionizing particle (m.i.p.) in the absorber layer.

Now $\Delta E_{abs} = t_{abs} \times (dE/dx)$ where t_{ab} is measured in units of X_0 . Hence

$$\frac{\sigma}{E} = \frac{\sqrt{n}}{n} \propto \frac{\sqrt{t_{abs}}}{\sqrt{E}}$$

For a fixed thickness of an active layer the energy resolution improves with decreasing absorber thickness. The above formula is not valid if the crossings between consecutive active layers are correlated, i.e. when t_{abs} is small. A generally valid formula is:

$$\frac{\sigma_s}{E} = \frac{5\%}{\sqrt{E}} (1 - f_{samp}) \Delta E_{cell}^{0.5(1-f_{samp})}$$

where ΔE_{cell} is the energy deposited in a unit sampling cell i.e. 1 active and 1 absorber layer. f_{samp} is labeled the *sampling fraction* and is the fraction of the total energy that is deposited in the active medium. As $f_{samp} \rightarrow 1$, $\sigma_s = 'a' \rightarrow 0$ (usually $a \neq 0$ due to imperfections in calorimeter systems) and as $f_{samp} \rightarrow 0$, $\sigma_s \propto \sqrt{\Delta E_{cell}} \propto \sqrt{\Delta E_{abs}}$.

The sampling fraction can be calculated as follows. If d is the thickness of active layer then

$$f_{samp} = 0.6 f_{mip} = 0.6 \frac{d \left(\frac{dE}{dx} \right)_{act}}{\left[d \left(\frac{dE}{dx} \right)_{act} + t_{abs} \left(\frac{dE}{dx} \right)_{abs} \right]}$$

$f_{mip} \approx 2/(12.75+2) \approx 13.5\%$ for a sampling calorimeter with 1cm Pb and 1cm scintillator plates

The fractional energy resolution as a function of $\sqrt{(d/f_{samp})}$ is shown in Figure 16 [5]. Clearly the energy resolution of gas calorimeters will be poor as the sampling fraction tends to be very low.

5.3 Energy Resolution of Hadronic Calorimeters

Hadronic calorimeters, because of the large depth required ($\approx 10\lambda$), are by necessity sampling calorimeters. The response of a sampling electromagnetic calorimeter can be expressed as

$$E_{vis} = e E$$

where E , E_{vis} are incident and visible energies respectively and $e = f_{samp}$, the electromagnetic

sampling fraction. Similarly the response of a hadronic sampling calorimeter is

$$E_{vis} = e E_{em} + \pi E_{ch} + n E_n + N E_{nucl}$$

where E_{em} , E_{ch} , E_n , E_{nucl} are respectively the energy deposited by electromagnetic component, charged hadrons, low energy neutrons and energy lost in breaking up nuclei. Each component has its own sampling fraction. N is normally very small but E_{nucl} can be large e.g. it is $\approx 40\%$ in Pb calorimeters. Hence the ratio of the response to electromagnetic and hadronic showers i.e. e/h is usually > 1 and the hadronic calorimeter is said to be *non-compensating*.

In hadronic calorimeters the fluctuation in the visible energy has two sources :

- sampling fluctuations as in the e.m. case which can be reduced by finer sampling and
- intrinsic fluctuation in the shower components (δE_{em} , δE_{ch} etc.) from shower to shower as seen in Fig. 14.

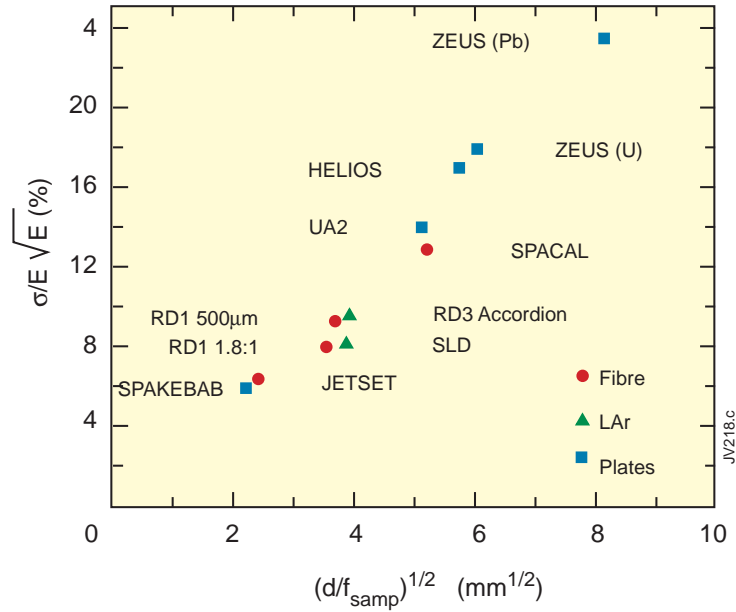


Figure 16: The fractional energy resolution of some calorimeters as a function of $\sqrt{(df_{samp})}$

Therefore the stochastic term is given by

$$a_h = a_{samp} \oplus a_{intr}$$

$$\left(\frac{\sigma}{E}\right)_{samp} = \frac{a_{samp}}{\sqrt{E}} \quad \text{where } a_{samp} \approx 10\% \sqrt{\Delta E_{cell}}$$

$$\left(\frac{\sigma}{E}\right)_{intr} = \frac{a_{intr}}{\sqrt{E}} + c$$

where c is the constant term which depends on e/h and vanishes for a compensating calorimeter.

5.3.1 The Intrinsic Hadronic Energy Resolution

There is a considerable event-to-event fluctuation in the e.m. component (F_0) of hadronic showers. A large event-to-event fluctuation in the neutral fraction is evident. Although at relatively low energy most of the e.m. component is produced in the first interaction, there is a rise in the fraction as the energy of the incident hadron increases, and hadrons further down the cascade

have enough energy to produce neutral pions. This can be seen in Fig. 17 [15] which shows the result of a simulation of pions of 20 GeV and 200 GeV incident on lead.

It usually turns out that the response to electrons and photons i.e. the e.m. component (labeled e) differs from that due to charged hadrons i.e. the non-e.m. component (labeled h). If E is the incident energy the response to electrons (E_e) and charged pions (E_π) can be written as :

$$E_e = e E, \quad E_\pi = [e F_0 + h (1 - F_0)] E \quad \text{leading to}$$

$$\frac{e}{\pi} = \frac{(e/h)}{[(e/h)F_0 + (1-F_0)]}$$

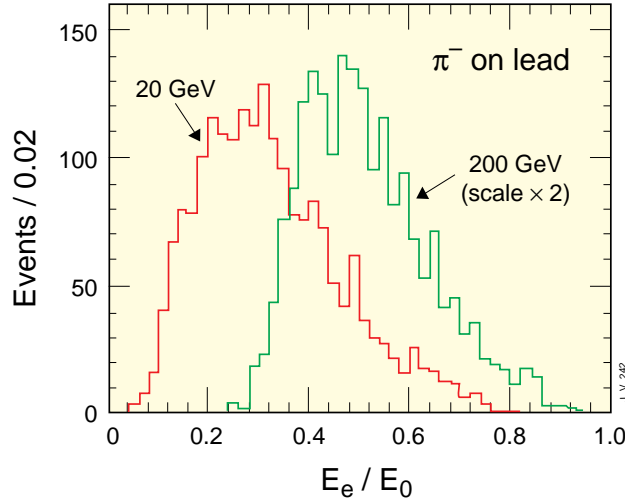


Figure 17: Distribution of e.m. energy fraction for charged pions incident on lead.

If $e/h = 1$ the calorimeter is said to be compensating.

Consider $dE_\pi = [(e - h) dF_0] E$. Then

$$\frac{dE}{E} = \frac{dF_0 [(e/h) - 1]}{[(e/h)F_0 + (1-F_0)]}$$

Hence the fractional error depends on e/h , F_0 and dF_0 . If $e/h=1$ then there is no contribution due to the fluctuation dF_0 . For example:

$$\frac{dF_0}{F_0} = \frac{df_0}{f_0} \sim \frac{1}{\sqrt{f_0 \langle n \rangle}}$$

i.e. for a 200 GeV hadron, $\langle n \rangle \approx 9$, $dF_0 \approx 0.6 \Rightarrow (dE/E)_{\text{comp}} \approx 3.5\%$.

$$\left. \frac{dE}{E} \right|_{\text{comp}} \sim \frac{1}{\sqrt{\ln E}} \quad \text{and} \quad \rightarrow 0 \quad \text{as} \quad E \rightarrow \infty \quad \text{since} \quad \langle n \rangle \propto \ln E$$

This aspect is illustrated by calorimeters using quartz fibres as active media. Charged particles traversing the fibres generate Cerenkov light which is guided to photomultipliers by the fibres themselves. Such a technique is employed by CMS for calorimetry in the very forward region ($3 < |\eta| < 5$) [11: Hadron Calorimeter TDR]. The aim is to measure the energies of, and tag, high energy jets from the WW fusion process. The signal in the calorimeter arises predominantly from the electromagnetic component as charged hadrons have a very high Cerenkov threshold when compared to that of electrons. Hence e/h is very large and the energy resolution at high energies will be dominated by the fluctuation in F_0 . The resolution should improve as $1/\ln E$ rather than as

$1/\sqrt{E}$ as illustrated in Fig. 18 which shows the measured energy resolution of the CMS copper/quartz fibre calorimeter. Also shown is the resolution after subtraction of the contribution from photostatistics. It should be noted that the photostatistics contribution is sizeable as only about 1 photoelectron per GeV is generated.

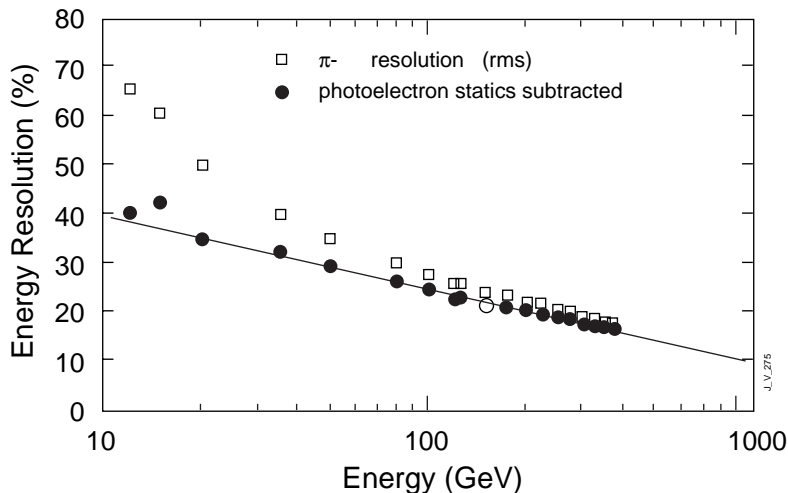


Figure 18: The measured pion energy resolution of a copper/quartz fibres calorimeter.

If $|e/h| \geq 10\%$ the performance of the calorimeter is compromised because of the fluctuation in the π^0 content of the cascades. This leads to:

- a non-Gaussian measured energy distribution for mono-energetic hadrons,
- an e/π ratio that is different from unity and that varies with energy,
- a non-linear response in energy to hadrons,
- an additional contribution to the relative energy resolution (σ/E),
- a σ/e that does not improve as $1/\sqrt{E}$.

These effects have been observed and are detailed in reference [12].

5.3.2 Compensation

The degree of compensation is expressed by the energy independent ratio e/h . The e/h ratio cannot be measured directly but can be inferred from the energy dependent e/π signal ratios. Two relations between the signal ratio $e/\pi(E)$ and e/h given by Groom [15] and Wigmans [16] are:

$$\frac{e}{\pi} = \frac{e/h}{1 + (e/h - 1)F_0}$$

$$F_0 = 1 - (E/0.76)^{-0.13} \quad D. Groom$$

$$or \quad F_0 = 0.11 \ln E \quad R. Wigmans$$

It is instructive to see how the energy is dissipated by a hadron in a Pb absorber. The breakdown of the dissipated energy is as follows:

- 42% in breaking up nuclei and not rendered measurable (invisible)
- 43% by charged particles
- 12% by neutrons with kinetic energy ~ 1 MeV
- 3% by photons with an energy ~ 1 MeV.

The sizeable amount of invisible energy loss means that hadronic calorimeters tend to be under-compensating ($e/h > 1$).

Compensation can be achieved in three ways;

- boost the non-e.m. response using depleted uranium,
- suppress e.m. response
- boost the detectable response to low energy neutrons.

The ZEUS Collaboration [17] have found that achieving compensation for U/scintillator and Pb/scintillator calorimeters requires absorber/scintillator plate thickness ratios given by 1:1 and 4:1 respectively. They also used a technique of interleaved calorimeters to determine the intrinsic energy resolution of U and Pb calorimeters. This is accomplished by reading out odd and even scintillator layers separately. The results are as follows:

hadrons	Pb	$\sigma_{\text{samp}} = 41.2 \pm 0.9\% / \sqrt{E}$	$\sigma_{\text{intr}} = 13.4 \pm 4.7\% / \sqrt{E}$
	U	$\sigma_{\text{samp}} = 31.1 \pm 0.9\% / \sqrt{E}$	$\sigma_{\text{intr}} = 20.4 \pm 2.4\% / \sqrt{E}$
electrons	Pb	$\sigma_{\text{samp}} = 23.5 \pm 0.5\% / \sqrt{E}$	$\sigma_{\text{intr}} = 0.3 \pm 5.1\% / \sqrt{E}$
	U	$\sigma_{\text{samp}} = 16.5 \pm 0.5\% / \sqrt{E}$	$\sigma_{\text{intr}} = 2.2 \pm 4.8\% / \sqrt{E}$

The intrinsic fluctuations in a compensating Pb calorimeter are smaller than those for a U one. However the sampling has to be much coarser for Pb calorimeter leading to a much poorer e.m. energy resolution. ZEUS therefore chose U as the absorber material. It can also be seen that for compensating Pb and U calorimeters the energy resolution is dominated by sampling fluctuations and is given by

$$\sigma_{\text{samp}} = \frac{11.5\% \sqrt{\Delta E_{\text{cell}}(\text{MeV})}}{\sqrt{E(\text{GeV})}}$$

The sampling fluctuations for hadrons are larger than those for e.m. showers by a factor of 2. From the above it is evident that very good e.m. energy resolution is incompatible with $e/h=1$.

5.4 Jet Energy Resolution

Hadronic calorimeters are primarily used to measure the energies of jets and hence the most important quantities that characterize them are:

- jet energy resolution and energy linearity,
- missing transverse energy resolution.

In hadron-collider experiments the energy of jets is often estimated by adding the energy contained in a cone, with half angle ΔR , where $\Delta R = \sqrt{(\Delta\eta^2 + \Delta\phi^2)}$ in pseudorapidity (η) and ϕ space, and whose axis is centred on a seed cell with an energy above a pre-defined threshold. The jet energy resolution is limited by effects from:

- algorithms used to define jets (energy is dependent on cone radius, lateral segmentation of cells etc.),
- the fluctuation in the particle content of jets due to differing fragmentation from one jet to another,
- the fluctuation in the underlying event,
- the fluctuation in energy pileup in high luminosity hadron colliders
- magnetic field.

A figure of merit of a hadron calorimeter is di-jet mass resolution. For the purposes of measuring the jet energy resolution low p_t di-jets ($50 < p_t < 60$ GeV), high p_t di-jets ($500 < p_t < 600$ GeV) and

high mass di-jets ($3 < m_Z < 4$ TeV) at the LHC can be used [18]. The mass resolution for the three categories v/s cone size, ΔR , is shown in Fig. 19a for a perfect calorimeter with no underlying event. The mass resolution improves with increasing cone size. However when running at high luminosity there are ≈ 30 minimum bias events which accompany the event of interest. The fractional mass resolution as a function of cone size is plotted in Fig. 19b. Also plotted is the case when energy is estimated using only the towers above a certain energy threshold (low p_t events – $E_t > 0.3$ GeV, others $E_t > 1$ GeV).

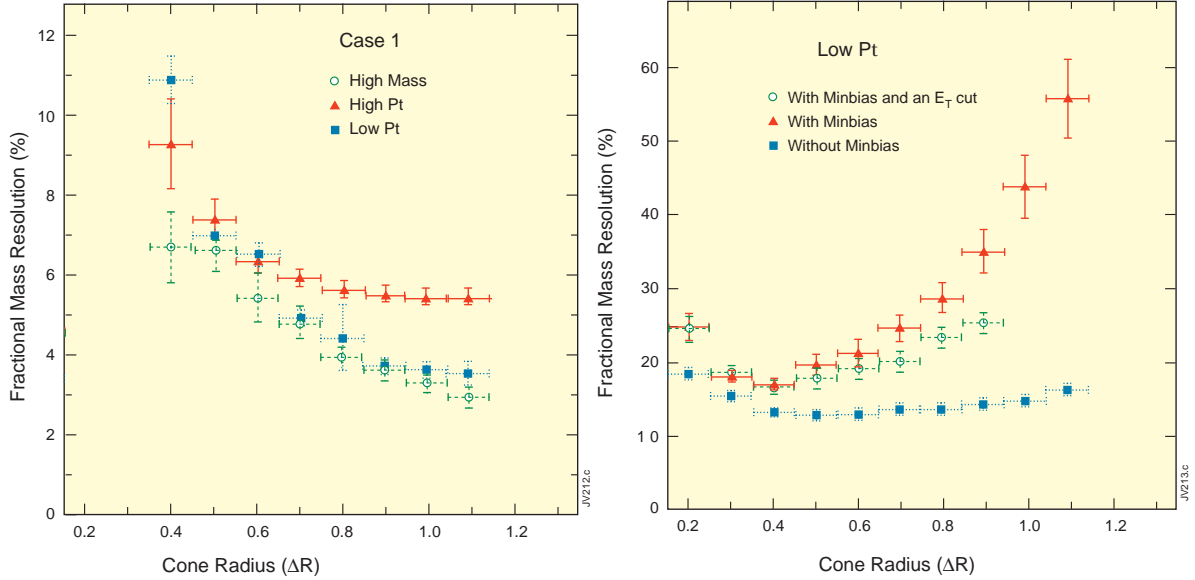


Figure 19: The fractional jet-jet mass resolution as function of cone radius a) perfect calorimeter, b) with 30 minimum bias events overlapped with the event of interest.

From the above it can be seen that in hadronic colliders the uncertainties caused by jet fragmentation (fluctuation of energy inside a pre-defined cone size) and underlying event are very significant in comparison with instrumental effects such as energy resolution, magnetic field, threshold E_T etc.). Hence the mass resolution finally depends on the physics itself. At high luminosities the resolution is degraded if the cone-size is too small (some signal energy is excluded) or if the cone size is too large (significant pileup energy is included). In order to obtain the best mass resolution the cone size has to be optimised for each process and instantaneous luminosity.

The mass resolution due to the angular error, $d\theta$, in defining the jet axis is given by:

$$\frac{dM}{M} = \frac{p_T}{M} d\theta$$

Only highly boosted and low mass di-jets (e.g. boosted Zs from $H \rightarrow ZZ$) will have a significant contribution from the angular error. This is illustrated in Fig. 20 [18].

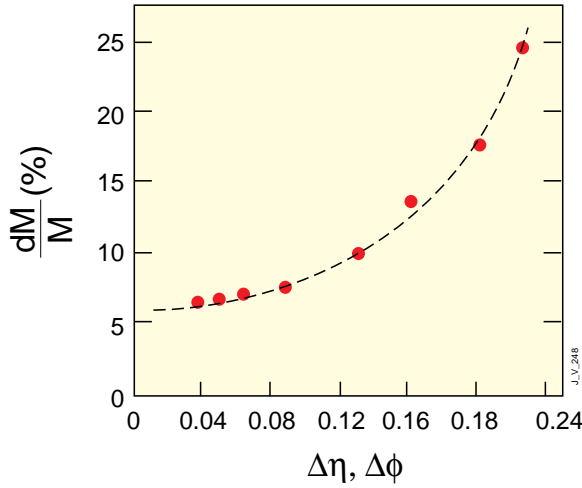


Figure 20: The fractional jet-jet mass resolution as a function of the tower size.

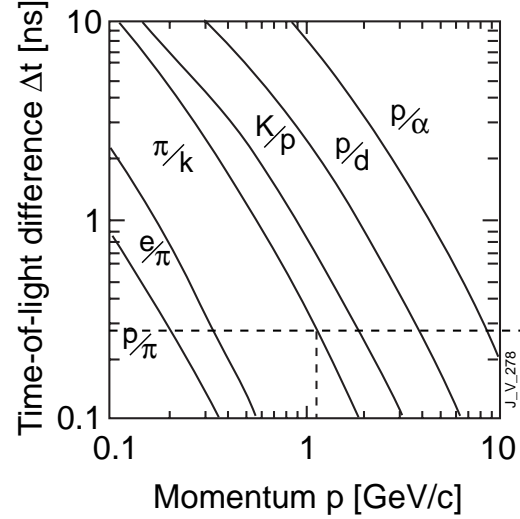


Figure 21: The difference in the time of flight as a function of time for different pairs of particles.

In experiments at e^+e^- machines the jet energy resolution can be improved by using the centre of mass energy to constrain the energies of jets if the jet directions are measured relatively precisely.

6 IDENTIFICATION OF PARTICLES

6.1 Identification of Particles using Time of Flight

At low momenta the difference in the time taken by different particles to traverse a certain distance can be used to distinguish between them. For a particle, with momentum p and mass m_1 , the time taken to traverse a distance L is

$$t_1 = \frac{L}{\beta_1 c}$$

Hence the difference in the time of flight for two particles with masses m_1 and m_2 is

$$\Delta t = \frac{L}{c} \left(\frac{1}{\beta_1} - \frac{1}{\beta_2} \right) = \frac{L}{c} \left(\sqrt{1 + m_1^2 c^2 / p^2} - \sqrt{1 + m_2^2 c^2 / p^2} \right) \approx \frac{Lc}{2p^2} (m_1^2 - m_2^2)$$

The difference Δt is illustrated in Fig. 21 for different pairs of particles as a function of momentum and for a path length of 1m. Plastic scintillators have usually been used to measure the time to a precision of about 300 ps. This enables π/K separation up to ≈ 1 GeV. ALICE [19], the heavy ion experiment on the LHC, will use parallel plate chambers which give a timing precision of ≈ 100 ps enabling π/K separation up to ≈ 2 GeV/c.

6.2 Identification of Particles using Specific Energy Loss

The energy loss of charged particles traversing a medium is given by Equation 1. The ‘truncated’ mean energy loss, measured in the OPAL jet-chamber [20], for different species of particles is shown in Fig. 22. The gas used is 80%/20% Ar/CH₄ at NTP. A large number of samples is used with each sample corresponding to a path-length of ≈ 1 cm. The energy loss measured in each sample has a considerable fluctuation as can be seen from the distribution for minimum ionising pions ($400 \text{ MeV}/c < p < 800 \text{ MeV}/c$) shown in Fig. 23. The distribution is known after Landau

who first calculated it. There is a long tail to the distribution and OPAL reject 30% highest charge samples when determining the mean energy loss per track.

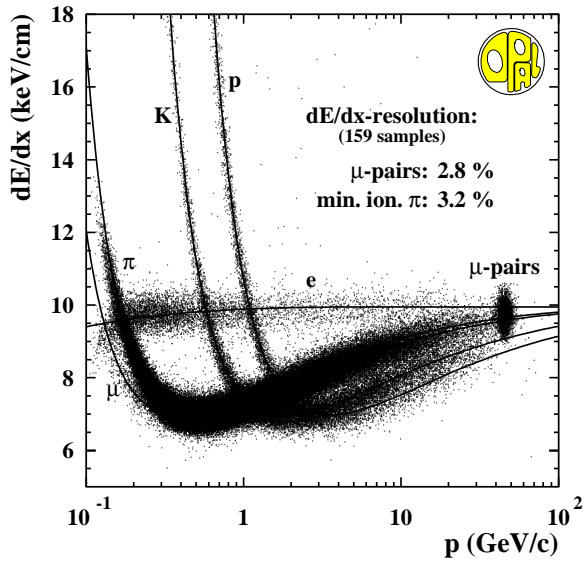


Figure 22: The truncated mean energy loss as a function of momentum for different species of particles.

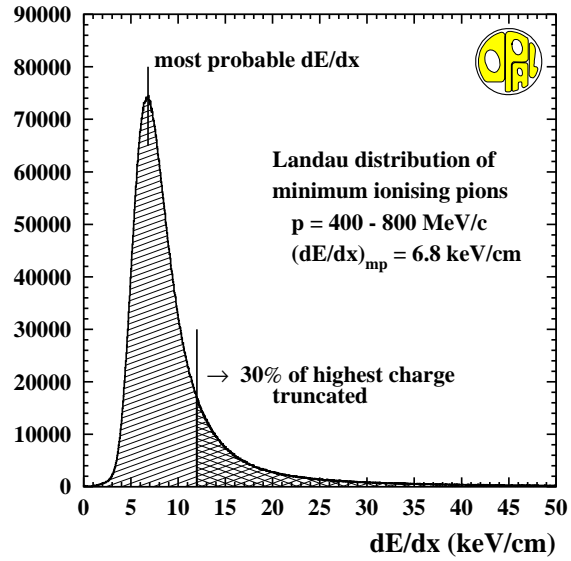


Figure 23: The energy loss distribution for minimum ionising pions.

The difference in the energy loss at a given momentum by various particles can be used to distinguish between them. Since

$$p = m\beta\gamma \quad \text{and} \quad \frac{dE}{dx} \propto \frac{1}{\beta^2} \ln(\beta^2\gamma^2)$$

a simultaneous measurement of p and dE/dx will yield the mass of the particle. The average energy loss for an electron, muon, pion, kaon and proton in 80%/20% Ar/CH₄ gas mixture at NTP is shown in Fig. 22. It can be seen that separation of 10 GeV/c pions and kaons, at 2σ level, requires a $\sigma(dE/dx)$ of $\approx 3\%$. The separation power in OPAL is summarized in Fig. 24.

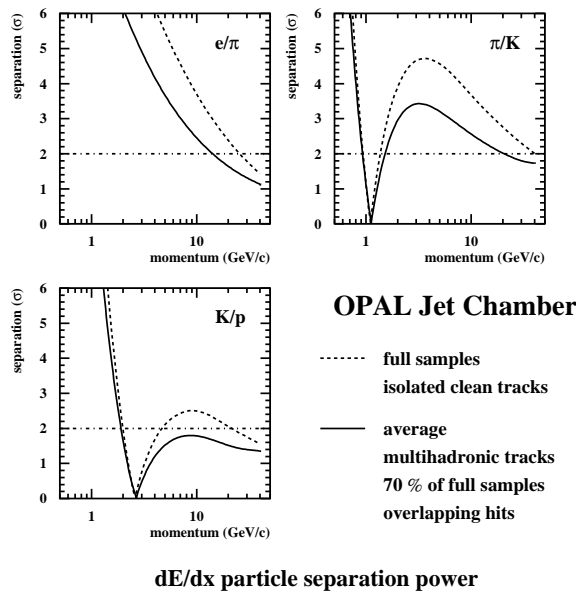


Figure 24: The separation power in OPAL

6.3 Identification of Particles using Cherenkov Radiation

Cherenkov radiation is emitted when a charged particle traverses a dielectric medium, with a refractive index n , at a velocity which is higher than the velocity of light in that medium i.e. if

$$v_{particle} > \frac{c}{n} \quad \text{or} \quad \beta > \beta_{thr} = \frac{1}{n}$$

At each point of emission 'Huygen's wavelets' are generated which add constructively along a cone with half-angle given by the Cherenkov angle (see Fig. 25). The outer surface of the cone constitutes a wavefront. The process is similar to the generation of a sonic shock wave by supersonic aircraft.

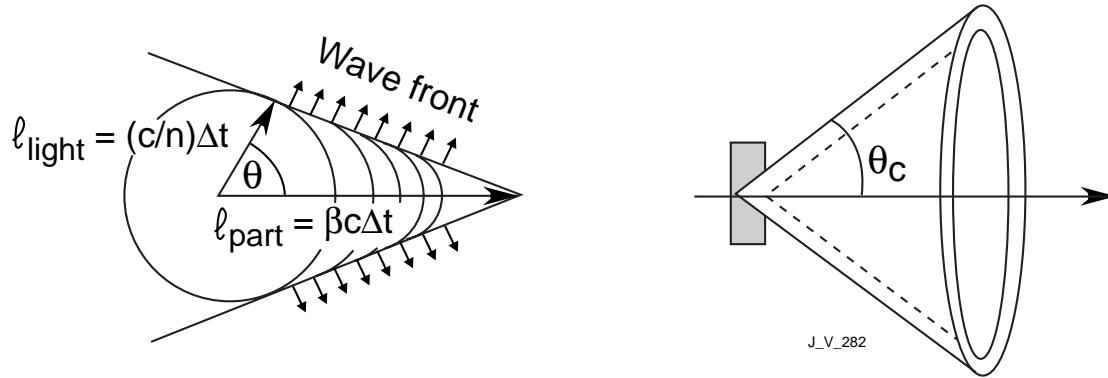


Figure 25: The construction of the Cherenkov light wave-front and the formation of a ring image.

The Cherenkov angle is given by

$$\cos \theta_c = \frac{1}{\beta n} \quad \text{with} \quad n = n(\lambda) \geq 1 \quad \text{and} \quad \theta_{max} = \cos^{-1}\left(\frac{1}{n}\right)$$

The number of photons emitted per unit length of radiator and unit wavelength interval are

$$\frac{d^2 N}{dx d\lambda} = 2\pi z^2 \alpha \frac{1}{\lambda^2} \sin^2 \theta_c$$

$$\text{or} \quad \frac{d^2 N}{dx dE} = \frac{\alpha}{\hbar c} \sin^2 \theta_c \approx 365 \sin^2 \theta_c \quad eV^{-1} cm^{-1}$$

with the characteristic $1/\lambda^2$ dependence. The energy loss through Cherenkov radiation is small ($\approx 1\%$) when compared with that due to ionization. Values of the above parameters for a few radiators are given in Table. 2.

The number of photoelectrons (pe) detected in a photo-device is given by

$$N_{pe} = 370 L \int \epsilon_{col}(E) \epsilon_{det}(E) \sin^2 \theta_c(E) dE$$

where L is the path length in the radiator, ϵ_{col} is the efficiency for collecting the Cv light, ϵ_{det} is the quantum efficiency of photo-conversion of the photodevice. Typically for a photomultiplier, with sensitivity in the range 350-550 nm, $N_\gamma \approx 450 \sin^2 \theta_c \text{ cm}^{-1}$.

Table 2: Parameters for some selected Cherenkov radiators.

Medium	n-1	θ_{\max}	$\pi_{\text{thr}}(p)$ GeV/c	N_{γ} (eV ⁻¹ cm ⁻¹)
Air	1.000283	1.36°	5.9	0.21
Isobutane	1.00217	3.77°	2.12	0.94
Aerogel	1.0065	6,51°	1.23	4.7
Aerogel	1.055	18.6°	0.42	37.1
Water	1.33	41.2°	0.16	160.8
Quartz	1.46	46.7°	0.13	196.4

Two types of Cherenkov detectors are used for particle identification. Threshold Cherenkov detectors use the existence of a threshold for radiation to make a simple yes/no decision based on whether a particle is above/below a threshold velocity ($\beta=1/n$). Ring-Imaging Cherenkov (RICH) detectors can use the dependence of the Cherenkov cone half-angle on the velocity to test a given hypothesis for the mass of the particle with known momentum.

6.3.1 Threshold Cherenkov Detectors

The number of photons emitted depends on the velocity of the particle and is given by

$$N_{\gamma} \propto \sin^2 \theta_C = 1 - \frac{1}{\beta^2 n^2} = 1 - \frac{1}{n^2} \left(1 + \frac{m^2}{p^2} \right)$$

An example of the use of threshold Cherenkov counters comes from BaBar experiment at SLAC [21]. Two aerogel radiators are used: A1 with $n=1.055$ and A2 with $n=1.0065$ leading to the following conditions (Fig. 26) :

- $p > 0.4$ GeV/c, π in A1 give light,
- $p > 1.2$ GeV/c, π in A1 and A2 give light,
- $p > 1.4$ GeV/c, K in A1 give light,
- $p > 4.2$ GeV/c, K in A1 and A2 give light.

Hence π/k separation can be obtained in the range below 4.2 GeV/c which is adequate for the study of CP violation in BaBar.

6.3.2 Ring Imaging Cherenkov (RICH) Detectors

RICH detectors determine the identity of particles by measuring the Cherenkov angle, θ_C , once the momentum has been measured precisely. The principle of operation is illustrated in Fig. 27 [22]. All photons, emitted at the same angle, are focused by a spherical mirror, placed at radius R_M from the point of origin of the particle, to a spherical detecting plane at a radius $0.5 R_M$. The detecting plane will see a ring of photon impacts whose radius can be measured once the centre is known from the tracking system. In realistic detectors this simple concept is modified by magnetic field effects and the requirement of placing the detectors outside the path of the particles.

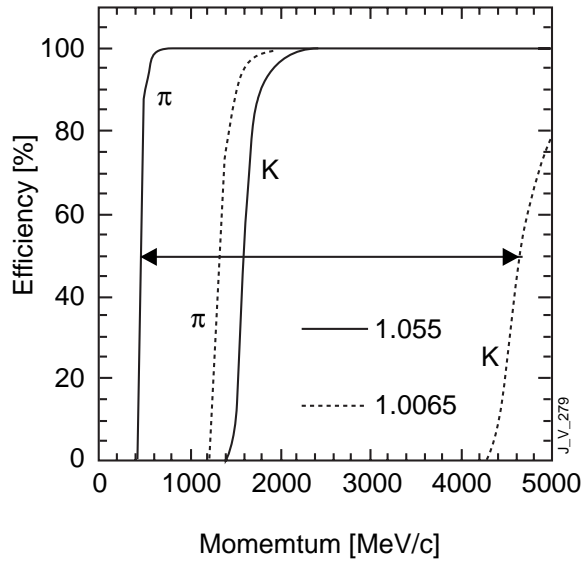


Figure 26: The pion and kaon thresholds for the two aerogel radiators used in BaBar.

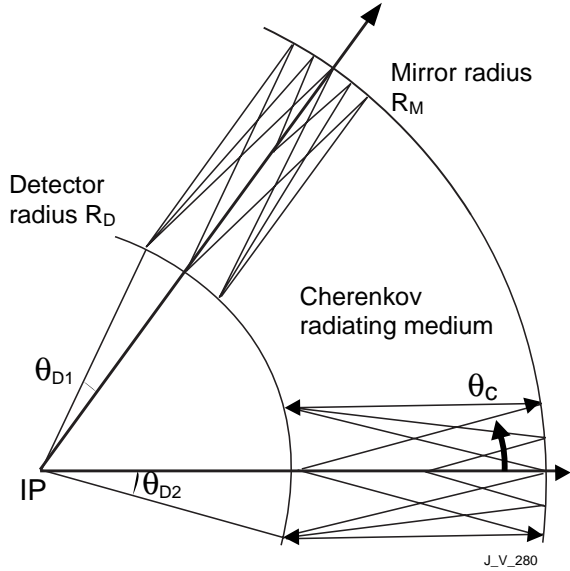


Figure 27: The principle of operation of ring-imaging Cherenkov detectors.

The angle θ_c is given by:

$$\theta_c = \cos^{-1}\left(\frac{1}{\beta n}\right) = \cos^{-1}\left(\frac{E}{pc} \frac{1}{n}\right) = \cos^{-1}\left(\frac{\sqrt{p^2 + m^2}}{pc} \frac{1}{n}\right)$$

The error in the measurement of the angle is minimized by minimizing the error on the localization of a photo-conversion, σ_θ , and maximizing the number of photo-electrons, N_{pe} . Two particles with masses m_1 and m_2 can be distinguished by n_σ up to a momentum p given by

$$p = \frac{1}{\sqrt{n_\sigma}} \sqrt{\frac{(m_2^2 - m_1^2) \sqrt{N_{pe}}}{2 \tan \theta \times \sigma_\theta^{pe}}}$$

As an example π/K can be separated up to 75 GeV/c at a 3σ level for $N=20$ pe, $\sigma_\theta=1$ mrad and $\theta=31$ mrad (CF_4).

The LHCb experiment [23] will use two RICH detectors to provide π/K separation in the momentum range from 1 to ≈ 100 GeV/c. The first RICH detector (Fig. 28) is a combined gas (C_4F_{10})-aerogel device and the second one is a gas device. The Cherenkov light will be detected by recently developed hybrid photo-detectors (HPD), sensitive to visible and near-UV light using small silicon-pad pixels to give unambiguous 2-D space points. The response for many triggers is shown in Fig. 29: there are ≈ 4 photoelectrons/event on the air ring (HPD1) and ≈ 1 photoelectron/event on the aerogel ring (HPD2-7).

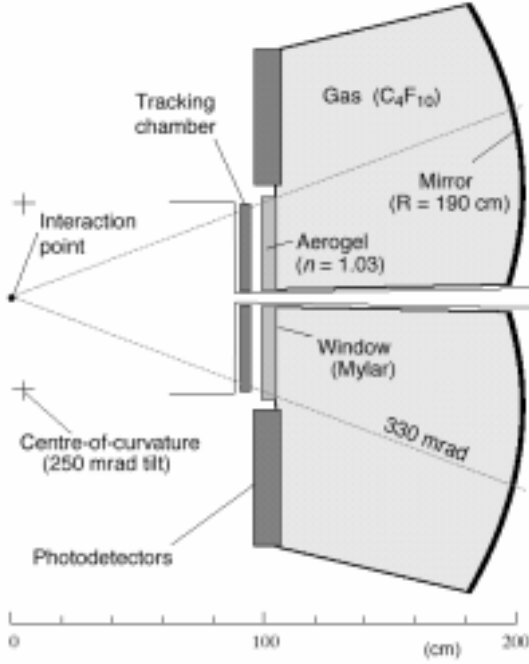


Figure 28: A combined gas(C_4F_{10})/aerogel RICH HPDs.device for LHCb.

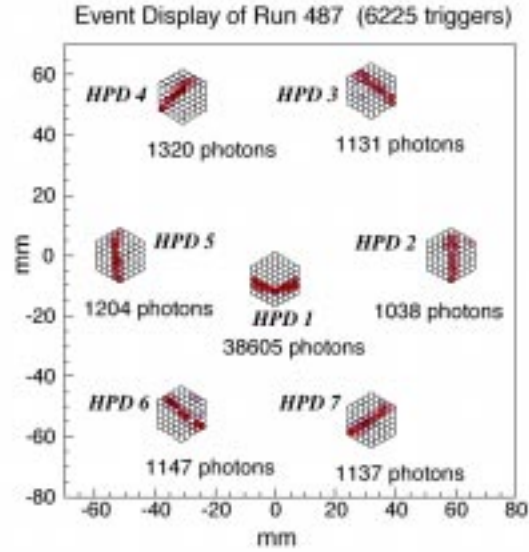


Figure 29: The Cherenkov light is detected by The response for many triggers is shown.

6.4 Identification of Electrons using Transition Radiation Detectors

The existence of transition radiation was predicted by Ginzburg and Franck in 1946. Transition radiation is emitted when a charged particle moves from a medium of refractive index n_1 to a medium of a different index n_2 . This may be thought of as an apparent acceleration. The changes in the medium are achieved by using thin foils of material like polyethelene and air.

Consider

$$p = \gamma m v \Rightarrow m = \frac{1}{\beta c \gamma} p$$

$$\therefore \left(\frac{\Delta m}{m} \right)^2 = \frac{1}{\beta^2 c^2} \left(\frac{\Delta \gamma}{\gamma} \right)^2 + \left(\frac{\Delta p}{p} \right)^2$$

If the momentum is precisely measured (i.e. $\Delta p/p$ is small) then the mass resolution at high momenta is $\propto \gamma$. The radiated energy/boundary to vacuum is given by:

$$W = \frac{1}{3} \alpha \hbar \omega_p \text{ i.e. } W \propto \gamma$$

where $\hbar \omega_p$ (≈ 20 eV for polyethelene) is the plasma frequency

The X-rays of transition radiation are emitted at a small angle w.r.t. the charged track ($\theta=1/\gamma$). The energy of the photons and the number of photons per boundary are given by

$$E_{ph} = \frac{\gamma}{3} \hbar \omega_p \text{ and } N_{ph} \approx \frac{W}{\hbar \omega_p} \propto \alpha \approx \frac{1}{137}!$$

Hence many transitions are needed. The detector therefore consists of a stack of many thin foils with a high Z detecting gas for effective photo-conversion of X-rays. The particle must traverse a minimum thickness to efficiently emit transition radiation, This is $\approx 20 \mu\text{m}$ for polyethelene.

6.4.1 ATLAS Transition Radiation Tracker

The ATLAS TRT [10. Inner Tracking TDR] comprises straw tube proportional chambers embedded in polyethylene fibres (see Fig. 30). Standard radiators for TR are made out of 15-20 μm thick polypropylene foils with a regular 200-300 μm spacing. Such regular radiators provide the highest radiation yield because the thickness and spacing can be optimised for each detector concerned. The ATLAS geometry however does not allow use of foil radiators. Foam radiators made out of polyethylene have been found to be the best but not as good as foil radiators as the variation of wall thickness and spacing are large. Furthermore it was found that properly oriented polyethylene fibres are almost as performant.

The gas in the straw tubes has to be an efficient X-ray absorber and hence dense gases such as Xe are employed. In order to attain high rate capability the gas has to be fast and ATLAS use CF_4 . In order to ensure stable operation at high gains a quenching gas such as CO_2 is needed. The gas chosen by ATLAS has the following composition: 70%:20%:10%/ Xe: CF_4 : CO_2 .

The probability to observe in a single straw an energy deposit from 200 GeV electrons above a given threshold is shown in Fig. 31 as a function of the this threshold for a variety of radiators (and no radiator). The best radiators are those yielding the highest probability/straw for an energy threshold of $\approx 6-7$ keV. The probability to exceed such a threshold is a factor 3-4 higher with than without a radiator. The difference between the probability for electrons and pions to deposit large amounts of energy in straws is shown in Fig. 32. In ATLAS the average number of TR hits (signaled by large energy deposits) for 30 GeV electrons is ≈ 6 per track compared with ≈ 1 for pions of the same energy.

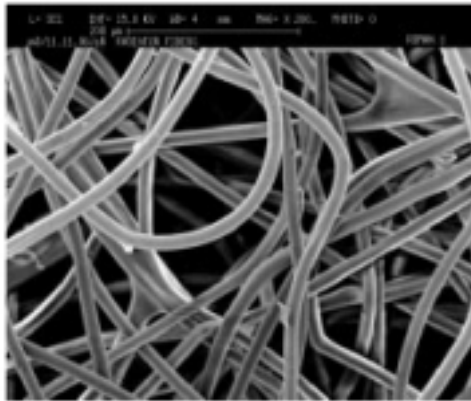


Figure 30: The detail of the polyethelene fibre radiator.

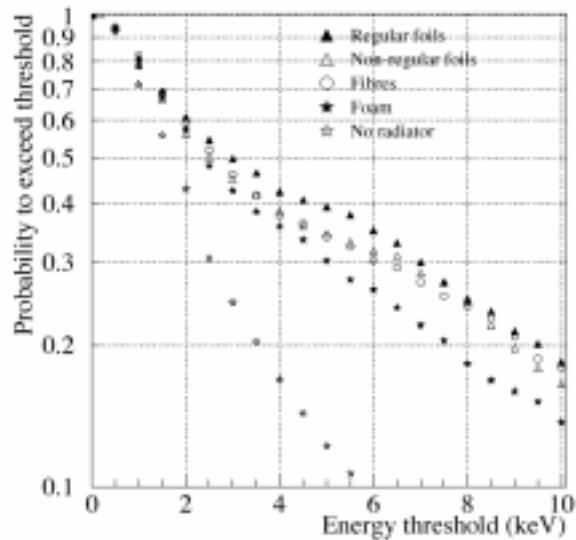


Figure 31: The probability of 200 GeV electrons to exceed a given threshold with and without radiators.

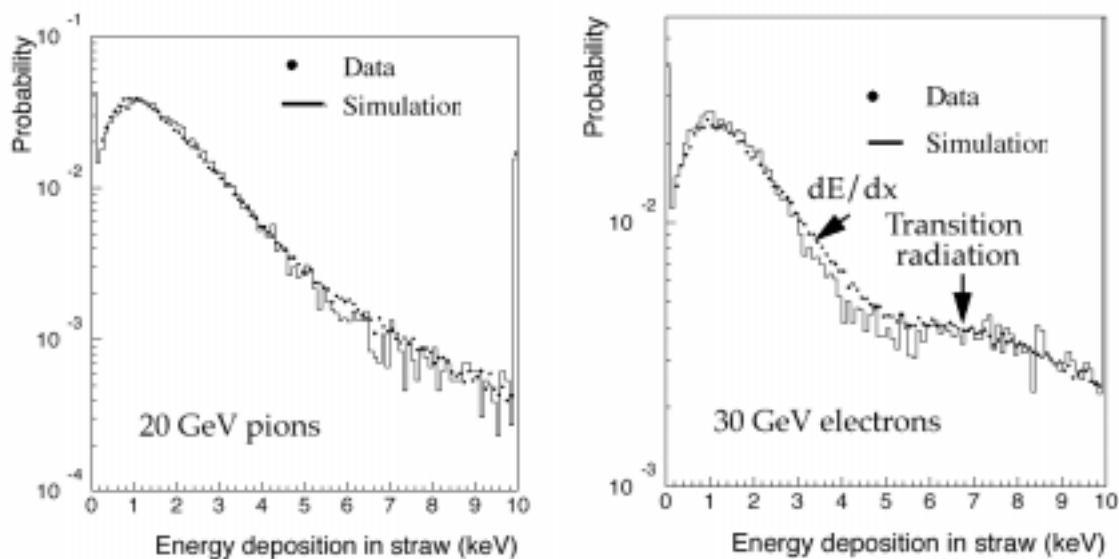


Figure 32: The difference between the distribution of energy deposits in the ATLAS TRT for 20 GeV pions and 30 GeV electrons showing clearly the onset of transition radiation for electrons.

6.5 Identification of b-jets

There are two methods for tagging b-jets. Charged leptons with relatively high momentum and a large momentum transverse to the jet axis arise mainly from semi-leptonic decays of b-hadrons. Hadronic decays of b-quarks can be enriched by taking advantage of the relatively long (≈ 1.5 ps) lifetimes of bottom hadrons. The long lifetime leads to secondary vertices which are separated from the primary vertex. Hence one looks for:

- relatively high transverse momentum electrons or muons within a jet arising from the semi-leptonic decay of a b-quark.
- one or more charged tracks within a jet with a significant impact parameter (defined to be the distance of closest approach of the track from the primary vertex)
- a secondary vertex consistent with the flight path of a B-meson (see Fig. 33).

The latter two methods require measuring layers close to the interaction vertex. Both CMS and ATLAS have several layers of pixel detectors. The precision with which the impact parameter can be measured is determined by:

- the closeness of the first measuring layer from the interaction vertex,
- the number of measurements close to the interaction vertex,
- the spatial resolution of the measured points and
- the amount of material in these layers leading the degradation in the significance of impact parameter due to multiple scattering.

Some of these points are illustrated in Fig. 34 that presents the results of a simulation of the CMS inner tracker. The points plotted are for two different radii of the first pixel layer (4 cm or 7.7 cm), differing number of tracks with different significance of the impact parameter. The estimated impact parameter resolution for 10 GeV tracks in CMS is around 15 (>20) μm for the first pixel layer at 4 (7.7) cm.

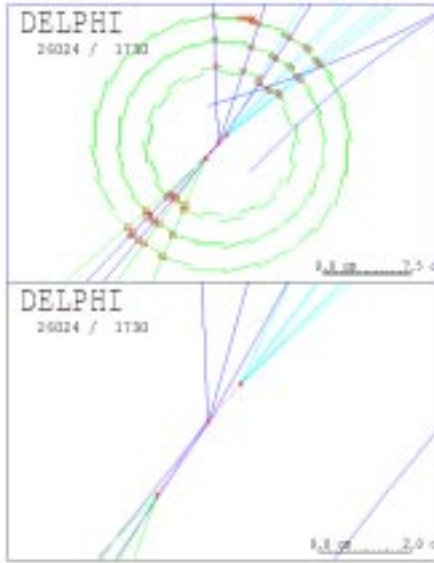


Figure 33: A DELPHI (LEP) event with two reconstructed B-hadron vertices.

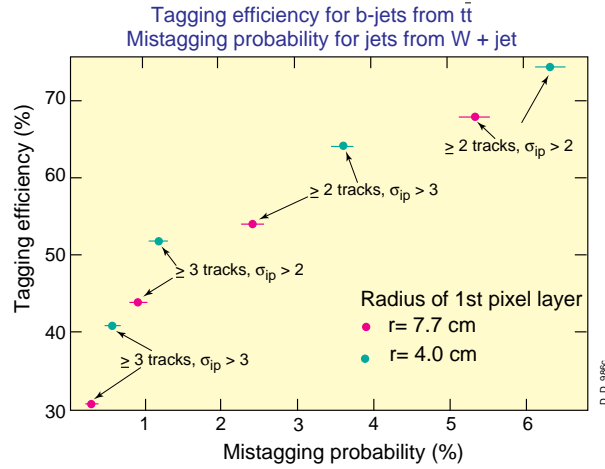


Figure 34: Tagging efficiency for b-jets and mistagging probability in CMS for various conditions.

6.6 Particle Identification Using Calorimeters

Below we consider some ways in which calorimeters can be used to identify isolated electrons and photons from hadrons and jets.

6.6.1 Isolated electromagnetic shower-jet separation

The largest source of electromagnetic showers is from the fragments of jets, especially π^0 s. A leading π^0 taking most of the jet energy can fake an isolated photon. There are large uncertainties in jet production and fragmentation. Furthermore the ratio of production of di-jets to irreducible di-photon background is $\approx 2 \cdot 10^6$ and γ -jet/irreducible $\gamma\gamma$ is ≈ 800 . Hence a rejection of ≈ 5000 against jets is needed. A certain rejection factor (≈ 20) can be obtained by simply asking for e.m. showers with a transverse energy greater than some threshold with the energy measured in a small region.

Jets can be distinguished from single electromagnetic showers by

- demanding an energy smaller than some threshold in the hadronic compartment behind the electromagnetic one
- using isolation cuts
- demanding a lateral profile of energy deposition in the ECAL consistent with that from an electromagnetic shower.

Using these criteria ATLAS [10: LAr TDR] estimates that the rejection factor against jets can be ≈ 1500 for a photon efficiency of 90%. This is illustrated in Fig. 35 where the effect of various cuts is shown: a) the energy (E_T^{had}) in the hadron calorimeter compartment behind the e.m. one of size $\Delta\eta \times \Delta\phi = 0.2 \times 0.2$ should be less than 0.5 GeV, b) e.m. isolation (R_{isol})— more than 90% of the energy is contained in the central 3×5 e.m. cells compared with that in central 7×7 e.m. cells, c) lateral shower profile (R_{lateral})— look for an e.m. core such that the central 4 towers contain more than 65% of the shower energy, d) shower width in η (σ_η). The distribution for jets is shown as dashed histogram whereas the full histograms depict single photons.

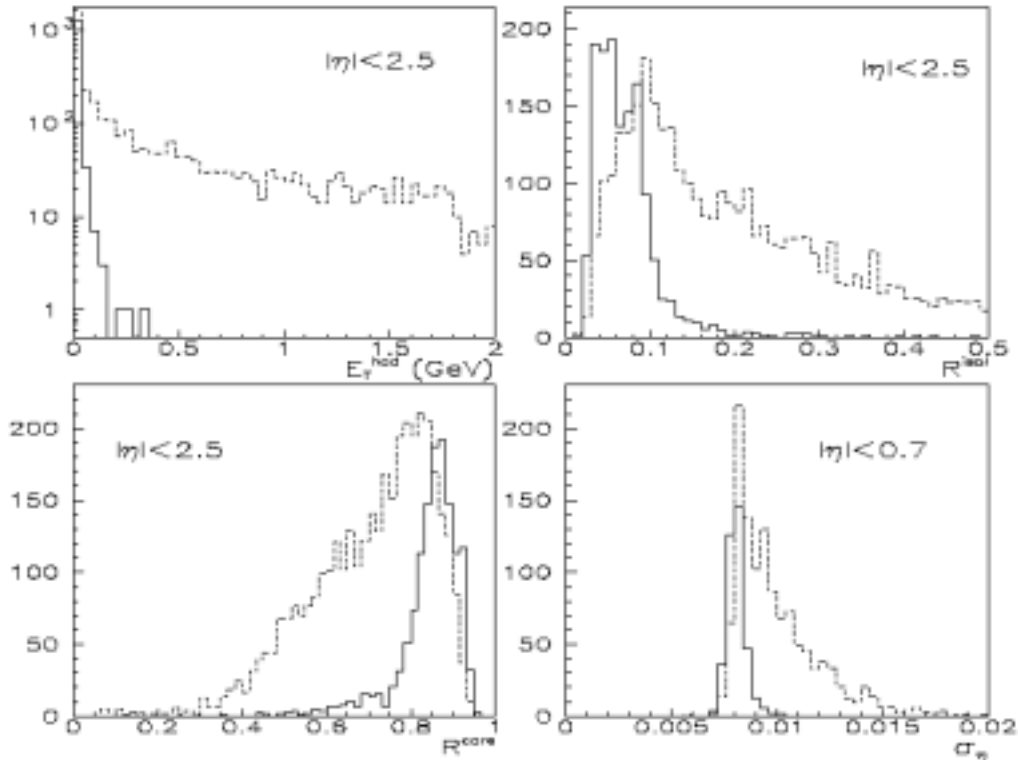


Figure 35: The distributions used to cut against jets. Solid histogram is for photons and the dashed one for jets. See text for explanation.

6.6.2 Photon – π^0 separation

After the application of the above criteria only jets resulting in leading π^0 s can fake genuine single photons. Further rejection can only be achieved by the recognition of two e.m. showers close to each other. CMS [11: ECAL TDR] uses the fine lateral granularity ($\approx 2.2\text{cm} \times 2.2\text{cm}$) of their crystals and a neural network algorithm that compares the energy deposited in each of the 9 crystals in a 3×3 crystal array with that expected from a single photon. Variables are constructed from the 9 energies, x and y position of impact and a pair measuring the shower width. The fraction of π^0 s rejected is shown in Figure 36.

The narrowness of the e.m. shower in the early part can be used to reject events consisting of two close-by e.m. showers. Planes of fine pitch orthogonal strips after a pre-shower, placed at a depth of $\approx 2.5 X_0$, can also be used to distinguish π^0 s from single photons. Results using 2mm pitch strips are shown in Fig. 36.

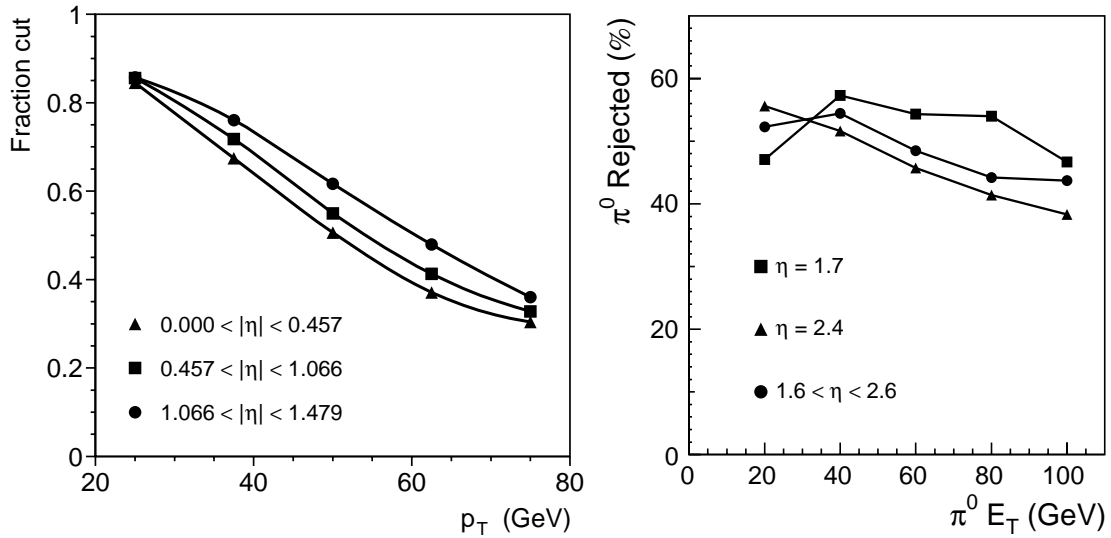


Figure 36: lhs) Fraction of pizeros rejected using lateral shape of energy deposit as a function of p_T rhs) Variation of pizero rejection as a function of η using two planes of orthogonally oriented 2mm pitch Si strips after 2 and 3 X_0 .

6.6.3 Electron-hadron Separation

A high energy pion faking an electron leads to the contamination of signals using prompt electrons. At LHC in order to bring down the rate of fake electrons from this source to a factor ≈ 10 below that from the genuine sources (e.g. $b \rightarrow e X$, $W \rightarrow e \nu$ etc.) an $e-\pi$ separation of ≥ 1000 is required for $p_T \geq 10$ GeV/c.

The electron-hadron separation is usually based on the difference in the longitudinal and lateral development of showers initiated by electrons and charged hadrons. One or more of the following can be used to achieve the desired pion rejection power when detecting electrons :

- a preshower detector between $\approx 1.5 - 4 X_0$
- lateral segmentation
- longitudinal segmentation including a hadron calorimeter
- energy - momentum matching

The ultimate rejection power is limited by the charge exchange process or the first hadronic interaction, which results in one or several π^0 's taking most of the energy of the incoming hadron. The shower from such hadrons then looks like an e.m. shower. Therefore sampling of showers early in their longitudinal development is important.

The separation power for single particle, using (i - iii) is shown in Fig. 37 [24]. The structure of the calorimeter consisted of :

- towers of a lateral size of $\sim 11 \times 11$ cm (effective $X_0 \approx 8$ mm),
- 8-fold longitudinal segmentation, the first four samplings (2mm U / 2.5 mm TMP) with thickness of 3, 6, 10, 7 X_0 leading to a total of 1λ , the next two (5mm U/ 2.5mm TMP) each with thickness of 0.7λ and the last two (5cm Fe/ 1cm scintillator) each with thickness of 2.5λ .
- a position detector placed at a depth of 3 X_0 . The rejection power, as a function of energy, using (ii), (iii) and (iv) individually and then all combined is shown.

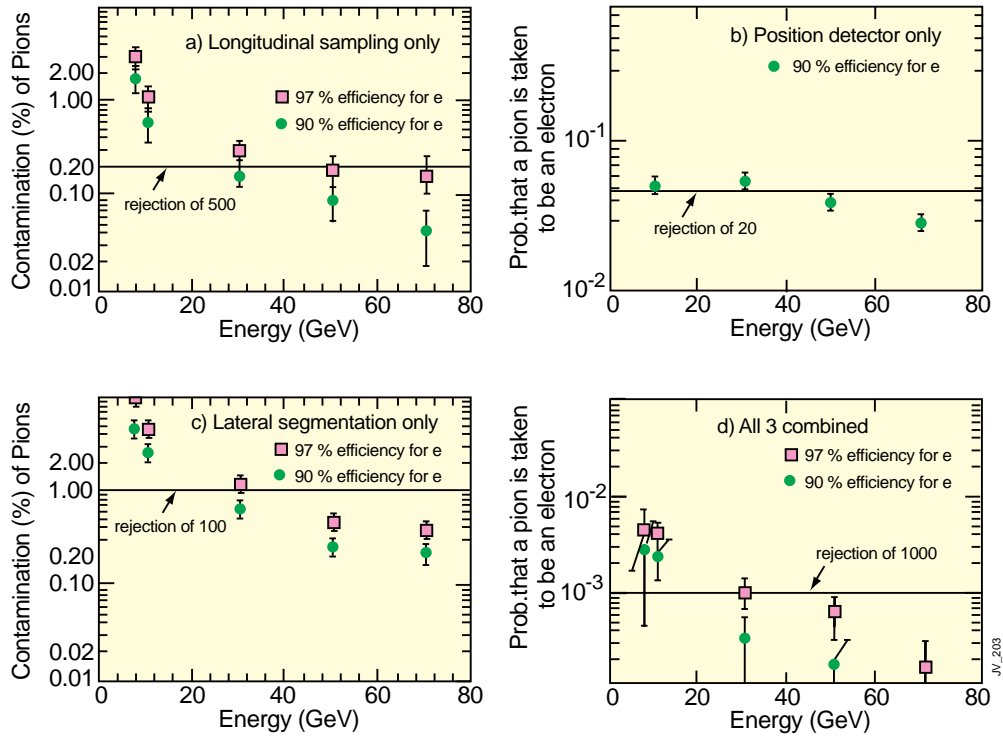


Figure 37: The probability that a single pion is taken to be an electron using a) longitudinal profile only, b) preshower detector only, c) lateral profile only and d) all three combined.

6.7 Identification of Muons

Muons are identified by their penetration power through the material of calorimeters which absorb the electrons, photons and hadrons. The depth required to absorb the hadrons is shown in Fig. 38 for pions of various energies. It can be seen that about two metres equivalent of iron is needed to absorb most of the energy of the hadrons. This corresponds to over 10λ of material. Insufficient depth of material can allow debris from hadronic showers to emerge and hence cause false identification of a hadron as a muon. The added confusion can also lead to difficulty in matching muon-tracks in jets and increase in trigger rate. Two scenarios are illustrated in Fig. 39. The study was carried out in H2 beamline at CERN using a 3T magnet followed by slabs of magnetized iron. A calorimeter is installed inside the magnet. One shows a hadron starting a shower late and contaminating the first muon station and the second with a secondary muon penetrating the muon system.

The identification and the measurement of the momentum of muons is accomplished by tracking in magnetic field. Two configurations are possible, tracking in air-filled magnetic field or in magnetized iron.

Extra material is usually required when muons are tracked through an air-filled field in order to decrease hadronic punchthrough from the calorimeters. However the magnetic field can help by sweeping the soft debris that may 'punch-through'.

Muons of energies above a few hundred GeV generate their own background when traversing magnetized iron. The critical energy of muons in iron is 350 GeV and hard bremsstrahlung (sometimes labeled catastrophic energy loss) can spoil muon tracking. A simulation of a 1 TeV muon traversing iron is shown in Fig 40. When tracking in iron several muon stations are required separated by a sufficient thickness of iron so as to kill the e.m. shower before the following station is reached.

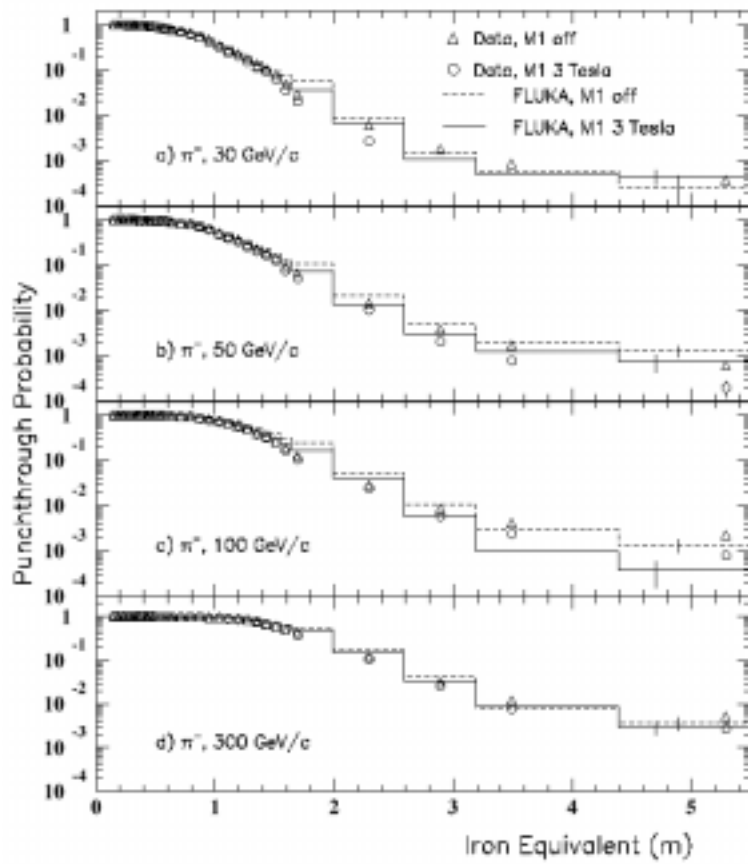


Figure 38: The punchthrough probability as a function of thickness of iron.

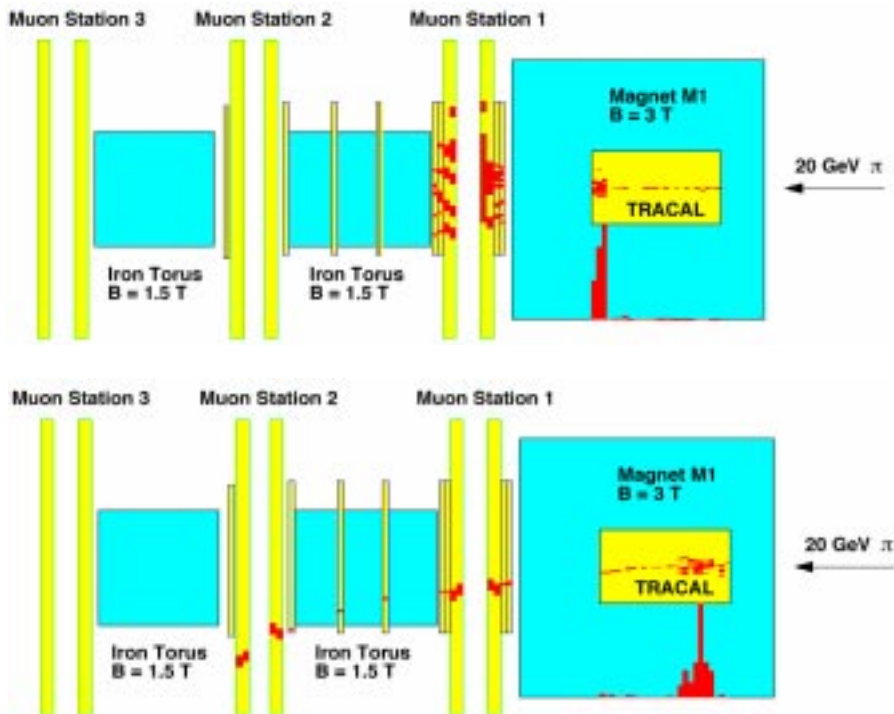


Figure 39: Two examples of punchthrough-one leading to confusion in the muon station and the other leading to a secondary muon.

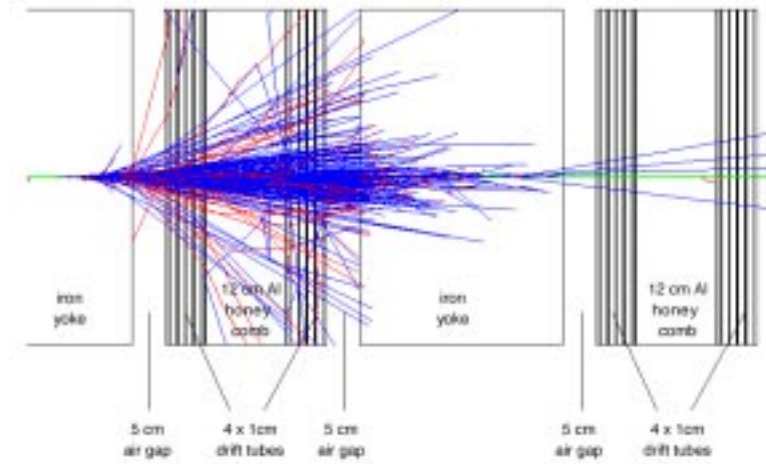


Figure 40: The simulation of a 22 GeV electromagnetic shower generated by a photon radiated by a 1 TeV muon.

7 THE EXPERIMENTAL CHALLENGE AT THE LHC

In the search for high-mass objects and rare signatures, high \sqrt{s} and high luminosity are required. The main LHC machine parameters (proton-proton mode) are a centre of mass energy of $\sqrt{s}=14$ TeV, design luminosity of $L=10^{34}$ $\text{cm}^{-2} \text{s}^{-1}$ and a bunch crossing interval of 25 ns. The large proton-proton inelastic cross-section (≈ 70 mb) leads to some 10^9 interactions/sec. These parameters lead to formidable experimental challenge [6].

The event selection (trigger) must reduce the billion interactions/s to ≈ 100 events/s for storage. The short bunch-crossing period has implications for the design of the readout and trigger systems. It is clearly not feasible to make a trigger decision in the time between bunch crossings, yet new events occur every crossing and a trigger decision has to be made for every crossing. This requires relatively complicated *pipelined* trigger processing and readout, where many bunch crossings are processed concurrently by a chain of processing elements. The 1st Level trigger decision takes ≈ 3 μs so the data must be stored in pipelines for ≈ 3 μs .

At design luminosity a mean of ≈ 20 minimum bias events will be superposed on the event of interest. Around 1000 charged tracks emerge from the interaction region every 25 ns. Thus, the products of an interaction under study may be confused with those from other interactions in the same bunch crossing. This problem, known as *pileup*, clearly becomes more severe if detectors with a response time longer than 25 ns are used. The affect of pileup can be reduced by using highly granular detectors with good time resolution, giving low *occupancy* (fraction of detector elements that contain information) at the expense of having large numbers of detector channels.

The high particle fluxes emanating from the interaction region lead to high radiation levels requiring radiation hard detectors and front-end electronics.

LHC detectors are therefore not just larger versions of the previous generation of HEP detectors. Many years of R&D have been needed to develop detectors and electronics that could survive the harsh environment of LHC.

8 THE PROTON-PROTON EXPERIMENTS AT THE LHC

The p-p General Purpose Detectors (GPDs) at the LHC follow closely the onion-like structure discussed in the introduction. The single most important aspect of the overall detector design is the magnetic field configuration for the measurement of muon momenta. The choice strongly

influences the rest of the detector design. The two basic configurations are solenoidal and toroidal. The closed configuration of a toroid does not provide magnetic field for inner tracking. Since a detector without magnetic inner tracking cannot adequately study a number of important physics topics an additional inner solenoid is required to supplement a toroid. Large bending power is needed to measure precisely high momentum muons or other charged tracks. This forces a choice of superconducting technology for solenoids whereas both superconducting (air or iron core) and warm (iron core) are possible for toroids. Below we briefly discuss the advantages and drawbacks of each of the configurations.

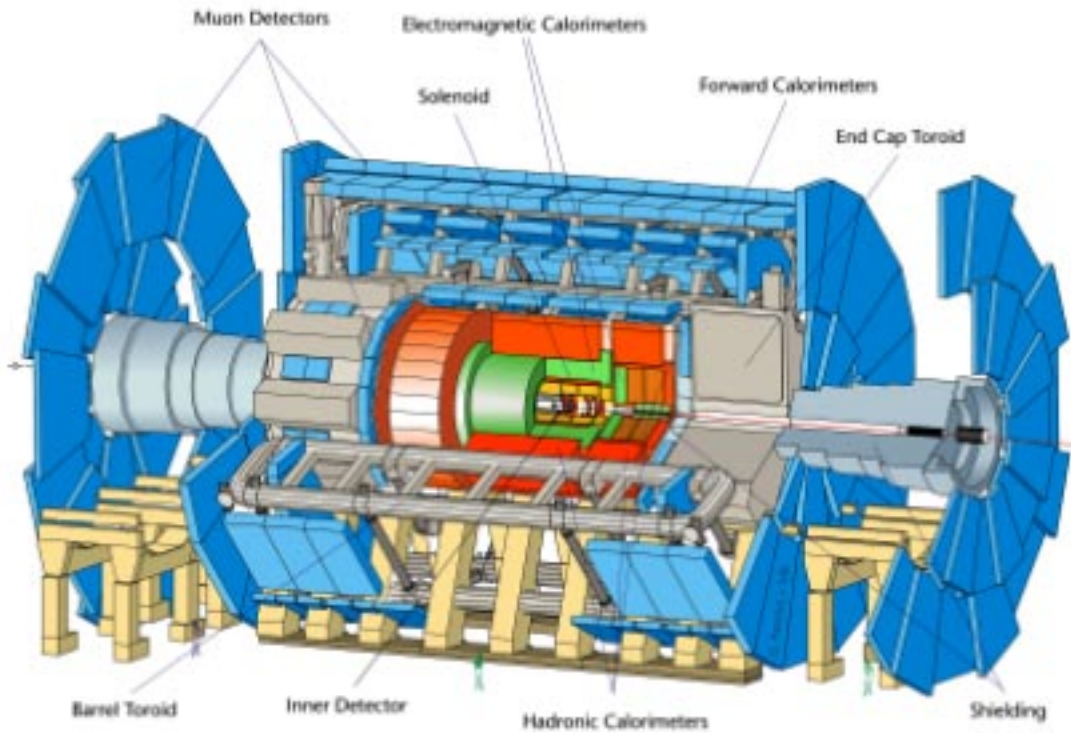


Figure 41: The 3-D view of the ATLAS detector displaying the various sub-detectors.

8.1 ATLAS

The overall detector layout is shown in Fig 41. The magnet configuration uses large superconducting air-core toroids consisting of independent coils arranged with an eight-fold symmetry outside the calorimetry. The magnetic field for the inner tracking is provided by an inner thin superconducting solenoid generating a field of 2T.

The inner detector is contained a cylinder of length 6.8 m and radius 1.15 m. It consists of a combination of ‘discreet’ high-resolution Si pixel and microstrip detectors in the inner part and ‘continuous’ straw-tube tracking detectors with transition radiation capability in the outer part of the tracking volume. Highly granular liquid-argon (LAr) e.m. sampling calorimetry covers the pseudorapidity range $|\eta| < 3.2$. In the endcaps the LAr technology is used for the hadronic calorimeter. The forward LAr calorimeters, extending the coverage to $|\eta| = 4.9$ are also housed in the same cryostat. The barrel part of the hadronic calorimetry is provided by Fe/ scintillator-tile sampling calorimeter using WLS fibres. The calorimetry is surrounded by the muon spectrometer. The air-core toroid system encloses a large field volume. The muon chambers, grouped into three stations, are placed in the open and light structure to minimize effects from

multiple scattering. The muon spectrometer defines the overall dimensions of the ATLAS detector with a diameter of 22m and a length of 46 m. The weight of the detector is about 7000 tons.

8.2 The Compact Muon Solenoid (CMS)

The overall layout is shown in Fig. 42. At the heart of CMS sits a superconducting solenoid. In order to achieve a good momentum resolution within a compact spectrometer without making stringent demands on muon-chamber resolution and alignment a high magnetic field is required. CMS has a long (13 m), large bore ($\phi=5.9$ m) and high field (4T) solenoid. The field is large enough to saturate 1.5 m of iron which is thick enough to accommodate four muons stations to ensure robustness and full geometric coverage. Each muon station consists of many measuring planes. These consist of aluminium drift tubes in the barrel region and Cathode Strip Chambers (CSCs) in the endcap region.

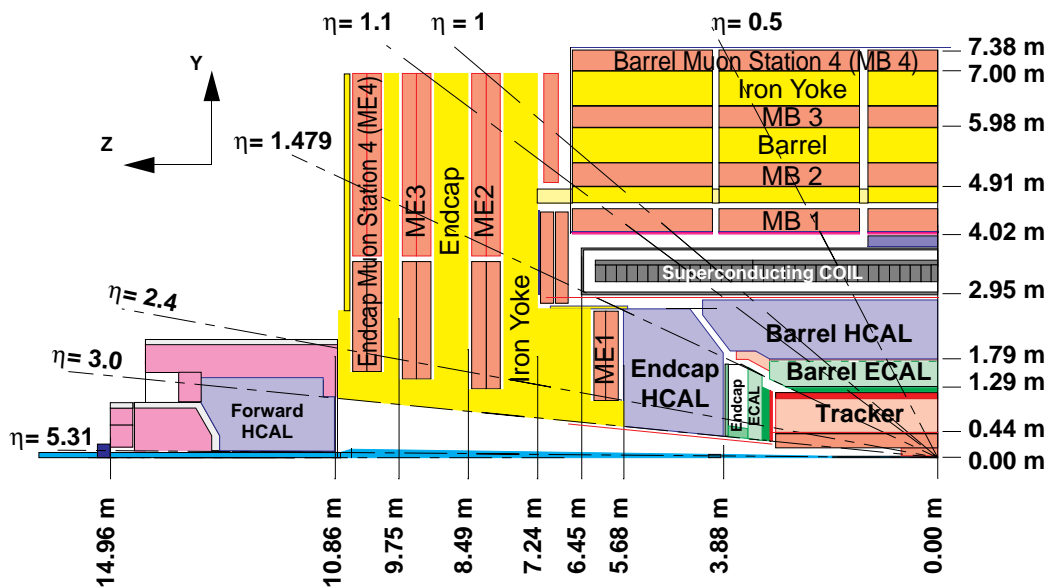


Figure 42: The transverse cut of the CMS detector.

The bore of the magnet is large enough to accommodate the inner tracker and the calorimetry inside the coil. The tracking volume is given by a cylinder of length 6 m and a diameter of 2.6 m. In order to deal with high track multiplicities tracking detectors with small cell sizes are used. Solid-state and gas microstrip detectors provide the required granularity and precision. Pixel detectors placed close to the interaction region improve the measurement of the track impact parameter and secondary vertices. The electromagnetic calorimeter (ECAL) uses lead tungstate (PbWO_4) crystals. A preshower system is installed in front of the endcap ECAL for π^0 rejection. The ECAL is surrounded by a copper/scintillator sampling hadronic calorimeter. The light is channeled by clear fibres fused to wave-length shifting fibres embedded in scintillator plates. The light is detected by photodetectors that can provide gain and operate in high axial magnetic fields (proximity focussed hybrid photodiodes). Coverage up to rapidities of 4.7 is provided by a Cu/quartz fibre calorimeter. The Cerenkov light emitted in the quartz fibres is detected by photomultipliers. The forward calorimeters ensure full geometric coverage for transverse energy measurement. The overall dimensions of the CMS detector are: a length of 21.6 m, a diameter of 14.6 m and a total weight of 14500 tons.

8.3 Muon Systems

8.3.1 ATLAS

The number of field lines crossed by a muon track in toroids is constant. In the endcap region the magnetic field increases as $1/R$. Hence toroids have the property that the transverse momentum resolution is constant over a wide range of pseudo-rapidity. The integral of $B \cdot dl$ ($\propto 1/\sin\theta$) compensates for the Lorentz boost in the forward direction. In an air-core toroid a good stand alone momentum resolution can be reached as long as the quantity BL^2 is large enough (cf. Equation 2). Two drawbacks of the toroidal configuration are:

- the bending does not take place in the transverse plane and hence benefit cannot be drawn from the precise knowledge of the beam-beam crossing point ($20 \mu\text{m}$ at LHC), and
- a solenoid is needed to provide field for the inner tracker, opening the debate of whether the coil should be place before or after the electromagnetic calorimetry.

The design criteria for the muon system can be obtained by requiring that an unambiguous determination is made of the sign for muons of 1 TeV. This implies that $\Delta p/p \approx 10\%$. The sagitta, s , for a track of momentum p in a uniform magnetic field is given by $s=0.3BL^2/8p$. In the case of ATLAS where $B \approx 0.6\text{T}$, $L \approx 4.5 \text{ m}$ $s \approx 0.5 \text{ mm}$ for $p_\mu = 1 \text{ TeV}$. This implies that the sagitta has to be measured with a precision of $\approx 50 \mu\text{m}$. For muon system as large as in ATLAS precision of this nature presents special challenges of spatial and alignment precision. From the term BL^2 (see Equation 2) it is clear that a large magnet is required. However it is not easy to generate a high field over a large volume. By considering Ampere's theorem we can estimate the current required, Now

$$2\pi RB = \mu_0 nI \Rightarrow nI = 20 \times 10^6 \text{ At}$$

$$\text{i.e. } 2.5 \times 10^6 \text{ At for 8 coils}$$

where n is the number of turns and I is the current. ATLAS employ $2 \times 2 \times 30$ turns leading to a current of $I=20 \text{ kA}$. Such currents can only be considered in the context of superconducting magnets.

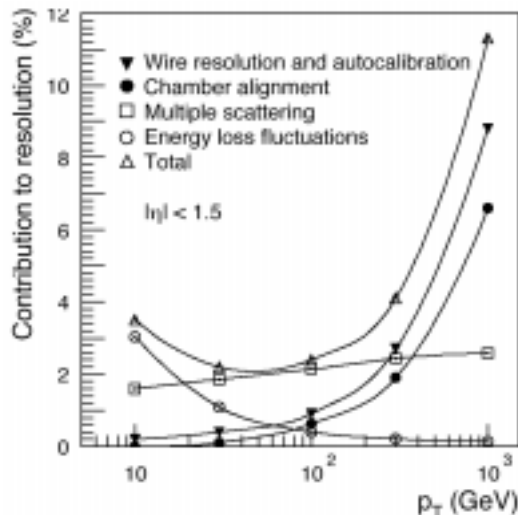


Figure 43: The various contribution to the momentum resolution for muon in the ATLAS detector.

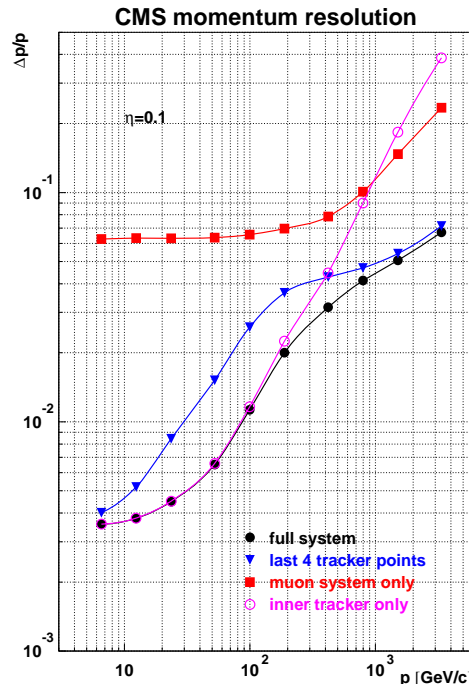


Figure 44: The muon momentum resolution using the the inner tracker and the muon system.

The basis of measurement in the barrel part of the ATLAS spectrometer is to measure a position on the muon trajectory before and after the magnet, and a third point between the other two.

$$\frac{\Delta p}{p} = 26.7 \sigma \sqrt{\left(\frac{1}{2N_1} + \frac{1}{N_2}\right)} \frac{p}{BL^2} \quad (\%)$$

where p is in GeV, B in T and σ, L is in m. In ATLAS $\sigma \approx 70 \mu\text{m}$, $N_1 \approx 6$, $B \approx 0.6 \text{T}$, $L \approx 4.5 \text{m}$ implying $\Delta p/p \approx 0.8 \%$ at 100 GeV which is very close to the value found in simulations.

The momentum resolution is limited by energy loss fluctuation in the calorimeters at small momenta and by detector resolution at high momenta, whereas multiple scattering effect is approximately momentum independent as can be seen in Fig. 43. The momentum resolution is typically 2-3% over most of the kinematic range apart from very high momenta, where it increases to $\approx 10\%$ at $p_t = 1 \text{ TeV}$.

8.3.2 CMS

A large $\int B \cdot dL$ can be obtained for a modest size using high field solenoids. The bending, which takes place in the transverse plane, starts at the primary vertex. For tracks which pass through the end of the solenoid the momentum resolution worsens as $L_c \cdot \tan\theta / r_c$ where L_c and r_c is the length and radius of the solenoid. The effect can be attenuated by choosing a favourable dimensional ratio (length/radius). For CMS coil, where a high magnetic field is chosen, the challenge lies in the production of a reinforced superconducting cable that can take an outwards pressure of about 60 atm.

The field generated in a solenoid is given by $B = \mu_0 n I$. For CMS with $B = 4 \text{T}$, $n = 2168$ implying that $I \approx 20 \text{ kA}$ again requiring superconducting technology.

Centrally produced muons are measured three times: in the inner tracker, after the coil and in the return flux. If multiple scattering and energy loss are neglected then the muon trajectory beyond the return yoke extrapolates back to the beam-line due to the compensation of the bending before and after the coil. This fact can be used to improve the momentum resolution at high momenta. The sagitta is given by perpendicular distance between the outermost inner tracking points and the line joining the beam to the muon beyond the return yoke. The muon momentum resolution is illustrated in Fig. 44.

6.3.3 Muon Detectors

Two kinds of muon detectors are used at LHC serving complementary purposes. These are gaseous drift chambers that provide accurate position measurement for momentum determination and ‘trigger’ chambers, such as resistive plate chambers, that have a short response ($\leq 25 \text{ ns}$) for precise bunch crossing identification but less accurate position measurement. The former category of detectors can also provide a first level-trigger on muons. In LHC GPDs the rate in the barrel region ($\approx 10 \text{ Hz/cm}^2$) is two orders of magnitude smaller than in the endcaps. This rate is due mainly to hits induced by photons from neutron capture. The neutrons are evaporation neutrons produced by breakup of nuclei in hadronic showers. Hence drift chambers are replaced by faster chambers such as cathode strip chambers. Since the dominant background is neutron induced which usually affecting two detecting layers, each of the muon stations comprises several (≈ 6) layers of detectors.

The operation of the gas chambers is discussed later.

9. INNER TRACKING

The most powerful way to ‘see’ the event topology is by using the inner tracker. The role of the inner tracker is to measure the momentum and impact parameter of charged tracks with minimal disturbance. The figures of merit are the track finding efficiency, the momentum resolution and the secondary vertex resolution. As described earlier the inner tracker plays a crucial role in the identification of electrons, taus and b-jets.

During the 60’s the bubble chamber was the detector of choice for tracking. However it was superseded by electronic detectors as HEP moved to the study of lower cross-section phenomena. The bubble chambers had a low repetition rate and lacked sufficient triggering capability. Recently large detectors such as ALEPH and DELPHI at LEP have used ‘electronic bubble chambers’ in the form of Time Projection Chambers (TPCs). These give 3-D spatial information with high granularity and some particle identification capability is in-built using dE/dx measurements. However these are not used in the LHC GPDs as the electron drift time is long (25-45 μ s). They are suitable for LEP as the event rate is low and the bunch crossing interval is large. The tracking detectors at the LHC have to deal with very high particle rates ($\approx 4 \cdot 10^{10}$ particles/s emerging from the interaction point) and very short bunch crossing time (25 ns). Furthermore the target momentum resolution for 100 GeV tracks is almost an order of magnitude better at the LHC than at LEP. Hence Si pixel and microstrip detectors, and short drift-time gaseous detectors (straw or MSGCs) are used.

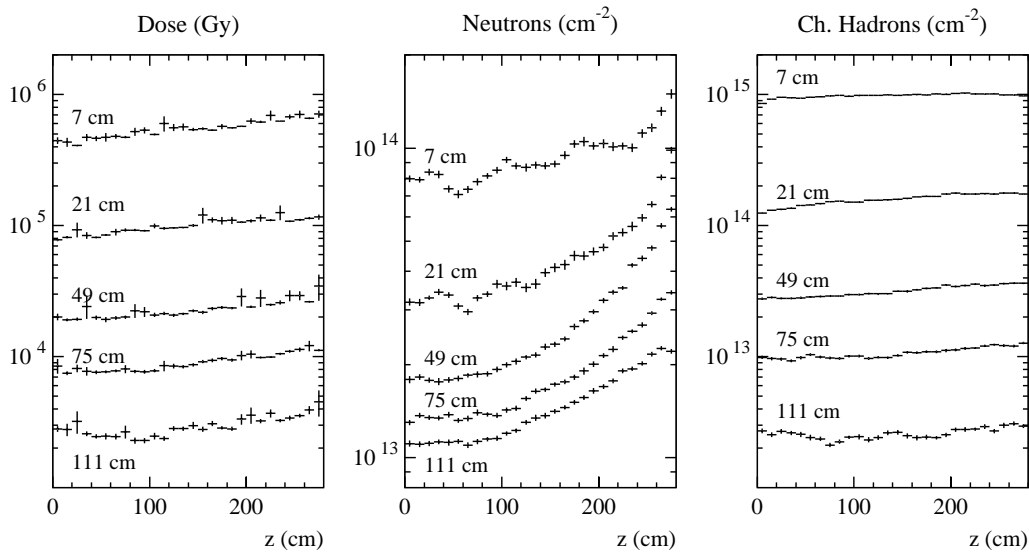


Figure 45: The integrated dose, neutron and charged hadron fluence in the inner tracking cavity for an integrated luminosity of $5 \cdot 10^5 \text{ pb}^{-1}$ corresponding to the first 10 years of LHC operation.

The radiation levels in the CMS tracking system are illustrated in Fig. 45 for an integrated running time of 10 years corresponding to $5 \cdot 10^5 \text{ pb}^{-1}$. Three regions can be delineated. Pixel detectors are placed closest to the interaction vertex where the particle flux is the highest. The typical size of a pixel is about $150 \mu\text{m} \times 150 \mu\text{m}$ leading to an occupancy of about 10^{-4} per LHC crossing. In the intermediate regions the particle flux is low enough to enable use of Si microstrip detectors with typical cell size of $10 \text{ cm} \times 75 \mu\text{m}$ leading to an occupancy of $\approx 1\%$ /LHC crossing. In the outermost regions of the inner tracker the particle flux has dropped sufficiently to allow

use of gaseous detectors. Typical cell size in CMS is $25\text{cm} \times 250 \mu\text{m}$ giving an occupancy of a few percent.

We shall now look at the operation of gaseous and semi-conductor detectors,

9.1 Gaseous Tracking Detectors

Fast charged particles ionise atoms of a gas. If W is the energy required to create an electron-ion pair then the total total number of electron-ion pairs is

$$n_{total} = \frac{\Delta E}{W} = \frac{dE}{dx} \frac{\Delta x}{W}$$

In fact $n_{total} \approx 3-4 n_{primary}$. Fig. 46 shows the number of primary electrons for various gases. For a gap of 1 cm of Argon about 100 electron-ion pairs are created. A signal consisting of only 100 electrons is not easy to detect as the noise of fast amplifiers tends to be $\approx 1000 e^-$'s. Hence one needs amplification in the gas. Consider a cylindrical cell, with grounded walls and a very thin anode wire placed at the axis. The electric field at a distance r from the wire can be calculated using Gauss' theorem and is given by

$$E(r) = \frac{CV_0}{2\pi\epsilon_0} \frac{1}{r}$$

Consider a charged track that traverses the cell (Fig. 47). The electrons from the electron-ion pairs drift towards the anode wire. Close to the wire the electric field is sufficiently high for the electrons to gain enough energy to ionise further atoms. This leads to an exponential increase in the number of e-ion pairs.

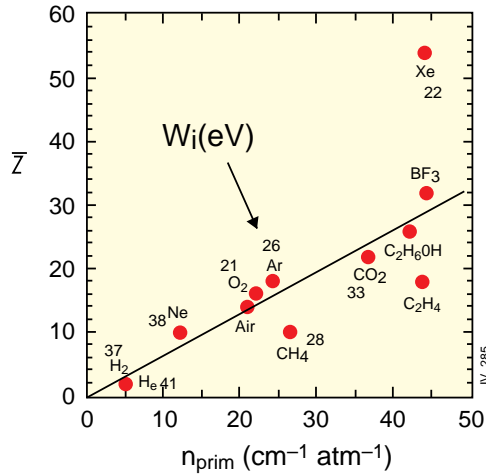


Figure 46: The number of primary clusters per cm in various gases.

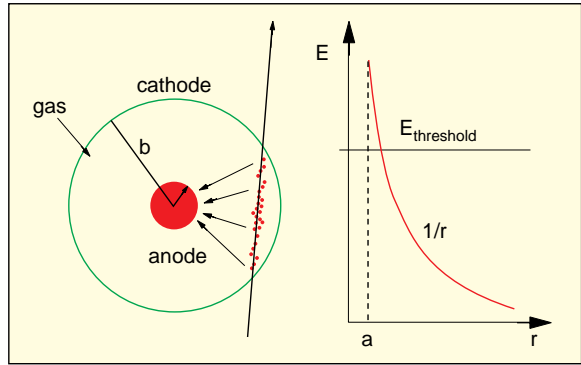


Figure 47: Schematic of a charged track traversing a cylindrical gas chamber (e.g. a straw tube).

The probability that an electron will produce an ionising collision with an atom in a distance dr is

$$N_a \sigma_i dr$$

where N_a is the no. of atoms/unit volume. The increase in the number of electrons after dr then is

$$dn = n N_a \sigma_i dr$$

Let $N_a \sigma_i = \alpha$. α is known as the 1st Townsend coefficient. The larger is the value of α the larger is the number of collisions per unit distance. The mean free path length (λ) between collisions can

be defined as $\alpha = 1/\lambda$. α is a function of r as it varies with electric field which usually varies with r . Hence

$$dn = n \alpha(r) dr$$

$$\therefore n = n_0 \exp \int_a^{r_c} \alpha(r) dr$$

where n_0 is the no. of electrons initially present. Therefore the gain, M , is given by

$$M = \frac{n}{n_0} = \exp \int_a^{r_c} \alpha(r) dr$$

In fact $M \propto e^{CV_0}$

It is interesting to calculate what happens near an anode wire. From Table 3 it can be deduced that 50% (90-%) of the electrons are produced ≈ 2.5 (10) μm from the anode wire.

Table 3: Values of various parameters that determine gain in gas wire-detectors.

r (μm)	E (kV/cm)	α (ip/cm)	$\lambda=1/\alpha$ (μm)
10	200	4000	2.5
20	100	2000	5
100	20	80	125
200	10	1	1 cm

9.1.1 Detector Gas Mixtures

Avalanche multiplication occurs in all gases. However gases should have the following properties: a low working voltage, stable operation at high gain, high rate capability, long lifetime and fast recovery. The principal component of a desirable gas is usually a noble gas such as argon. These allow multiplication at relatively low electric fields. They do not have molecules and hence the electrons only suffer elastic collisions with little loss of energy. Electrons can easily be absorbed by complex molecules. Argon is usually preferred as it gives more primary ionisation than He or Ne and is significantly cheaper than Kr or Xe. However a counter full of a noble gas (e.g. argon) does not allow stable operation. During the avalanche process many Ar atoms are excited and decay emitting UV photons (e.g. with an energy of 11.6 eV). These UV photons can strike the cathode (usually clad with copper which has an ionisation threshold of 7.7 eV) and eject photoelectrons which give rise to another avalanche. There is therefore a positive feedback and a continuous discharge sets in. A chamber filled with pure Ar suffers such breakdown at relatively low gain. Gases are added which ‘quench’ the secondary avalanches. Polyatomic gases have many non-radiative vibrational and rotational excited states over a wide energy range. If a chamber contains a fraction of such a gas, its molecules will absorb energy from excited argon atoms by colliding with them or by dissociating into smaller molecules. Since $\tau_{\text{emission}} \gg \tau_{\text{collision}}$ the UV photon emission is eliminated or quenched. The presence of a quenching gas can allow an enormous increase in stable gain obtainable. Isobutane (C_4H_{10}), methane (CH_4) and many hydrocarbons and alcohols are such gases.

9.1.2 Operation Modes of Chambers

We can look at various operation modes of gas chambers (Fig. 48) as the potential difference is increased [25]. At very low voltages electrons begin to be collected but *recombination* of electrons and ions is the dominant process. At higher voltages all the electrons and ions are collected and the chamber is said to operate in the *ionisation mode*. At a certain higher voltage called the threshold voltage (V_T) the electric field close to the surface of the anode is large enough to begin the process of *multiplication*. Increasing the voltage (V_0) beyond V_T results in gains $\geq 10^4$ with the detected charge being proportional to the deposited energy. The chamber is said to operate in the *proportional mode*. At even higher voltages the proportionality is gradually lost due to the distortion of the electric field caused by space charge around the anode (*limited proportionality mode*). The region of limited proportionality eventually ends in a region of saturated gain i.e. the size of the signal is the always the same i.e. independent of the initial deposition of energy. The chamber is said to operate in the *Geiger mode*.

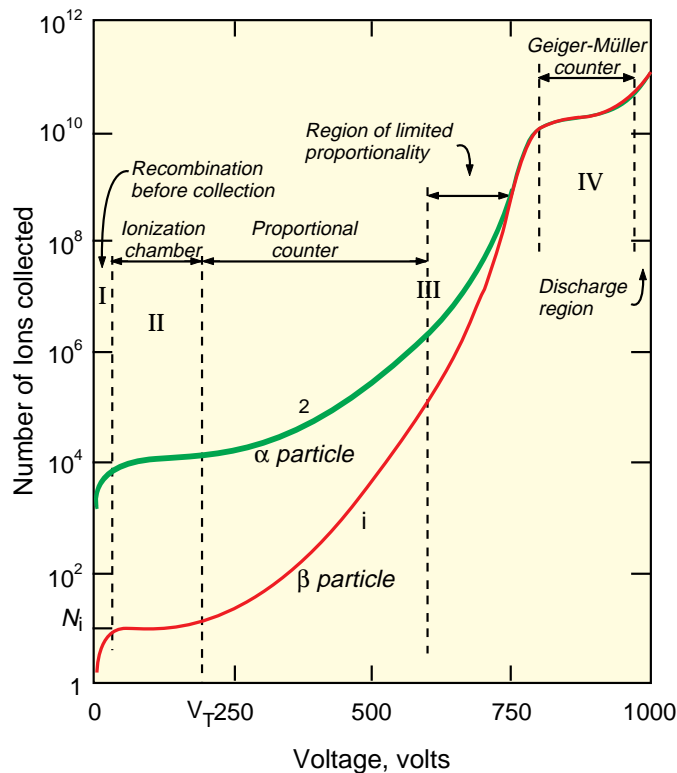


Figure 48: The various modes of operation of gas wire detectors.

9.1.3 Time development of the Signal

Consider a single primary electron drifting towards the anode (at ≈ 5 cm/ μ s) and into the region of increasingly high electric field (Fig. 49). At a radius of typically a few wire radii the electric field becomes large enough for the primary electron to gain enough energy to cause ionisation. Due to lateral diffusion a drop-like avalanche surrounding the wire develops. The whole process of exponential avalanche multiplication lasts ≈ 1 ns. The electrons are collected very fast (in ≈ 1 ns) as the drift distance is only a few microns. The positive ions drift slowly towards the cathode. However *the signal on the electrodes is induced by the movement of charges*. Since the electrons move a very short distance they induce a very small signal. The size and time development of the induced signal is determined by the ion drift. It is given by:

$$I(t) = \frac{Q}{2t_0 \ln(b/a)} \left(\frac{1}{1+t/t_0} \right)$$

where t_0 is the characteristic time. For example, the total drift time for ions in Ar at NTP is 550 μs for $a = 10\mu\text{m}$, $b = 8\text{mm}$, $C = 8 \text{ pF/cm}$, $\mu^+ = 1.7 \text{ cm}^2\text{V}^{-1}\text{s}^{-1}$, $V_0 = 3\text{kV}$. The growth time is very fast (1/1000 of the total drift time). The normal practice is to terminate the counter with a resistor R such that the signal is differentiated with a time constant RC allowing very short pulses. A high rate capability is therefore possible.

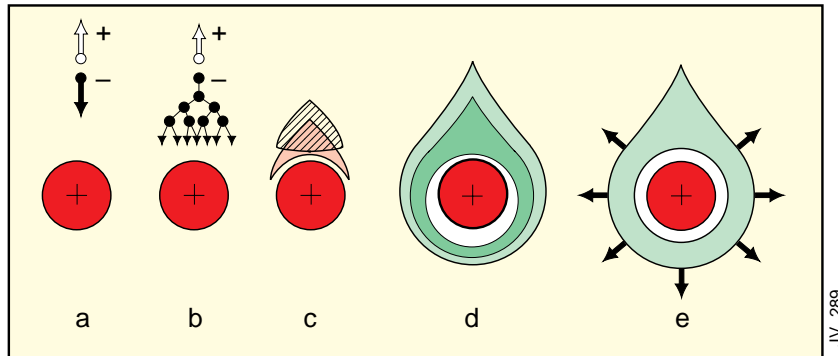


Figure 49: The schematic drawing of the development of an avalanche in a wire chamber.

9.1.4 Drift Chambers

The working of a drift chamber is illustrated in Fig. 50. The electrons liberated along the path of the charged track drift towards the anode wire. The spatial information is obtained by measuring the time of drift of electrons. The traversal of the particle is signaled by a scintillator or by the bunch crossing time in collider experiments. The stop on a TDC is given by the arrival of the electrons. The cell size in drift chambers is much larger than in multi-wire proportional chambers thus relatively fewer number of wires and electronics channels are needed.

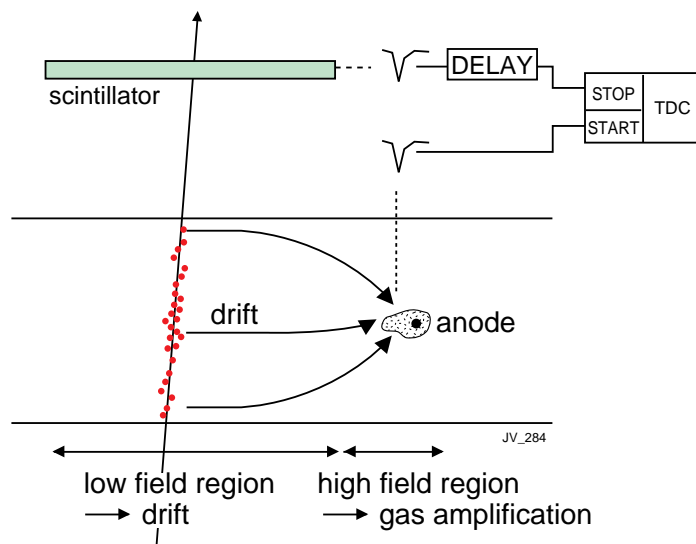


Figure 50: The principle of operation of a drift chamber

The desired properties of the gases used in drift chambers are listed below:

- the gas should have a high purity - electrons can be captured if electro-negative impurities

are present. The longer the drift path length the higher the required level of purity.

- the gas should exhibit saturation of drift velocity i.e. drift velocity that is constant over small voltage shifts away from the working voltage. The precision then becomes insensitive to field inhomogenieties, changes in voltage and temperature etc.

- the gas should be fast for high counting rate. The maximum counting rate is limited by the total drift time.

Below we consider two drift chambers; the monitored drift tubes (MDTs) used in the ATLAS and drift tubes (DTs) used in the CMS muon system.

The MDTs are cylindrical aluminium tubes with a length of about 5 m, a diameter of 3 cm and a wall thickness of $400\mu\text{m}$ with a $50\mu\text{m}$ diameter central W-Re wire. The tubes are operated with a non-inflammable $\text{Ar-CH}_4\text{-N}_2$ (91%-5%-4%) gas mixture at a pressure of 3 bars. The wire is set at a potential of $\approx 3300\text{V}$ and the electric field at the wire is $\approx 200\text{ kV/cm}$ yielding a gain of about 20,000. The maximal drift time is $\approx 500\text{ns}$. The distance-time relation is shown in Fig. 51a and good linearity is achieved over almost the full drift path. The measured resolution is $\approx 80\mu\text{m}$ (Fig. 51b).

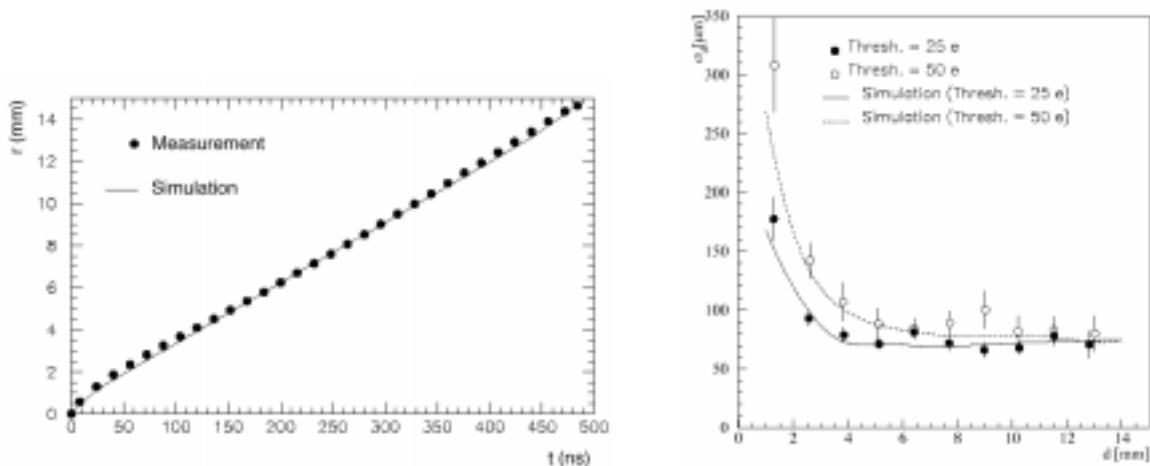


Figure 51: a) The distance-time relation and b) the measured position resolution for the ATLAS MDTs.

The layout of the CMS muon DT cell is illustrated in Fig. 52. Three field-shaping electrodes are employed to assure a linear distance-time relationship. The side cathode is set at $\approx 1800\text{V}$, the top and bottom strips at $\approx 1800\text{V}$ and the wire is run at $\approx 3600\text{V}$. The gain is about 90,000. The gas mixture is Ar-CO_2 (85%-15%). The drift velocity as a function of the electric field is shown in Fig. 53. The measured resolution is found to be $\approx 200\mu\text{m}$ (Fig. 54)

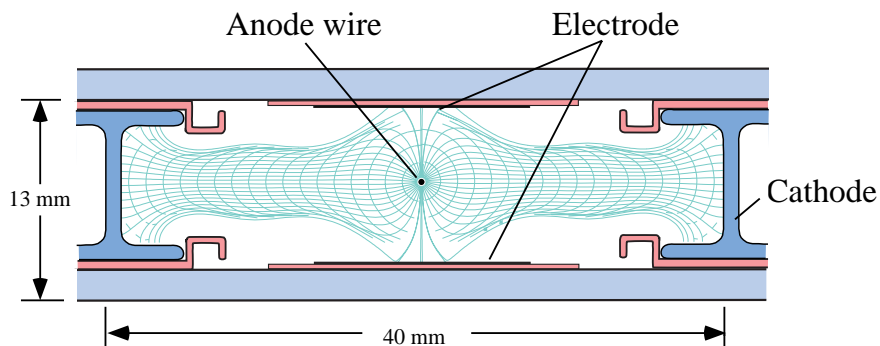


Figure 52: The layout of the drift cell of the CMS drift tubes

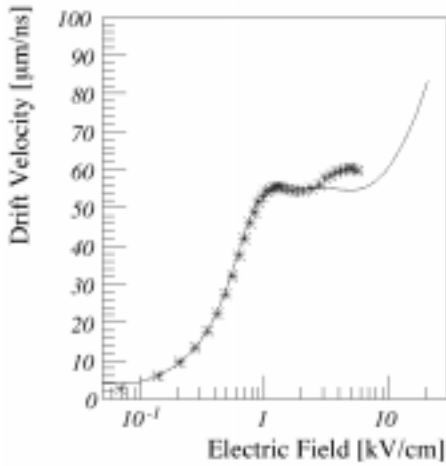


Figure 53: The drift velocity as a function of the electric field in Ar-CO₂. The calculated one is shown as a line.

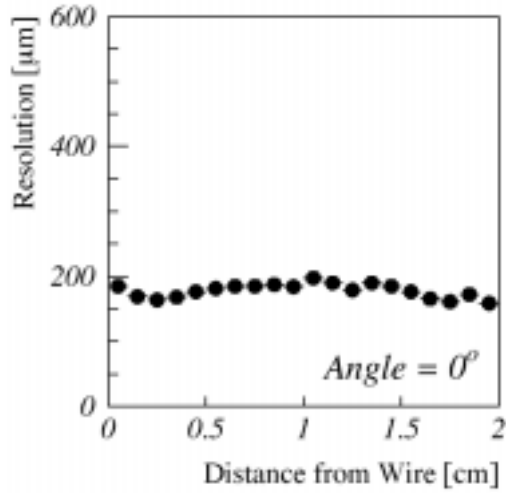


Figure 54: The measured position resolution in the CMS drift tubes.

9.1.5 The Time Projection chamber

The time projection chamber (TPC) is a 3-D imaging drift chamber. An example is the ALEPH TPC illustrated in Fig. 55 [26]. It consists of a large gas filled cylinder with a thin HV electrode in the middle plane. The magnetic and electric fields are parallel, uniform and along the axis. The ends of the cylinder are covered by sector arrays of proportional anode wires. Parallel to each wire are rectangular cathode pads.

The ALEPH TPC has a diameter of 3.6 m and a length of 4.4m. It is filled with Ar-CH₄ (91%-9%) at atmospheric pressure. The electron drift time is 45 μs. The r-φ coordinate is obtained by interpolating signals induced on precisely located cathode pads (6.2mm×30mm) and the z coordinate from the drift time. Particle identification for low momenta particles can be achieved by using the dE/dx information. Diffusion is significantly reduced by the axial magnetic field and the performance is improved by laser calibration. Various systematics are removed by making straight line fits to trails of ionisation caused by laser beams shot into the gas volume. The performance is given by:

$$\sigma_{R\phi} \approx 170 \mu\text{m}, \sigma_z \approx 750 \mu\text{m} \text{ and } \frac{\sigma_{p_t}}{p_t} \approx 0.1p_t \oplus 0.3 (\%)$$

where p_t is in GeV.

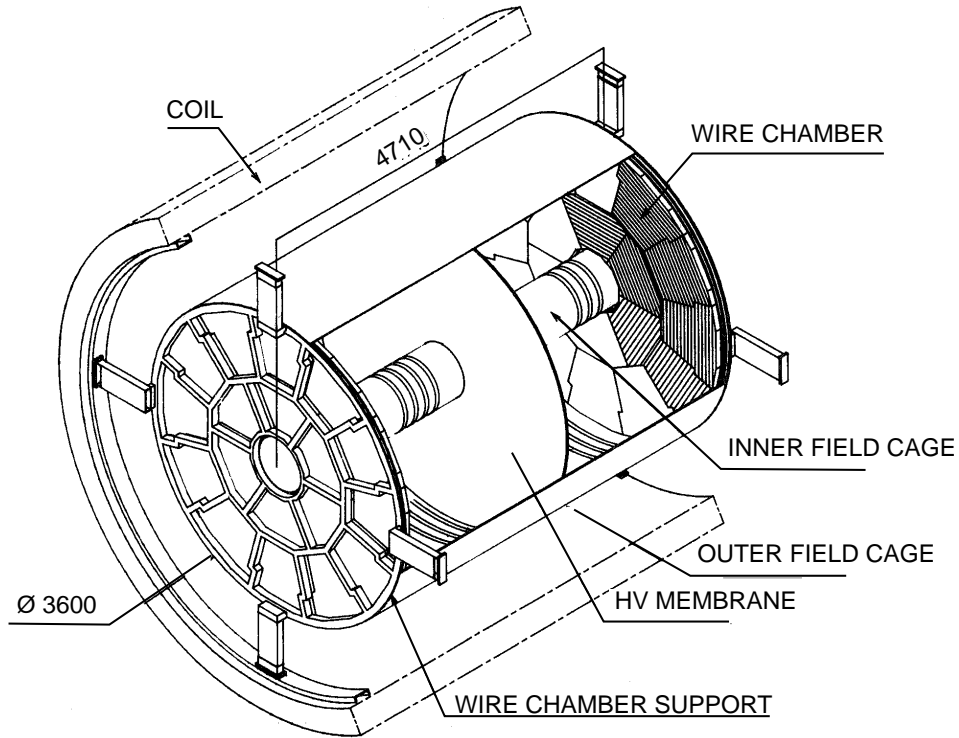


Figure 55: The illustration of the ALEPH time projection chamber.

9.1.6 Microstrip Gas Detectors

Microstrip gas chambers (MSGCs) are made using micro-electronics technology where the precision of photo-lithography is $\approx 0.1\text{-}0.2 \mu\text{m}$ [27]. This allows the overcoming of two major limitations of multi-wire proportional chambers (MWPCs). The spatial resolution in MWPCs, orthogonal to the wire is limited by wire spacing. The limit is around 1mm due to mechanical and electrostatics considerations. The rate capability of MWPCs is limited by the long ion collection time that is typically several tens of μs .

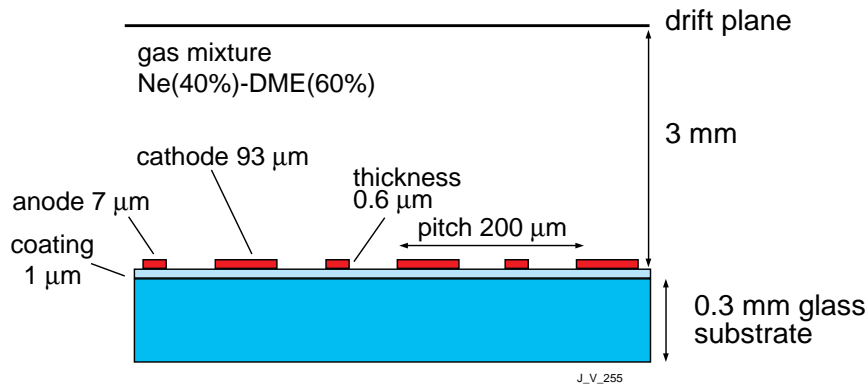


Figure 56: The principle of operation of a microstrip gas chamber.

The MSGC is a miniaturized version of a MWPC. The principle of operation of an MSGC is illustrated in Fig. 56. The wires are replaced by thin strips imprinted on an insulating support e.g. glass to prevent the electrostatic forces from distorting or breaking them. Hence their spacing and width can be reduced. The cathode and anode strips are laid on the substrate over which is placed a planar electrode generating the drift field. The gas gap between the substrate and the drift

electrode is usually about 3mm. The MSGCs have been operated up to rates of 10^6 particles/mm²/s.

For the chambers to be used in CMS the drift plane is set at $-3500V$, the cathode at around $-520V$ and the anode is grounded. The primary electrons drift along the uniform electric field (Fig.57) until they get close to the anode where multiplication takes place. A major advantage of the MSGC is the much faster signal development since the ions have only to drift the short distance of about $60 \mu m$ from the anode to the cathode as shown in Fig. 58.

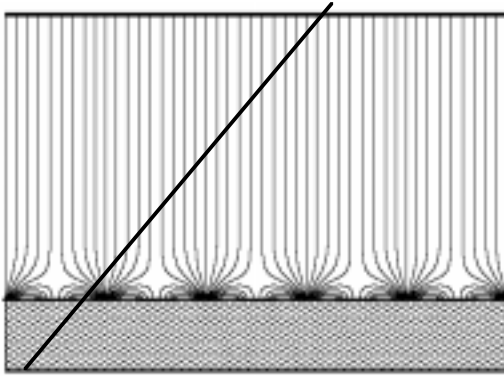


Figure 57: Illustration of the drift field lines.

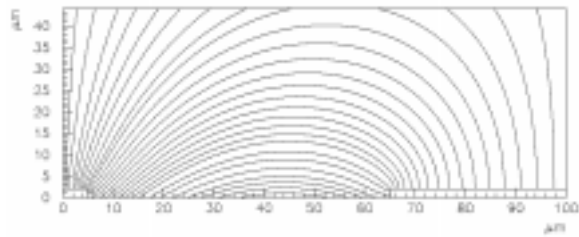


Figure 58: The drift path of ions.

Many parameters can significantly affect the performance. Coating the surface of glass with resistive coating (e.g. Pestov glass with $r \approx 10^{16} \Omega/cm^2$) stops charging-up of the substrate at high rates and renders the detector independent of the bulk electrical characteristics of the substrate. Strips have to be made out of gold to slow aging and decrease attenuation of the collected charge along the strips if they are long. A reduction in the maximum operating voltage for MSGCs exposed to heavily ionising tracks and at high rates has been observed. A proposed solution is to passivate the cathode edges and has been adopted by CMS.

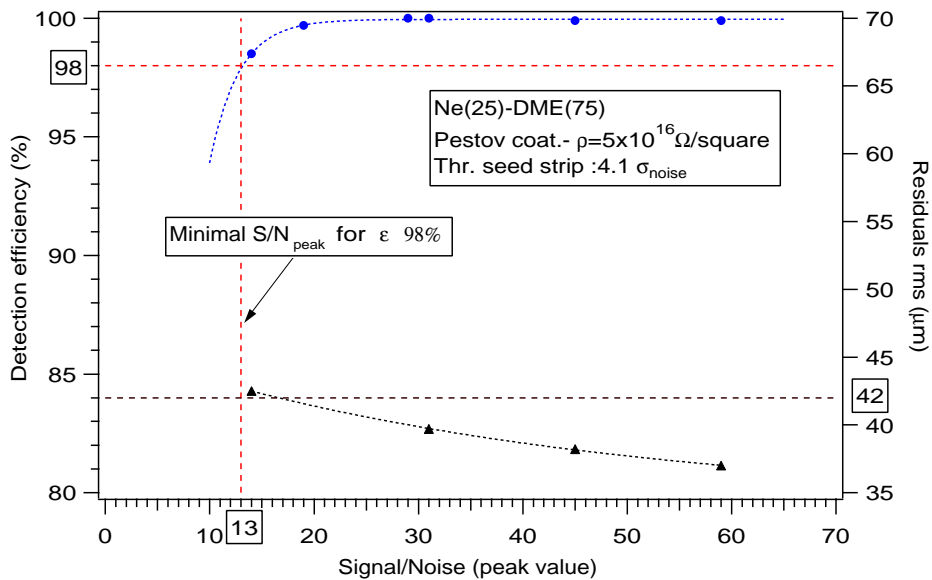


Figure 59: The measured performance of the CMS MSGCs.

The gas mixture used by CMS is Neon-DiMethylEther (40%-60%). DME generate a large number of primary clusters (60 clusters/cm and 180 electrons/cm for a mip). From many points of view 100% DME would be the best gas but it would require a cathode voltage too close to the breakdown voltage. The performance of CMS chambers with an anode-cathode pitch of 200 μm is shown in Fig. 59.

The average cluster size is over 2 and a resolution of about 45 μm can be achieved by using the centroid of the charge deposition.

In a more recent development, the Gas Electron Multiplier (GEM [28]) the gain is achieved in two stages. The first stage of amplification is carried out in a thin polymer foil (kapton), metal-clad on both sides and perforated with a high density of holes with photo-lithographic processing. When a suitable potential difference is applied between the two sides, the field in the hole is large enough to allow multiplication. The second stage can be a conventional MSGC. This is illustrated in Fig. 60. The MSGC can then be operated at a lower voltage promising a wider margin for safe operation as illustrated in Fig. 61.

Much research is still being carried out on the miniaturized gas chambers.

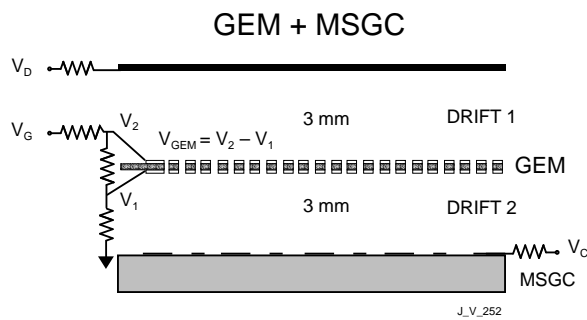


Figure 60: Schematic drawing of GEM+MSGC 2-stage gas microstrip detector

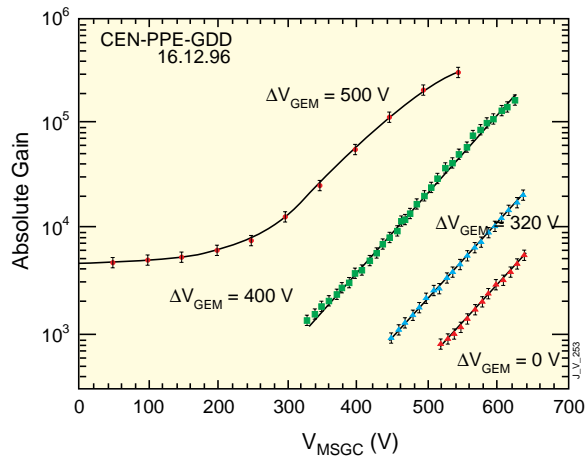


Figure 61: The various combinations of GEM and MSGC potential difference for a given gain.

9.2 Silicon Detectors

Solid state detectors have long been used for the measurement of low energy photons. When used for tracking they have several advantages :

- a large number of carriers are produced. Charged particles traversing Si create electron-hole (e-h) pairs. It takes about 3.6 eV of deposited energy to create an e-h pair compared with about 30 eV to create e-ion pair in gas detectors. The typical thickness of Si detectors is about 300 μm leading to the creation of about $3 \cdot 10^4$ e-h pairs on average. This is large enough not to require multiplication.

- the mobility of electrons and holes is 1450 and 450 cm^2/Vs respectively. The typical operating voltage is $\approx 100\text{V}$ and both the electron and hole charges drift to the respective electrodes within 10 ns. Hence silicon detectors have a fast response and both charge carriers equally induce the detected pulse.

- microelectronic techniques are used for the production of silicon detectors. Silicon detectors therefore have small pitch ($\geq 50\mu\text{m}$) but strip lengths are usually limited in length ($\leq 12\text{cm}$).

9.1.7 Signal generation in Silicon Detectors

The energy levels of atoms become energy bands in a regular assembly of atoms such as crystals.

Valence and conduction bands of energy levels are formed in crystalline materials due to the periodic lattice structure. In the valence band the electrons are bound to specific lattice sites whereas in the conduction band they are free to move through the crystal. At non-zero temperatures it is possible for valence electrons to get enough energy to get into the conduction band (the band gap energy is 1.12 eV). In a pure intrinsic (undoped) material the electron density, n , and the hole density, p , are equal i.e. $n_i = p_i$. For silicon $n_i = 1.45 \times 10^{10} \text{ cm}^{-3}$. Hence in a silicon detector with an area of 1 cm^2 and a thickness of $300 \mu\text{m}$ there are 4.5×10^8 free charge carriers but only $\approx 3.10^4$ e-h pairs are created by the passage of a mip. For the signal to be significant the number of free charge carriers has to be considerably reduced. This is done by 'depleting' the detector using reverse biased p-n junctions.

The p-n junction is made by doping to create *p-type* and *n-type* silicon.

Silicon sits in Group IV of the periodic table i.e. it has 4 outer electrons and can form 4 covalent bonds. If a small concentration (few ppm) of a pentavalent impurity (e.g. P or As) is added one electron is left over after all the covalent bonds are formed. It is very lightly bound and can easily be promoted to the conduction band without creating a corresponding hole. P or As are known as *donor* impurities. Donor electrons are not part of the regular lattice and can occupy a position in the normally forbidden gap (near the top of the gap). Thermal excitation is sufficient to ionize a large fraction of the donors (N_D) and $n = N_D$. The added concentration of electrons increase the rate of e-h recombination shifting the equilibrium between electrons and holes. The concentration of holes decreases but

$$n p = n_i p_i$$

e.g. at room temperature, $n_i = p_i = 10^{10} \text{ cm}^{-3}$ and if donor impurities are $N_D \approx 10^{17} \text{ atoms/cm}^3$, $n = 10^{17} \text{ cm}^{-3}$ and $p = 10^3 \text{ cm}^{-3}$. Charge neutrality is maintained by the presence of ionized donor impurities which cannot migrate as they are fixed to the lattice sites.

If a small concentration (few ppm) of trivalent impurity (e.g. B) is added there is one fewer electron and one covalent bond is left unsaturated. The vacancy represents a hole. Other electrons can be captured to fill this vacancy but are on the whole less firmly bound to the specific sites. are formed. Such impurities are labeled *acceptor* impurities. These lie near the bottom of the forbidden gap. Thermal excitation always assures that electrons are available to fill the vacancies. Hence a large fraction of the acceptor sites are filled i.e.

$$p \approx N_A \quad \text{with} \quad n p = n_i p_i \quad \text{and} \quad p \gg n$$

A measure of impurity level is the electrical *conductivity* or its inverse *resistivity* e.g. an impurity concentration of $10^{13} \text{ atoms/cm}^3$ leads to a resistivity of $500 \Omega \cdot \text{cm}$.

Heavily doped materials with an unusually high impurity concentration are labeled n^+ or p^+ and have a high conductivity. Such doping is often used for electrical contacts.

Consider now the formation of a p-n junction. Start with a wafer of *p-type* crystal with an original acceptor concentration N_A . Assume that one side is left exposed to the vapour of *n-type* impurity so that the left side becomes *n-type*. The density of electrons in *n-type* material is much higher than in the *p-type* one. There is a net diffusion of conduction electrons into *p-type* material where they quickly recombine with holes. The electrons moving out of *n-type* material leave immobile +ve charges and net -ve charge on the p-side is established. The accumulated space charge creates an electric field that diminishes the tendency for further diffusion. The region over which the imbalance exists is called the *depletion region*. The concentration of electrons and holes in this region is $\approx 100/\text{cm}^3$! In our case the region will extend deeper into p-side than the n-side. For electron-hole pairs created in the depletion region electrons will be swept towards the *n-type* material and the holes towards the *p-type*. The application of reverse bias (n-side made +ve) extends the depletion region and the depletion depth is given by

$$d \cong \sqrt{\frac{2\varepsilon V}{eN}} \quad \text{and in PDG } d \approx 0.5(0.3)\mu\text{m} \times \sqrt{\rho V} \quad \text{for } n\text{-type (p-type)}$$

where N is the lower dopant concentration, ρ is the resistivity (typically between 1-10 k Ω .cm). Typically for $d \approx 300\mu\text{m}$ and $\rho = 5 \text{ k}\Omega\text{.cm}$ the bias voltage is $\approx 70\text{V}$.

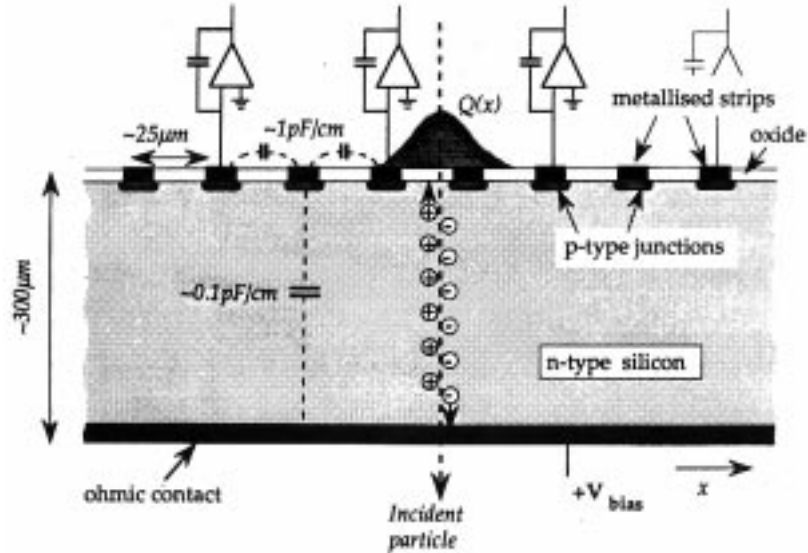


Figure 62: Schematic of a silicon microstrip detector.

1.1.3 Radiation Damage in Silicon Detectors

There are two types of effects that take place in silicon after high levels of irradiation: surface and bulk. The bulk damage is more important than surface damage. High energy hadrons interacting with nuclei, requiring a transfer of only $\approx 15\text{eV}$, can displace Si atoms from their lattice positions. The simplest defects are *vacancies* where a Si atom is absent from its site and *interstitials* where a Si atom occupies a position intermediate between other atomic sites. Disruption of the crystal symmetry leads to the formation of unwanted energy levels in the forbidden gap. The presence of these energy levels considerably increases the leakage current in radiation damaged detectors. The volume current density is observed to increase linearly with particle fluence with

$$\frac{\Delta I}{V} = \alpha \phi$$

where V is the volume (in cm^3), ϕ is the fluence in particles/ cm^2 and $\alpha = 2.10^{-17} \text{ A/cm}$ for minimum ionizing protons and pions after long term annealing.

The ultimate limit to detector lifetimes is given by significant changes in the substrate dopant density during and after irradiation. This effect is poorly understood. The substrate eventually becomes *p-type* irrespective of the initial type. This is shown in Fig. 63. The depletion voltage initially decreases and then increases without limit with increasing particle fluence. Partially depleted detectors can still operate but the charge collection in the undepleted volume is slow and occurs with reduced efficiency due to trapping of electrons. The dopant changes continue after irradiation has stopped BUT can be arrested if the detectors are kept below 0°C . The manufacture of Si detectors has improved substantially and high voltage operation (bias voltage $\geq 500 \text{ V}$) is nowadays possible. It is expected that Si microstrip detectors can be operated to fluences beyond a few times 10^{14} cm^{-2} .

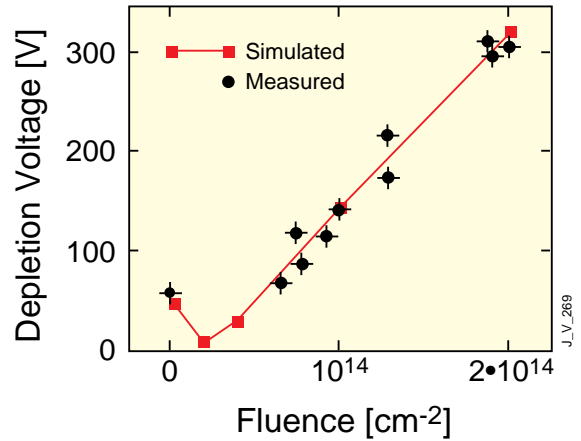
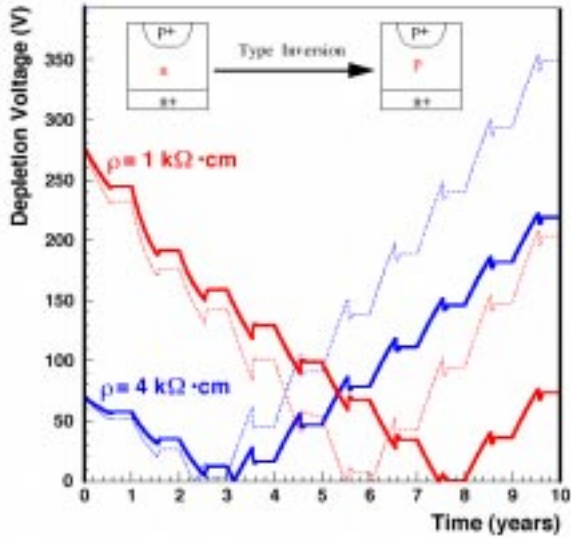


Figure 63: a) The bias voltage to achieve full depletion as a function of running time at the LHC at high luminosity

b) the bias voltage to achieve full depletion as a function of the neutron fluence.

With increasing particle fluence the depletion voltage increases without limit. To obtain a detailed picture of the signal loss after irradiation we consider Si pixel detectors irradiated with pions of 300 MeV/c at extremely small angles. The thickness of the Si was 300 μm and the size of the pixels was $125 \mu\text{m} \times 125 \mu\text{m}$, Effects due to charge trapping can be separated from charge lost due to reduced depletion depth. The method and results are illustrated in Fig. 64.

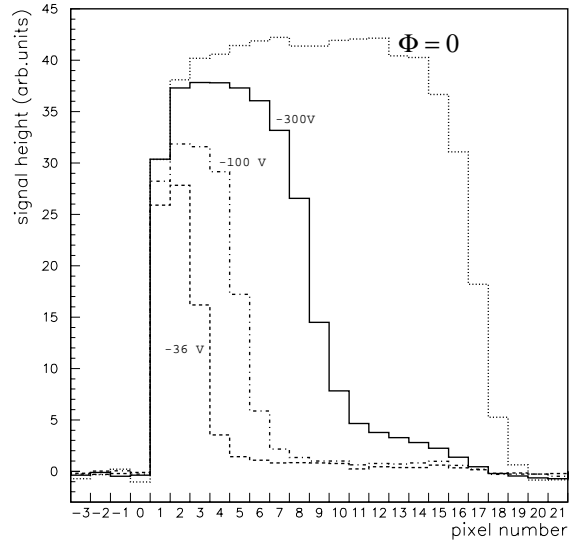
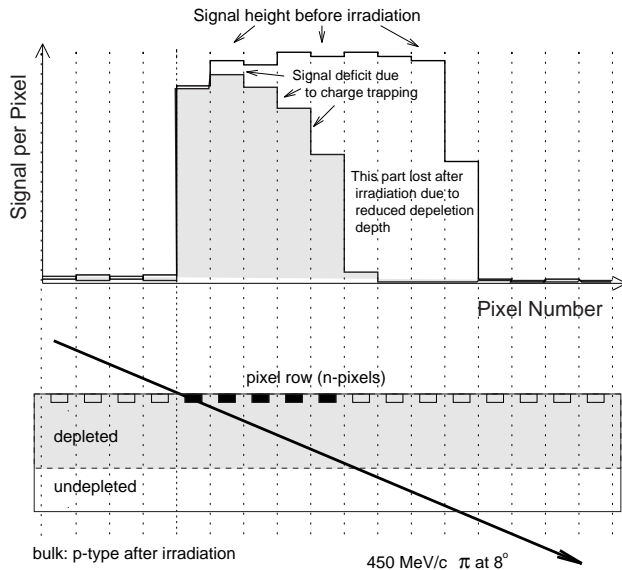


Figure 64: Minimum ionising pions (450 MeV/c) graze the pixel array at an angle of 8° (bottom). The signals from the hit pixel row exhibit the response of pixels at various depths (top). Each pixel sense a depth of $17.5 \mu\text{m}$.

b) Depth profiles of charge collected from the array irradiated with $6 \cdot 10^{14}$ pions/cm². The dotted histogram is for the un-irradiated array.

The detector was kept at 3°C and was irradiated to $6 \cdot 10^{14}$ pions/cm². Twenty days after irradiation the signals from various pixels were measured. The reduced depth of the depletion can clearly be discerned from the pixels that yield little or no charge. The decrease in signal with increasing depth of traversal is due to trapping of charge in the depleted region. The trapping of charge can be kept below $\approx 10\%$ by applying a high bias voltage.

10. ELECTRONICS NOISE

Noise is any unwanted signal that obscures the desired signal. Therefore noise degrades the accuracy of the measurement. There are two types of noise: *intrinsic* and *extrinsic* noise. The intrinsic noise is generated in the detector or electronics and cannot be eliminated though possibly reduced. The extrinsic noise is due to pickup from external sources or unwanted feedback (e.g. ground loops, power supply fluctuations etc.) and is usually eliminated by proper design.

Intrinsic noise has two principal components namely :

- thermal noise (Johnson or Nyquist noise) – *series noise*

Any resistor, R , will develop a voltage across its ends whose average value is zero but r.m.s. is

$$\langle v^2 \rangle = 4ktR\Delta f$$

- shot noise – *parallel noise*

This source arises from fluctuation in the charge carriers and is given by

$$ENC^2 = \frac{4ktR_s(C_d + C_{in})^2}{\tau} I_s + I_n \tau I_p$$

where C_d is the detector capacitance, C_{in} is the input capacitance of the amplifier, I_n is the leakage current, τ is the shaping time and I_s , I_p are series and parallel noise integrals (≈ 1 for $(RC)^2$ shaping). For example, for $\tau = 50$ ns, and a leakage current of $1 \mu\text{A}$, $ENC \approx 800$ electrons. Further examples are considered in Sections 9.3 and 10.2.

10.1 Electronics for LHC Experiments

The main components of electronics systems are:

- front-end, signal processing,
- data transmission,
- power supplies, services, ...

The features that differentiate the electronics of the LHC experiments from e.g. LEP experiments are:

- high speed signal processing
- signal pileup
- high radiation levels
- larger number of channels (large data volume),
- new technologies

For example the challenges for the inner tracker electronics are:

- signals are small and fast response must be preserved. Hence long leads cannot be used and the preamplifiers must be mounted on the detectors themselves.

- the data must be held in pipeline memories awaiting Level-1 decision. It is not feasible to transfer data off of the detector at a rate of 40 million events/s for millions of channels. Hence the pipeline memories must be located on the detectors. Consideration has to be given to how the signals are taken out.

- the several millions of channels will dissipate a considerable amount of heat (power dissipation has to be kept as low as possible; the goal is \leq few mW/channel). This leads to the question of how the electronics are cooled.

The above leads to difficult engineering and systems challenges. All this has to be accomplished whilst keeping the amount material in the tracker to the minimum to minimize multiple scattering

and conversion or bremsstrahlung.

10.1.1 Electronics of Sub-detectors

The characteristics and requirements for the electronics for the various sub-detectors can be summarized as follows:

tracking: large number of channels ($\approx 10^7$'s of millions), limited energy precision and limited dynamic range (< 8 -bits). The power dissipation/channel has to be low ($\approx \text{mW/ch}$) and the electronics have to withstand very high radiation levels (neutron fluence of 10^{15} n/cm^2 , integrated doses of 10^7 's of Mrads).

calorimetry: : medium number of channels ($\approx 10^5$), high measurement precision (12-bits), large dynamic range (16 to 17-bits), very good linearity and very good stability in time. The power constraints and the radiation levels ((neutron fluence of 10^{13} n/cm^2 , integrated doses of 100's of krad) are not as stringent as for the tracker.

muon system: the large surface area that needs to be instrumented means that the electronics are distributed over large area and the radiation levels are low.

The generic LHC readout system is illustrated in Fig. 66.

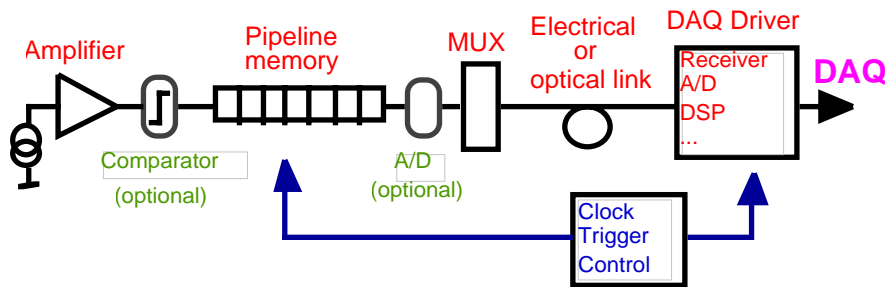


Figure 66a: A generic readout system for a p-p experiment at the LHC.



Figure 66b: The deconvolution of the signal of a silicon detector. The amplifier has a time constant of 50ns.

The functions that are common to all systems are amplification, analogue to digital conversion, association to beam crossing, storage prior to trigger, deadtime-free readout, zero suppression and formatted storage prior to access by the data acquisition, calibration control and monitoring. Most of these features can be illustrated by using as an example the microstrip tracking electronics chain of CMS. The scheme is illustrated in Fig. 67.

Each microstrip is read-out by a charge sensitive amplifier with $\tau=50 \text{ ns}$. The output voltage is sampled at the beam crossing rate of 40 MHz. Samples are stored in an analogue pipeline for up to the Level-1 latency of $\approx 3.2 \mu\text{s}$. Following a trigger a weighted sum of 3 samples is formed in an analog circuit. This confines the signal to a single bunch crossing and gives the pulse height (Fig. 66b). The buffered pulse height data are multiplexed out on optical fibres. The output of the transmitting laser is modulated by the pulse height for each strip. The light signals are transformed into electrical pulses by a Si photodiode and digitized. After some digital processing (zero suppression etc.) the data are formatted and placed into dual port memories for access by the data acquisition. The electronics noise/channel of the tracking system is about 1000 to 1500

electrons before and after irradiation respectively.

The calorimeter and muon systems have also to generate the primitives (energy or momentum values) for the first-level trigger.

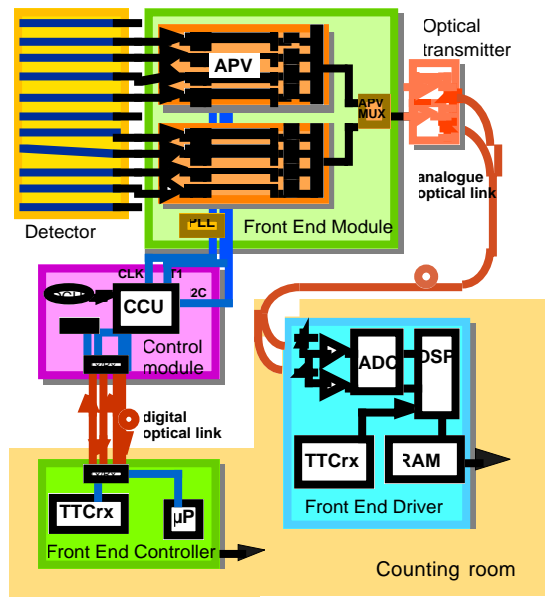


Figure 67: Schematic of the CMS Tracker readout and control system

11. INORGANIC SCINTILLATORS

The desirable properties of a scintillator include:

- a high efficiency of conversion of deposited energy into scintillation light,
- a conversion to light that is proportional to the energy deposited,
- a high light output,
- a medium that is transparent to its emitted light,
- a short luminescence decay time,
- a refractive index $n \approx 1.5$ for efficient coupling to photosensors
- radiation hardness for LHC operation.

No material simultaneously meets all these criteria. Inorganic scintillators (e.g. sodium iodide) have the best light output and linearity whilst organic scintillators (e.g. plastic scintillator) have faster light output but smaller light yield and display saturation of output for radiation with high linear energy transfer. Two types of light emission are possible: *fluorescence* resulting in prompt emission of light in the visible wavelength range and *phosphorescence* resulting in slower emission of light at longer wavelengths. In particle physics inorganic scintillators are only used for electromagnetic calorimetry.

The most demanding physics channel for an electromagnetic calorimeter at the LHC is the two-photon decay of an intermediate-mass Higgs boson. The background is large and the signal width is determined by the calorimeter performance. The best possible performance in terms of energy resolution is only possible using fully active calorimeters such as inorganic scintillating crystals.

Inorganic scintillators have crystalline structure. The valence band contains electrons that are bound at the lattice sites whereas electrons in the conduction band are free to move throughout the crystal. Usually in a pure crystal the efficiency of scintillation is not sufficiently large. A small amount of impurity, called an activator, is added to increase the probability of emission of visible

light. Energy states within the forbidden gap are created through which an electron, excited to the conduction band, can de-excite. Passage of a charged particle through the scintillator creates a large number of electron-hole pairs. The electrons are elevated to the conduction band whereas the +ve holes quickly drift to an activator and ionize it. The electrons migrate freely in the crystal until they encounter ionised activators. The electrons drop into the impurity sites creating activator excited energy levels which de-excite typically with $T_{1/2} \approx 100$ ns. In a wide category of materials the energy required to create an electron-hole pair is $W \approx 3E_g$ e.g. in sodium iodide (NaI), $W \approx 20$ eV. In thallium doped sodium iodide [NaI(Tl)] the number of emitted photons $N_\gamma \approx 40000/\text{MeV}$ with an energy of ≈ 3 eV.

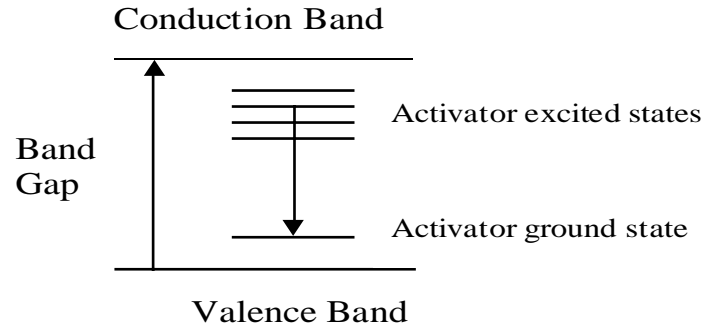


Figure 26: The energy level diagram for a scintillating crystal containing an activator

The consequence of luminescence through activator sites is that the crystal is transparent to its own scintillation light because the emission and absorption bands do not overlap and self-absorption is small. The shift towards longer wavelengths is known as *Stokes' shift*.

The scintillation mechanism in crystals without activators is more complex. For example, in lead tungstate the intrinsic emission in the blue is through excitons localized on the Pb site whereas the green emission is due to defects in the crystalline structure linked to oxygen vacancies [29].

The properties of various crystals used in high energy experiments are given in Table 3. The parameters of some of the recently designed crystal calorimeters are given in Table 4 [30].

Table 3: Properties of various scintillating crystals.

Crystal		NaI(Tl)	CsI(Tl)	CsI	BaF ₂	BGO	CeF ₃	PbWO ₄
Density	g.cm ⁻²	3.67	4.51	4.51	4.89	7.13	6.16	8.28
Rad. length	cm	2.59	1.85	1.85	2.06	1.12	1.68	0.89
Molière radius	cm	4.5	3.8	3.8	3.4	2.4	2.6	2.2
Int. length	cm	41.4	36.5	36.5	29.9	22.0	25.9	22.4
Decay Time	ns	250	1000	35	630	300	10-30	<20>
				6	0.9			
Peak emission	nm	410	565	420	300	480	310-340	425
				310	220			
Rel. Light Yield	%	100	45	5.6	21	9	10	0.7
				2.3	2.7			
d(LY)/dT	%/°C	≈ 0	0.3	- 0.6	- 2.0	- 1.6	0.15	-1.9
Refractive Index		1.85	1.80	1.80	1.56	2.20	1.68	2.16

Table 4: Parameters of various experiments using scintillating crystals.

Experiment		KTeV	BaBar	BELLE	CMS
Laboratory		FNAL	SLAC	KEK	CERN
Crystal Type		CsI	CsI(Tl)	CsI(Tl)	PbWO ₄
B-Field	T	-	1.5	1.0	4.0
Inner Radius	m	-	1.0	1.25	1.3
No. of crystals		3,300	6,580	8,800	76,150
Crystal Depth	X ₀	27	16-17.5	16.2	26
Crystal Volume	m ³	2	5.9	9.5	11
Light Output	p.e./MeV	40	5,000	5,000	4
Photosensor		PMT	Si PD	Si PD	APD*
Gain of photosensor		4,000	1	1	50
Noise / channel	MeV	Small	0.15	0.2	30
Dynamic Range		10 ⁴	10 ⁴	10 ⁴	10 ⁵

* APD: Si avalanche photodiode

11.1 Radiation Damage in Crystals

All crystals suffer from radiation damage at some level. It is rare that irradiation affects the scintillation mechanism itself. However formation of colour centres takes place leading to absorption bands. A colour centre is a crystal defect that absorbs visible light. A high concentration of blue light colour centres makes crystals yellowish. The simplest colour centre is an F-centre where an electron is captured in an anion vacancy. The consequence of colour centre production is a decrease in the light attenuation length leading to a decrease in the amount of light incident on the photosensor. This is illustrated in Figure 27 for various samples of PbWO₄ crystals grown under differing conditions. The crystals were irradiated using γ s, incident at the front of the crystal, from a ⁶⁰Co source.

Extensive R&D has been carried out over the last 5 years by CMS in order to improve the radiation hardness of PbWO₄ crystals [29]. Generally the strategy has been to decrease the concentration of defects that lead to colour centre production by optimizing the stoichiometry (the concentration of PbO and WO₃ in the melt) and annealing after the growth of the crystal. The remaining defects are compensated by specific doping, e.g. by pentavalent elements on the W site and trivalent on the Pb site, and by improving the purity of the raw materials. The levels of improvement can be seen from Fig 69. The most recent crystals of lead tungstate have shown very good resistance to irradiation. This is illustrated in Fig 70. The loss of collected light, for crystals doped with both niobium and yttrium, show a decrease in the collected light of less than 2% at saturation. The effect of irradiation can also be dose-rate dependent

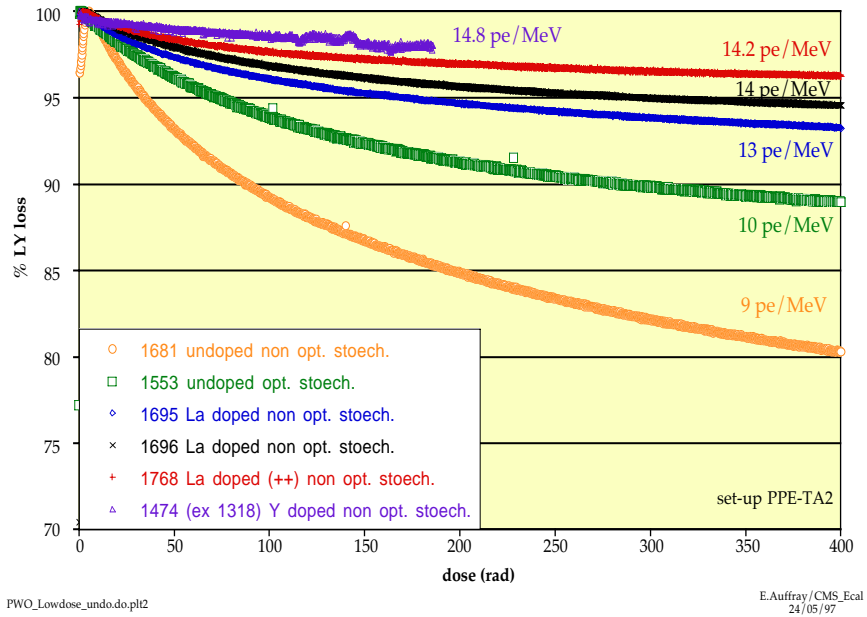


Figure 69: The loss in the collected light as a function of dose (delivered at ≈ 0.15 Gy/hr) for crystals grown under various conditions.

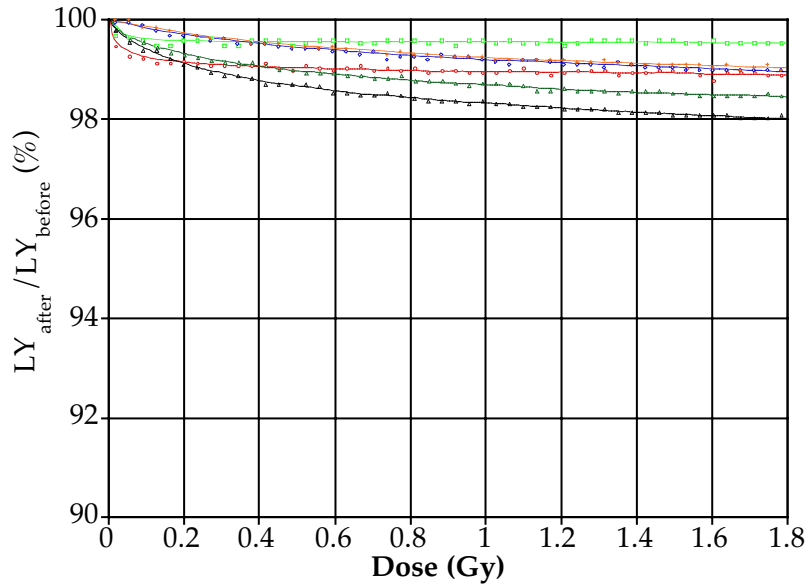


Figure 70: The loss in the collected light as a function of dose (delivered at ≈ 0.15 Gy/hr) for recent PbWO_4 crystals doped with Niobium and Yttrium.

The radiation dose expected at the shower maximum for the lead tungstate calorimeter of CMS, over the first ten years of LHC operation, is below 4,000 Gy in the barrel region ($|\eta| < 1.5$), $\approx 70,000$ Gy at $|\eta| \approx 2.5$ rising to 200,000 Gy at $|\eta| \approx 3.0$. Furthermore the expected dose rate at design luminosity, and shower maximum, is below 0.3 Gy/h in the barrel region, ≈ 6 Gy/h at $|\eta| \approx 2.5$ rising to 15 Gy/h at $|\eta| \approx 3.0$.

11.2 Performance of CMS Lead Tungstate Crystals

Several matrices of improving quality have been tested in electron beams over the last few years. Radiation damage leads to a decrease in the attenuation length and hence in the collected light. As the efficiency of the scintillation mechanism is not affected by irradiation the energy resolution will not be affected as long as the attenuation length does not fall below ≈ 2 -3 times the length of the crystal. The small loss of light can be corrected by regularly measuring the response to a known amount of light injected into crystals. This has been demonstrated in beam tests [31].

Results from a recently tested prototype are shown in Fig 71. The distribution of the sum of energy in 9 crystals for electron of an energy of 280 GeV is shown. An excellent energy resolution is measured without significant tails. The measured energy resolution is also shown. The stochastic term is expected to be $< 3\%$ in the final calorimeter since the surface area of the photosensor will be doubled.

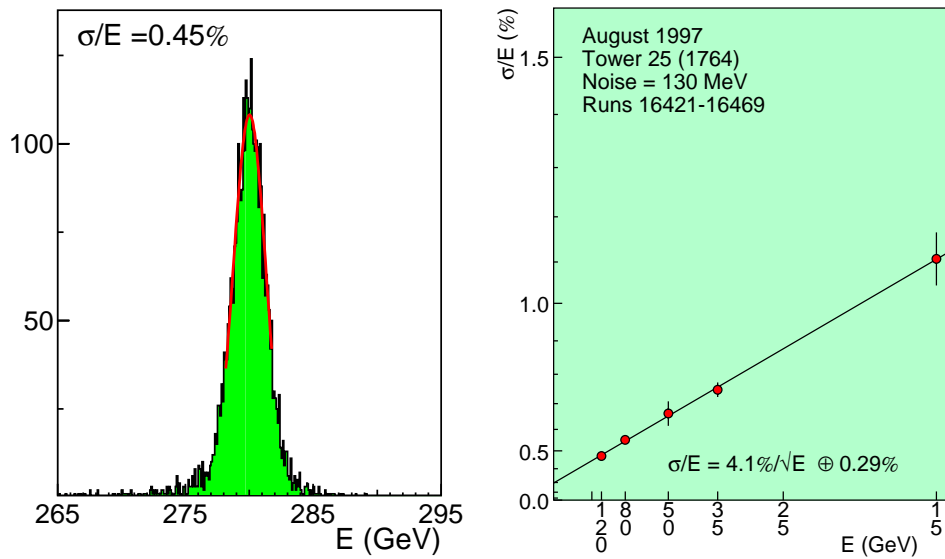


Figure 71: a) The distribution of the sum of energy in 9 crystals for an electron of an energy of 280 GeV, b) the measured energy resolution

11.3 Photosensors

11.3.1 Photomultipliers

The contribution to the energy resolution from the process of conversion of light to photoelectrons can be significant. For example, in a lead glass calorimeter about 10,000 Cerenkov photons/GeV impinge on the photomultiplier. The conversion leads to about 1000 photoelectrons/GeV and hence the contribution to the stochastic term will be

$$\left(\frac{\sigma}{E}\right)_{pe} = \frac{\sqrt{1000}}{1000} \approx 3.2\%$$

The maximum number of independent e^\pm particles, given that the Cerenkov threshold is 0.7 MeV, is $1000/0.7$ per GeV i.e. $n = 1400 e^\pm$. This leads to an additional contribution to the energy resolution i.e. $(\sigma/E)_n = (\sqrt{1400})/1400 \approx 2.7\%$. The observed resolution then becomes

$$\frac{\sigma}{E} = \sqrt{\left(\frac{\sigma}{E}\right)_n^2 + \left(\frac{\sigma}{E}\right)_{pe}^2} \approx 4.5\%$$

An energy resolution of $\sigma/E \sim 5\% / \sqrt{E}$ for e.m. showers has been measured in a large lead glass array [32].

11.3.2 Silicon Avalanche Photodiodes

The light output from PbWO_4 crystals is low. These crystals are deployed by CMS in a 4T transverse magnetic field and the use of photomultipliers is excluded. Unity gain Si photodiodes cannot be used since even the small rear shower leakage from $25 X_0$ deep crystals considerably degrades the energy resolution. This is due to the fact that the photodiode response to ionising radiation is significant compared with the signal due to scintillation light. Hence CMS use Si avalanche photodiodes (APDs) with a gain of about 50. The particularity of these novel devices, over and above photomultipliers, is the noisy amplification process. The working principle of these devices is shown in Fig 72.

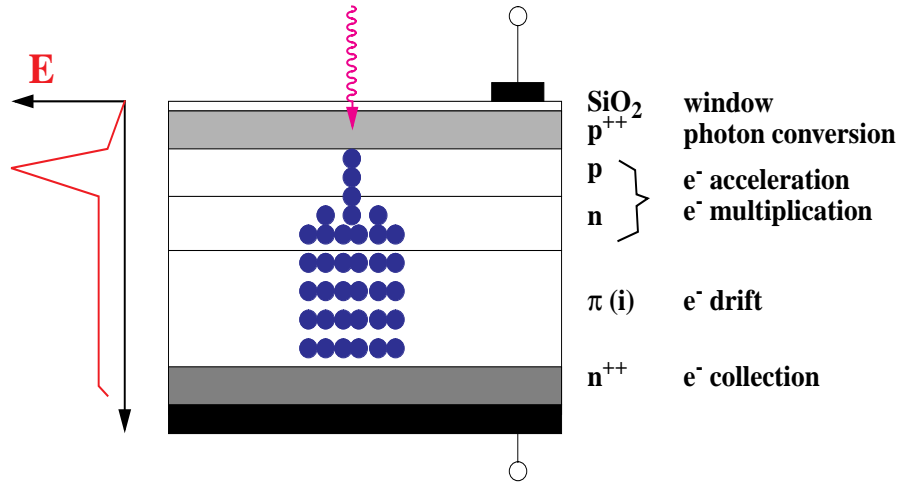


Figure 72: The working principle of a Si avalanche photodiode.

Consider a crystal with a light yield of N_γ photons/MeV. $N_\gamma E$ photons hit the APD for an energy deposit E . Assuming a quantum efficiency Q (which can easily be $\approx 85\%$ for APDs),

No. of photoelectrons is $N_{pe} = N_\gamma E Q$

Then the photostatistics fluctuation is $\pm \sqrt{N_{pe}}$

If there is no fluctuation in the gain process then the no. electrons transferred to the amplifier is (M =gain) $M N_{pe} \pm M \sqrt{N_{pe}}$

BUT if the multiplication process is noisy and the gain itself has a fluctuation, σ_M , then the no. of electrons is $M N_{pe} \pm \sqrt{M^2 + \sigma_M^2} \sqrt{N_{pe}}$

Hence the photostatistics contribution to the energy resolution becomes

$$\frac{\sigma_{pe}(E)}{E} = \frac{1}{\sqrt{N_\gamma E Q}} \sqrt{\frac{M^2 + \sigma_M^2}{M^2}} = \frac{1}{\sqrt{N_\gamma E Q}} \sqrt{F}$$

where F is called the 'excess noise factor' and quantifies the induced degradation in the energy

resolution due to fluctuations in the amplification process. Typically for APDs $F \approx 2$ and for photomultipliers $F \approx 1.2$. Some properties of APDs, from two manufactures, are listed in Table 5.

Table 5: Some properties of APDs

Parameter	Hamamatsu	EG&G
Active Area	25 mm ²	25 mm ²
Quantum Efficiency at 450nm	80%	75%
Capacitance	100 pF	25 pF
Excess Noise Factor, F	2.0	2.3
Operating Bias Voltage	400-420 V	350-450 V
dM/dV x 1/M at M=50	5%	0.6%
dM/dT x 1/M at M=50	-2.3%	-2.7%

11.4 System Aspects

A real calorimeter is a system comprising active media, electronics chain and mechanical structure, all enclosed in an environment that must be kept stable. Hence many factors have to be considered in order to maintain the resolution achieved in beam tests. For example, in the case of the CMS ECAL, the temperature of the crystals has to be maintained to within 0.1% since both the crystal and the photosensor each have a temperature dependence of the output signal of $d(\text{Signal})/dT \approx -2\%/^{\circ}\text{C}$. This requires a powerful cooling system and a hermetic environmental shield. To maintain uniformity of response across crystals the mechanical structure has to be thin and preferably made of low-Z material. No load from one crystal should be transferred to its neighbours. A 300 μm glass fibre alveolar structure has been chosen by CMS. The electronics system has to provide a stable response, deliver high resolution digitization (12-bits) and a large dynamic range (≈ 16 -bits) whilst preserving a low electronics noise per channel (< 40 MeV/channel). Furthermore, the on-detector electronics must be radiation hard and have as low a power consumption as possible.

More information on the systems aspects of calorimeters can be found in the ATLAS [10] and CMS [11] Technical Design Reports.

12. CALORIMETRY USING NOBLE LIQUIDS

Calorimeters using liquid filled ionization chambers as detection elements have several important advantages. The absence of internal amplification of charge results in a stable calibration over long periods of time provided that the purity of the liquid is sufficient. The number of ion pairs created is large and hence the energy resolution is not limited by primary signal generating processes. The considerable flexibility in the size and the shape of the charge collecting electrodes allows high granularity both longitudinally and laterally.

The desirable properties of liquids used in ionization chambers include:

- a high free electron or ion yield leading to a large collected charge,
- a high drift velocity and hence a rapid charge collection,
- a high degree of purity. The presence of electron scavenging impurities leads to the reduction of electron lifetime and consequently a reduction in the collected charge.

The properties of noble liquids are given in Table 6.

12.1 Charge Collection in Ionisation Chambers

Ionisation chambers are essentially a pair of parallel conducting plates separated by a few mm and with a potential difference in an insulating liquid (e.g. liquid argon).

Consider what happens when a single ion-pair is created at a distance $(d-x)$ from the +ve electrode (Fig. 73). The electron drifts towards the +ve electrode and induces a charge

$$Q = - e \frac{(d-x)}{d}$$

where d is the width of the gap. Assuming that the electron drifts with a velocity v , and the time to cross the full gap is v_d , then the induced current is

$$i(t) = \frac{dQ}{dt} = - e \frac{v}{d} = - \frac{e}{t_d}$$

The contribution from the drifting ions can be neglected as their drift velocity is about three orders of magnitude smaller than that of electrons.

Table 6: Properties of noble liquids.

		LAr	LKr	LXe
Density	g/cm ³	1.39	2.45	3.06
Radiation Length	cm	14.3	4.76	2.77
Moliere Radius	cm	7.3	4.7	4.1
Fano Factor		0.11	0.06	0.05
Scintillation Properties				
Photons/MeV		-	1.9 10 ⁴	2.6.10 ⁴
Decay Const. Fast	ns	6.5	2	2
Slow	ns	1100	85	22
% light in fast component		8	1	77
λ peak nm		130	150	175
Refractive Index @ 170nm		1.29	1.41	1.60
Ionization Properties				
W value	eV	23.3	20.5	15.6
Drift vel (10kV/cm)	cm/ μ s	0.5	0.5	0.3
Dielectric Constant		1.51	1.66	1.95
Temperature at triple point	K	84	116	161

Now consider the case where a charged particle traverses the gap (Figure 31b). Suppose N ion-pairs are produced and are uniformly distributed across the gap. The fraction of electrons still moving at a time t after traversal is $(t_d-t)/t_d$ for $t_d < t$. Therefore

$$i(t) = - Q_0 \frac{v}{d} \left(1 - \frac{t}{t_d}\right)$$

where $Q_0 = Ne$ and the current is at its maximum at time $t = 0$ and disappears once all the charges have crossed the drift gap. This time is about 400 ns for a 2 mm LAr gap. Hence

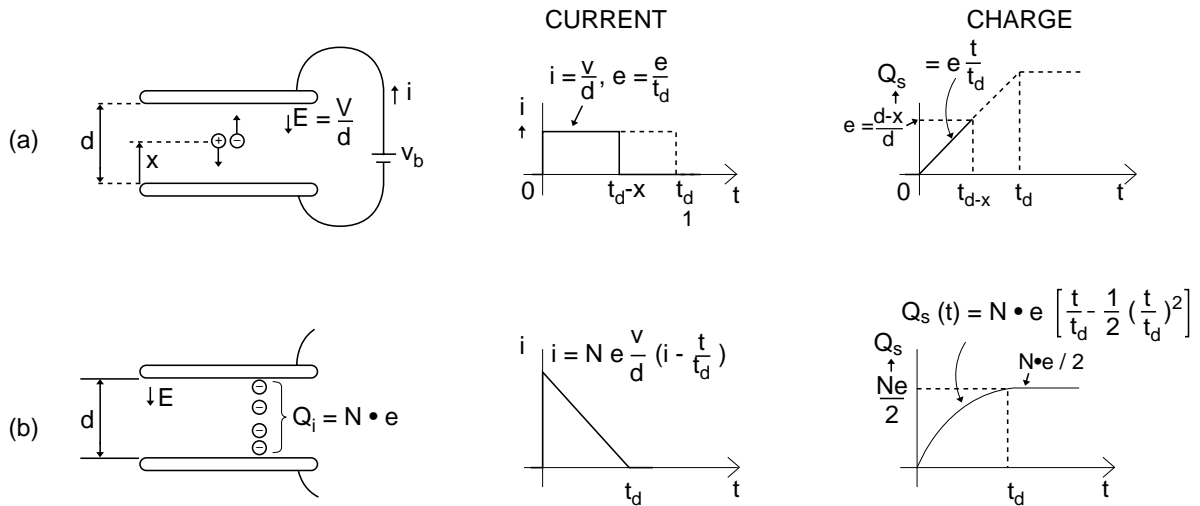
$$q(t) = \int_0^t i(t) dt = -Q_0 \left(\frac{t}{t_d} - \frac{t^2}{2t_d^2} \right) \text{ for } t < t_d$$

The total collected charge (for $t > t_d$) is

$$Q_c = \frac{Q_0}{2}$$

The factor two is due to uniform distribution of ionisation. During drift the electrons can be trapped by impurities. Then the induced current will be reduced. In fact if the electron lifetime is τ

$$i(t) = \frac{Q_0}{t_d} \left(1 - \frac{t}{t_d} \right) e^{-t/\tau} \text{ for } t < t_d$$

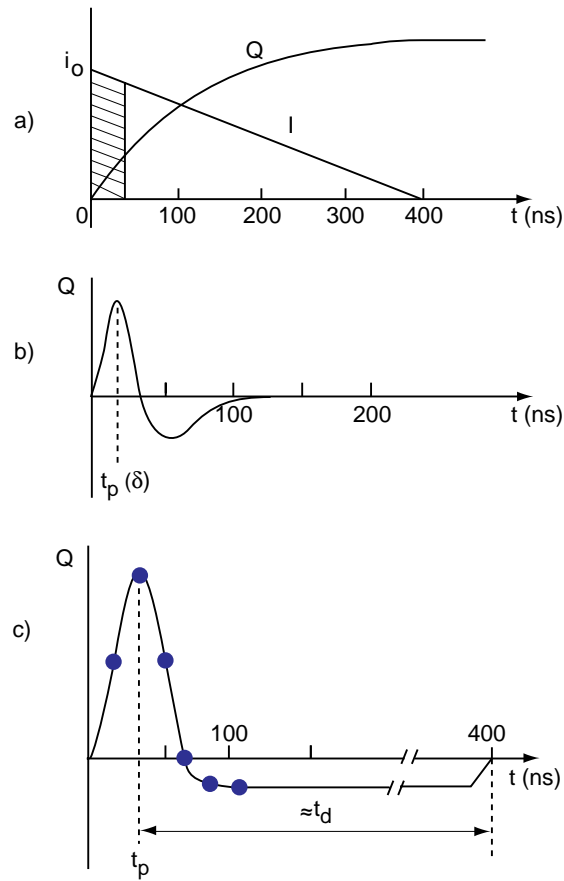


J.V.274

Figure 73: The current and charge for a) a single e-ion pair, b) uniformly distributed e-ion pairs.

12.2 Signal Shapes

As discussed above, for a long electron ‘lifetime’ the induced current has a triangular shape with a duration equal to the electron drift time t_d (Fig. 74a). The total collected charge is also shown. It is clear that a device based on full charge collection will be slow, and hence not suitable for use at the LHC. However the energy information is contained in the initial current i_0 . The information can be extracted and high rate operation made possible by clipping the signal with fast bipolar shaping (Fig. 74b). If the system impulse response has zero integrated area then pileup does not produce a baseline shift. For a peaking time, t_p that is much faster than drift time i.e. $t_p \ll t_d$, the output response becomes the first derivative of the current pulse (Fig. 74c). The height of the output pulse is proportional to the initial current. However, with respect to full charge collection, the energy equivalent of the electronics noise will increase as this scales with $1/\sqrt{\tau}$, where $\tau (=RC)$ is the shaper time constant. At high luminosities, pileup also influences the choice of the value of τ . Pileup scales as $\sqrt{\tau}$. As an example, the optimized value for τ gives $t_p \approx 40$ ns for the ATLAS ‘‘accordion’’ e.m. calorimeter..



JV_204

Figure 74: a) Induced current and integrated charge, b) bipolar shaping function and c) the shape of the output pulse, all as a function of time.

12.3 Examples of Noble Liquid Calorimeters

Conventionally ionization chambers are oriented perpendicularly to the incident particles. However in such a geometry it is difficult to

- realize fine lateral segmentation with small size towers, which in addition need to be projective in collider experiments,
- implement longitudinal sampling,

without introducing insensitive regions, a large number of penetrating interconnections, and long cables which necessarily introduce electronics noise and lead to significant charge transfer time. To overcome these shortcomings a novel absorber-electrode configuration, known as the 'accordion' (Fig. 75, [33]), has been introduced, in which the particles traverse the chambers at angles around 45° .

In a variant, the NA48 [34] experiment has chosen an arrangement of electrodes that is almost parallel to the incident particles. With such structures the electrodes can easily be grouped into towers at the front or at the rear of the calorimeters. In ATLAS the absorber is made of lead plates, clad with thin stainless steel sheets for structural stiffness and corrugated to the shape shown in Fig. 75. Details of the sampling structure are also shown. The read-out electrodes are made out of copper clad kapton flexible foil and kept apart from the lead plates by a honeycomb structure.

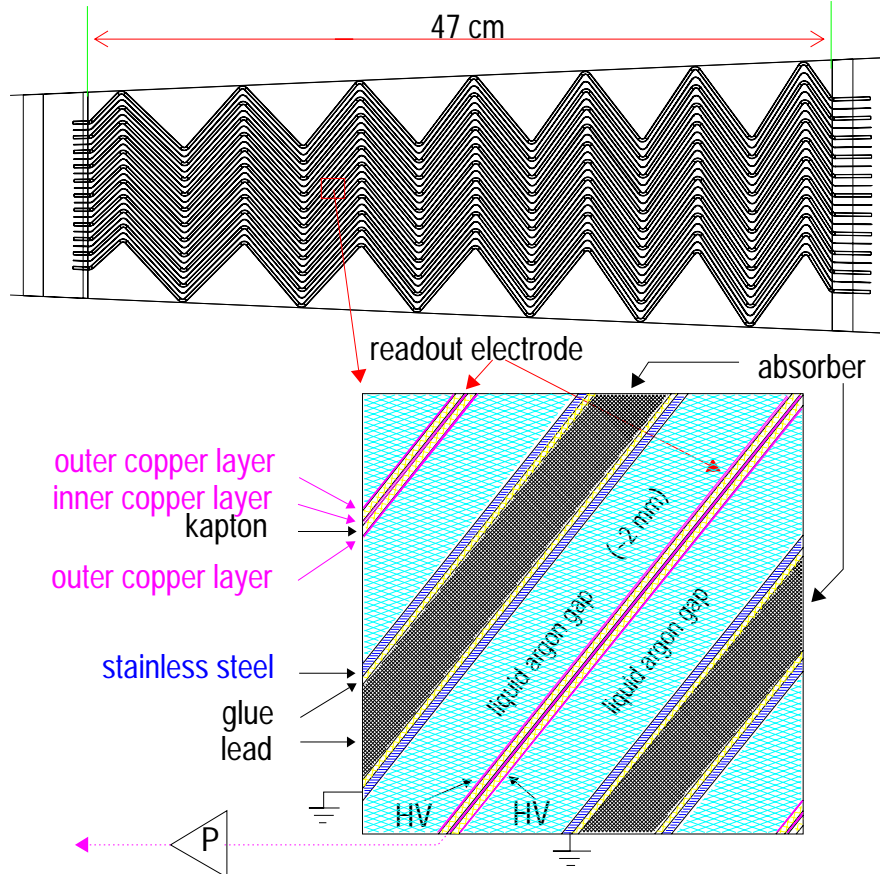


Figure 75: Top) the “accordion” structure of absorber plates of the ATLAS ECAL, below) details of the electrode structure.

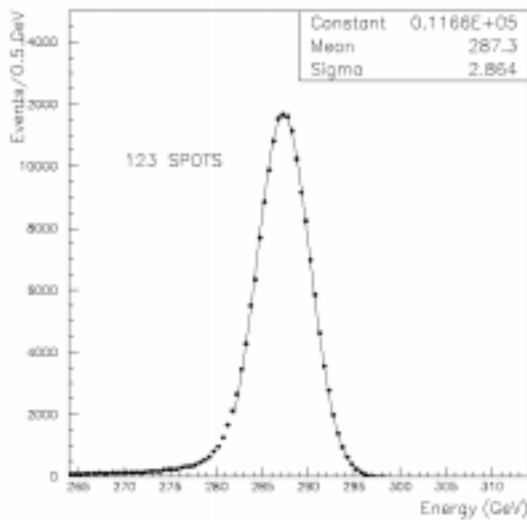


Figure 76: The distribution of the reconstructed energy for 300 GeV electrons in the ATLAS ECAL.

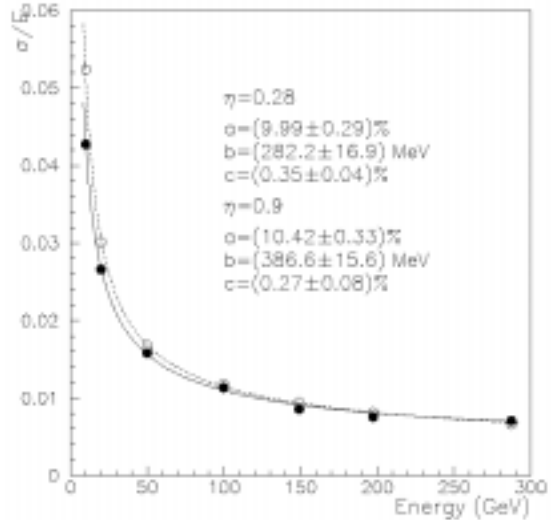


Figure 77: The fractional energy resolution for the ATLAS barrel prototype ECAL.

The results from a beam test of a large ATLAS prototype are shown in Figs. 76 and 77. The electron shower is reconstructed using a region of 3x3 cells each of a size of $\approx 3.7 \text{ cm} \times 3.7 \text{ cm}$. The distribution of reconstructed energy for 300 GeV electrons, over a large area, is shown in

Fig. 76. The fractional energy resolution is shown in Fig. 77 and can be parameterised as

$$\frac{\Delta E}{E} \approx \frac{10\%}{\sqrt{E}} \oplus \frac{0.28_{\text{GeV}}}{E} \oplus 0.35\%$$

where E is in GeV. The response of more than 150 cells over a large area has also been measured. The cell-to-cell non-uniformity is measured to be $\approx 0.58\%$. The major contributions come from mechanics (residual ϕ -modulation, gap non-uniformity, variation of absorber thickness) and calibration (amplitude accuracy). The large flux of isolated electrons from W or Z decays will be used to establish cell-to-cell intercalibration.

13. COMBINED E.M. AND HADRONIC CALORIMETRY

The LHC pp-experiments have put more emphasis on high precision e.m. calorimetry. This is not compatible with perfect compensation. For example the electromagnetic energy resolution of the compensating ZEUS U-calorimeter is modest. The e.m. (σ_E) and hadronic (σ_h) resolutions are given by

$$\frac{\sigma_E}{E} = \frac{17\%}{E} \quad \text{and} \quad \frac{\sigma_h}{E} = \frac{35\%}{E}$$

Nevertheless it is very important to ensure:

- a Gaussian hadronic energy response function (a moderate energy resolution is acceptable),
- hermiticity
- linearity of response, especially for jets.

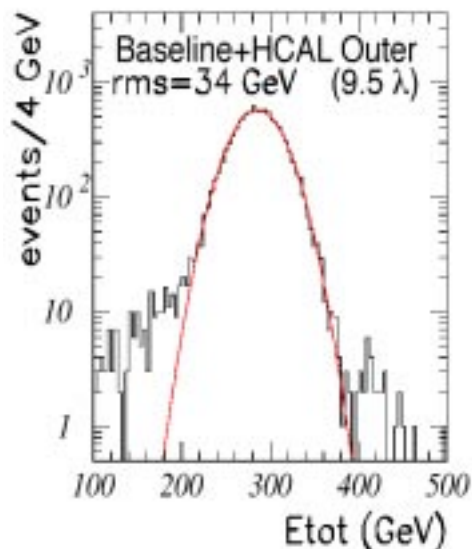


Figure 78: Distribution of reconstructed energy of 300 GeV pions [8, HCAL TDR].

As an example in CMS this is done by introducing multiple longitudinal samplings. Reading out separately the first scintillator plate, placed behind the e.m. calorimeter, allows a distinction to be made between the cases where an e.m. shower has developed in the crystals (little signal from the first scintillator) and the ones where a hadronic shower has started (signal from the first scintillator). The energy observed in the first scintillator therefore allows a correction to be made. In fact the correction can be somewhat ‘hard-wired’ by choosing an appropriate thickness for the scintillator. The longitudinal leakage can also be up-weighted by increasing the thickness of the

last scintillator. The measured energy distribution for 300 GeV pions in the CMS baseline is shown in Fig. 78. The tails are kept below a few percent.

The test beam results of the combined calorimetry of ATLAS (LAr ECAL and Fe/Scintillator HCAL) are shown in Fig. 79. The data are compared with results from two simulation codes namely FLUKA and GCALOR. Use is made of three energy-independent corrections for the:

- intercalibration between the e.m. and hadronic calorimeter
- energy lost in the cryostat wall separating the two calorimeters
- non-compensating behaviour of the e.m. calorimeter. A quadratic correction is made.

The above procedure minimizes the fractional energy resolution but results in a systematic underestimation of the reconstructed energy: by 20% at 30 GeV and decreasing to $\approx 10\%$ at 300 GeV. Other weighting methods, which have the effect of simultaneously minimizing the non-linearity and the energy resolution can also be employed.

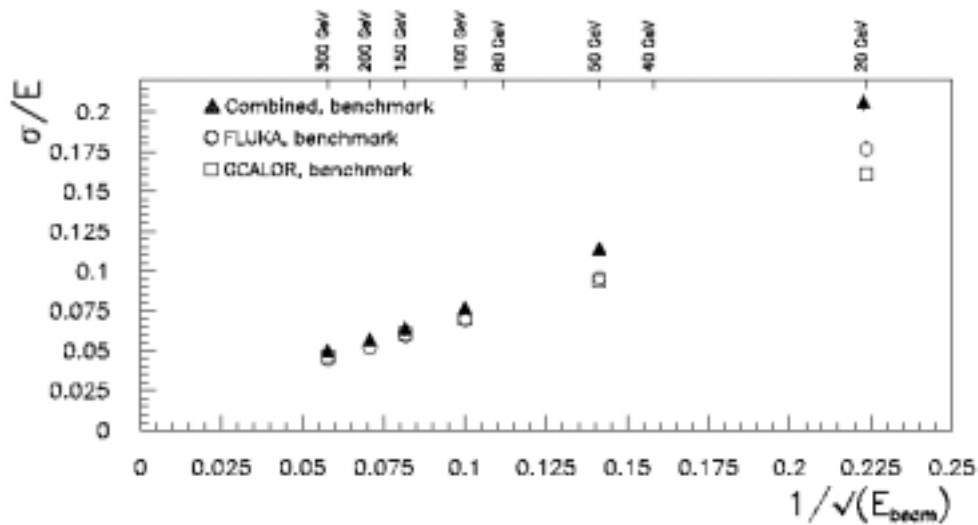


Figure 79: The energy resolution for pions compared with FLUKA and GCALOR simulation codes.

The hadronic cascade simulation codes such as FLUKA, GHEISHA and GCALOR have improved substantially and can now be used with some confidence in the design of hadron calorimeters.

14. TRIGGER AND DATA ACQUISITION SYSTEM

The bunch crossing rate at the LHC is 40 MHz. At high luminosity about 1 billion pairs of protons are interacting every second. The role of the trigger and data acquisition system is to look at (almost) all the bunch crossings, select about one hundred of these containing the most interesting events, collect all the detector information corresponding to these and record on permanent storage for offline analysis. This is a daunting task because the selection process:

- must be highly efficient. Since only data from about 100 crossings can be recorded the vast majority of the events have to be rejected. However none of the few expected rare events should be missed.
- should not introduce any bias.
- should cause as little deadtime as possible.
- must use data from the same crossing for all sub-detectors. This requires synchronisation of millions of channels.

- needs an information super-highway as the 20 or so interactions every 25 ns lead to the generation of 40,000 Gbits/s. The data flow has to be reduced as quickly as possible by high selectivity.

- is carried out in real time i.e. one cannot go back and recover lost events. It is essential to monitor the selection process.

A typical trigger and data acquisition system consists of four parts : the detector electronics, the calorimeter and muon first level trigger processors, the readout network and an on-line event filter system. As an example the functional view of the CMS system is shown in Fig.80

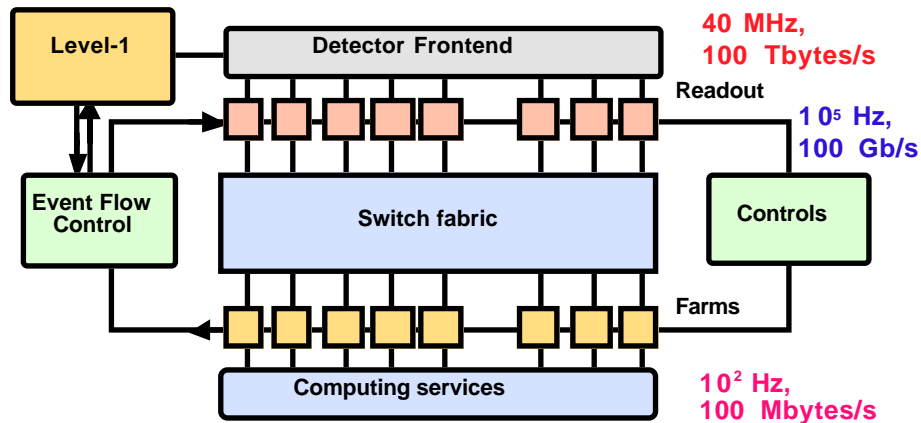


Figure 80: The functional view of the CMS trigger and data acquisition system.

The Level-1 Trigger System is required to reduce the bunch-crossing rate of 40 MHz to an event rate of 100 kHz. Upon receipt of a Level-1 trigger the data from the pipelines are first transferred to ‘derandomizing’ memories that can accept the very high instantaneous input rate (the Level-1 can accept several events within the space of \approx ten crossings even though the average rate is much lower). These memories are emptied into readout buffers: usually many individual channels are multiplexed over a single readout link. After further signal processing (e.g. digitisation, deconvolution) zero suppression and/or data compression takes place before the reduced amount of data are placed in dual-port memories for access by the DAQ system. Each physics event (\approx 1 Mbytes large) is contained in about 500 front-end *Readout* buffers. To further analyse the event it is necessary to transfer the data from the 500 Readout units to a single processor running the appropriate physics selection algorithm. The input rate of 100 kHz is thus reduced to the 100 Hz of sustainable physics. The ‘event building’ is performed using a data switch, somewhat similar to a telephone exchange; in fact use will certainly be made of switching technologies from the telecommunications industry. The most important elements, and also the most difficult ones to develop, are the front-end buffers, the switch that will connect these memories to the processor farm and the physics selection selection algorithms.

14.1 Level-1 Trigger

Since the detector data are not all promptly available and the selection process is highly complex, it is carried out by successive approximations called trigger levels.

The search for new physics involves the study of hard interactions. Hence the first trigger step (Level-1) looks for any one or a combination of the following entities: high transverse momentum muons, high transverse energy photons, electrons, or jets, significant missing E_t (to find neutrinos). Track stubs in the muon system or energy deposits in the calorimeters are used to create the so-called trigger objects: isolated e.m. clusters, muons, jets, E_t^{miss} etc. The selection is

based on e.m. and/or hadronic clusters and/or muons with transverse energy and momentum above certain pre-loaded thresholds in trigger processors.

The time required to make the Level-1 decision is between 2 to 3 μs . Most of the time is taken by propagation delays on cables between the detector and the underground counting room where the trigger logic is housed. There is not much time to combine information from sub-detectors and only elementary operations with elementary conditions are possible. Reduced granularity (e.g. information from groups of 25 crystals are combined to form one trigger-tower, of typical size $\Delta\eta \times \Delta\phi \approx 0.1 \times 0.1$, in the case of CMS ECAL) and reduced resolution (e.g. 8-bits instead of full 12-bit information is used for energy in the CMS ECAL trigger towers) data are used to form trigger objects.

An example from ATLAS of how an isolated e.m. calorimeter is selected is shown in Fig. 81. There are some 4000 ECAL and geometrically matching 4000 HCAL trigger towers each giving an 8-bit value every 25 ns.

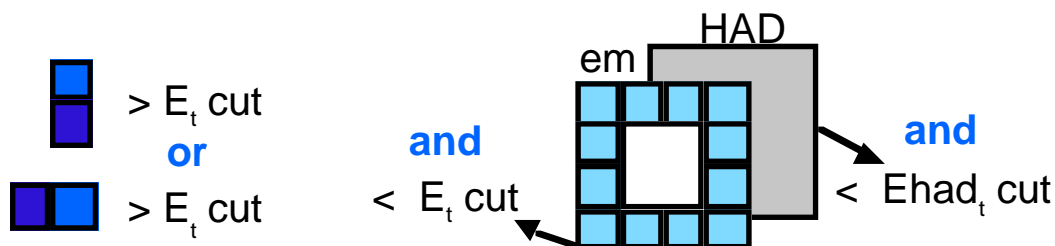


Figure 81: Selection of isolated e.m. clusters at Level-1 Trigger in ATLAS

The Level-1 selection proceeds as follows: the energy in a ‘hot’ trigger tower is combined with that from the hottest one in either η or ϕ (Fig. 81) the transverse energy of the sum should be greater than some E_t^{cut} , an isolation condition is applied. For an isolated cluster the transverse energy in the 12 towers surrounding the central 2x2 has to be smaller than E_t^{em} . Furthermore the transverse energy leaking into the HCAL (sum energy in the 16 HCAL towers behind) for an e.m. shower has to be smaller than E_t^{had} .

The above algorithm is applied for each of the 4000 window positions representing a massive computing task. Pipelined and parallel processing is employed. Pipelined processing means that the logic is organised in a chain of operations to be performed one after the other for each crossing. Each processing element in the chain performs its function in 25 ns and passes its result to the next element in the chain. Data corresponding to successive bunch crossings follow each other down the processing ‘pipe’. Parallel processing means that many processing elements act in parallel, for example performing the same operations on different data.

The above algorithms can be extended to triggers on taus or jets. For a τ -trigger, the vertical and horizontal sum transverse energy of the two (2x1) or four (2x2) trigger towers in both ECAL and HCAL should be greater than some cut E_t^{cut} . The isolation is applied only in the ECAL as above. For jet triggers the transverse energy is summed in 4x4 trigger towers in both the ECAL and the HCAL. A sliding window can be employed centred on blocks of 2x2 towers.

For muon triggering ‘roads’ are defined from one station to the next. The width of the road depends on the desired p_t threshold. The calculation allows for magnetic deflection and multiple scattering. An example, from CMS, is shown in Fig.82.

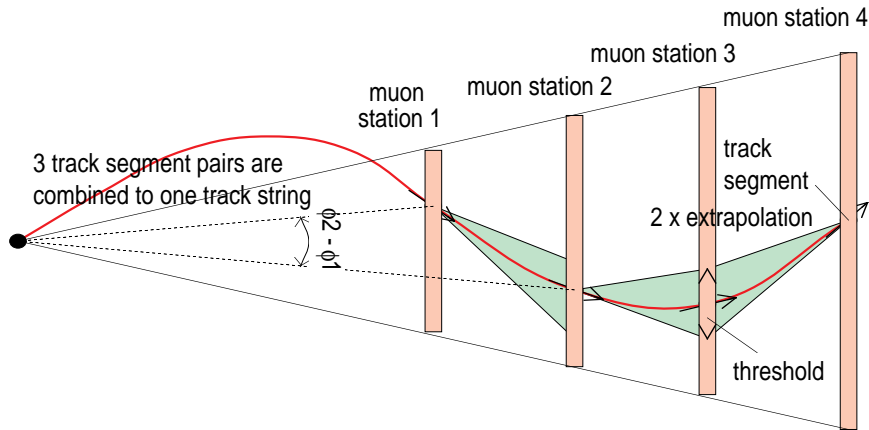


Figure 82: Schematic of Muon Level-1 trigger in CMS using 'roads'.

Each of the barrel stations consist of two sets of 4 planes of drift tubes measuring the r - ϕ coordinate. The two sets are separated by about 20 cm and hence a 'primitive' giving the track direction can be created. This is used to project to the next station and if a consistent primitive is found there the process is continued. This allows muon finding and a yes or no answer for the trigger.

The trigger rates for e.m clusters for ATLAS and muons for CMS are illustrated in Figs. 83 and 84. The efficiency curves are also shown. Clearly for the lowest possible rate the turn-on in the efficiency curve should be as steep as possible (ideally a step function).

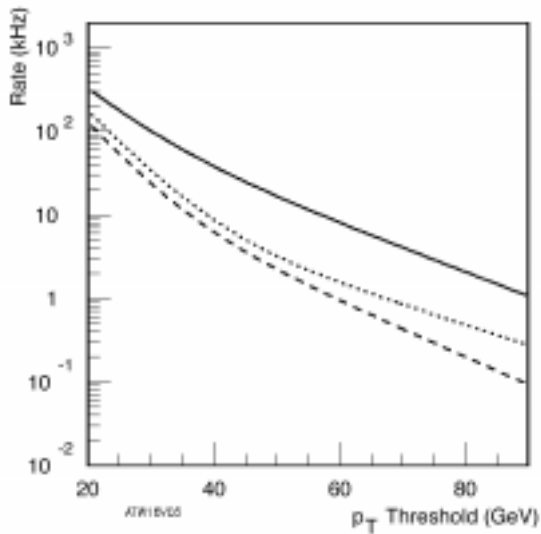


Figure 83: Inclusive electron trigger rate at high luminosity ($10^{34} \text{ cm}^{-2} \text{ s}^{-1}$), without isolation (solid), requiring only hadronic isolation (dotted) and requiring both electromagnetic and hadronic isolation (dashed).

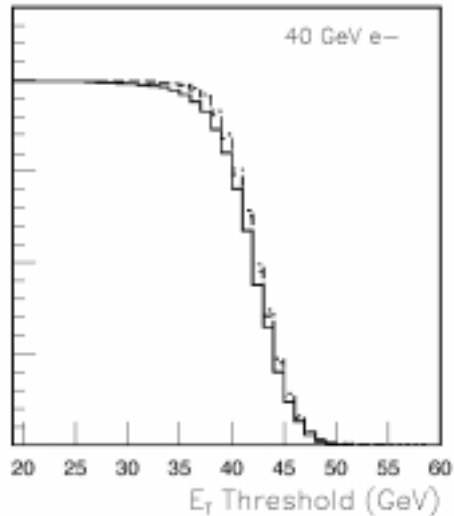


Figure 84: Trigger efficiency curve for 40 GeV E_T electrons at high luminosity ($10^{34} \text{ cm}^{-2} \text{ s}^{-1}$).

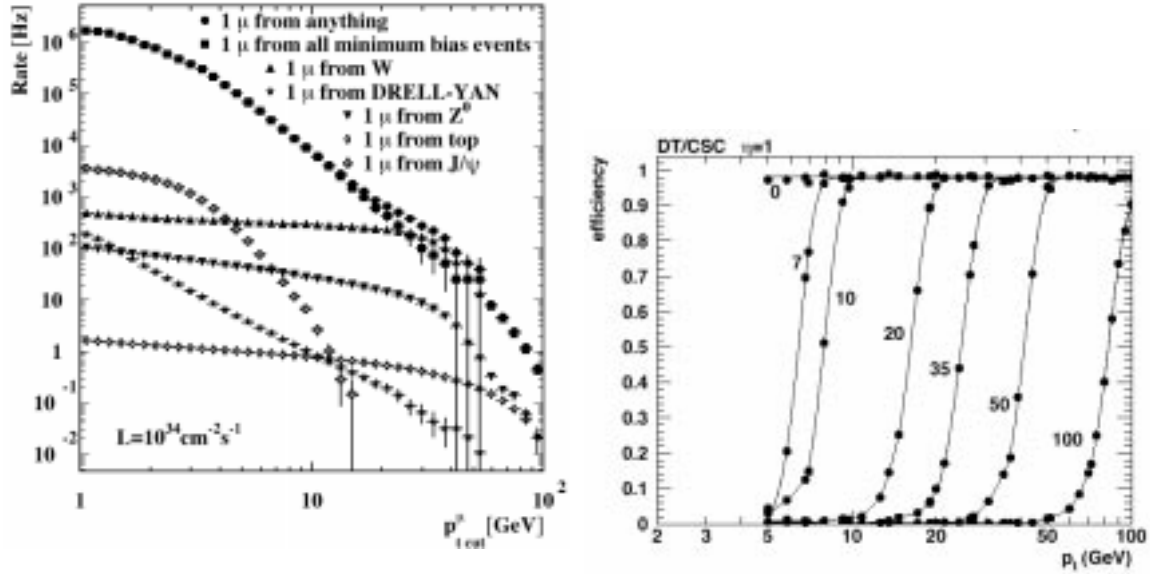


Figure 84:

For events within the geometric acceptance of the detector the trigger ‘cocktail’ and the rates at high luminosity ($10^{34} \text{ cm}^{-2} \text{ s}^{-1}$) for CMS are detailed in Table. 7. The physics efficiency (for events within the geometric acceptance of the detector) using these cuts for some example channels is as follows: $H(80 \text{ GeV}) \rightarrow \gamma\gamma - \approx 99\%$, $H(150 \text{ GeV}) \rightarrow 4l - \approx 100\%$, $pp \rightarrow t\bar{t}b\bar{b} \rightarrow eX - \approx 90\%$, $\Sigma \text{SUSY} - \approx 85\%$. The cumulative rate of 30 kHz is predicted. However a margin for error is taken and both ATLAS and CMS are designing their systems to handle at least 100 kHz of input rate.

Table 7: Trigger rates in CMS running at high luminosity for 90% efficiency of selection

Type Calo.	E_t^{cut} GeV	Individ. kHz	Increm, kHz	Type Muon	E_t^{cut} GeV	Individ. kHz	Increm. kHz
Sum E_t	400	0.3	0.3	1μ	20	7.8	7.8
E_t^{miss}	200		0.9	2μ	4	1.6	9.2
1 e.m.	33		5.3	$1\mu+1e.m$	4/8	5.5	14.4
2 e.m.	20		1.3				
1 jet	140		1.0	$1\mu+1 \text{ jet}$	4/40?	0.3	14.4
Multijets	various		3.0	$1m+ E_t^{\text{miss}}$	4/60?	1.0	15.3
1 em+1jet	14/50		0.3				
Cumul.			12.1	Cumul.		≈ 15	

Numbers need checking

14.2 Higher Level Triggers and Data Acquisition

The output rate from the Level-1 trigger has to be reduced to 100 Hz by using more complex algorithms. In CMS all this will be carried out in a processing farm. The farm will consist of about 500 computers with the capability of 1000Gips (Giga instructions per second). The aim is to initially bring to the farm only the full granularity and full-precision calorimeter and/or muon system data. The Level-1 trigger will point to the region of interest (ROI) for further analysis. A

factor of 5-10 reduction in rate is to be achieved by refining the energy or momentum measurement and applying a sharper cut. The isolation condition is also refined. The tracker data corresponding to the ROI may then be pulled into the processor through the switch. For example matching e.m. clusters or track segments in the muon system to tracks in the ROI, both in space and in energy/momentum, will enable the rate to be further reduced. At each level of refinement more data are brought into the processor but for fewer and fewer events. The final step will use the full event data and almost full event reconstruction and physics analysis will be carried out. In this way the bandwidth needed in the switch can be minimized. Nevertheless a switch network of about 500 Gbits/s is required. It is estimated that the data rate that will be handled by the LHC experiment event builders is equivalent to the data rate exchanged by World Telecom today (1998).

15. CONCLUSION

Much R&D has been carried out during the last 8 years to develop detectors that could cope with the harsh conditions anticipated in the pp LHC experiments. These detectors are not just bigger versions of the current detectors but are substantially different, innovative and at the frontier of technology. Improvements in techniques used in particle detection have always been essential to explore uncharted territory. The ATLAS and CMS detectors should be capable of discovering whatever Nature has in store at the TeV energy scale.

ACKNOWLEDGEMENTS

I would like to thank Nick Ellis for the invitation to give these lectures. I would also like to sincerely acknowledge the unknowing help from many colleagues (S. Cittolin, N. Ellis, D. Green, G. Hall, C. Fabjan, D. Fournier, C. Joram, C. Seez, P. Sphicas, to name a few). I have liberally borrowed from their presentations and write-ups in various schools and conferences. I would like to thank Guy Martin for drawing many plots in the lectures and this write-up.

REFERENCES

- [1] Techniques for Nuclear and Particle Physics Experiments, W. R. Leo, Springer, 1994.
- [2] Single Particle Detection and Measurement, R. S. Gilmore, Taylor and Francis, 1992.
- [3] Physics of Particle Detectors, D. Green, Cambridge Univ. Press, to be published.
- [4] Rev. of Particle Physics, C. Caso et al., Euro Phys. J. C3(1998)1, <http://pdg.lbl.gov/>
- [5] D. Fournier and L. Serin, Experimental Techniques, 1995 European School of HEP, CERN 96-04, 1996.
- [6] N. Ellis and T. S. Virdee, Experimental Challenges in High Luminosity Collider Physics, Ann. Rev. Nucl. Part. Sci. 44(1994)609.
- [7] C. Joram, Particle Detectors, CERN Academic Training Programme, 1998.
- [8] G. Hall, Electronics at LHC, CERN Academic Training Programme, 1998.
- [9] P. Sphicas, Trigger/DAQ at LHC, CERN Academic Training Programme, 1998.
- [10] ATLAS Technical Design Reports, <http://atlasinfo.cern.ch/Atlas/GROUPS/Notes.html>
- [11] CMS Technical Design Reports, <http://cmsdoc.cern.ch/LHCC.html>
- [12] R. Wigmans, Ann. Rev. Nucl. Sci. and Part. Sci., **41**(1991)133.
- [13] D. Barney, Private communication.

- [14] D. Acosta et al., SPACAL, Nucl. Instr. and Meth., **A294**(1990)193.
- [15] D. Groom, To appear in Proc. of Intl. Conf. on Calorimetry in High Energy Physics, Tucson, 1998.
- [16] R. Wigmans, Nucl. Instr. and Meth., **A259**(1987)389.
- [17] G. Drews et al., Nucl. Instr. and Meth., **A290**(1990)335, and H. Tiecke (for ZEUS Calorimeter Group), Nucl. Instr. and Meth., **A277**(1989)42.
- [18] A. Beretvas et al., CMS TN/94-326 (1994).
- [19] R. Apsimon et al., Nucl. Instr. and Meth., **A305**(1991)331.
- [20] ALICE Technical Design Reports, <http://www1.cern.ch/ALICE/documents.html>
- [21] M. Hauschild et al., Nuc. Instr. and Met., **A314**(1992)74.
- [22] BaBar
- [23] J. Seguinot and T. Ypsilantis, Nucl. Instr. and Meths., **142** (1977)377.
- [25] F. Sauli, Techniques and Concepts of High Energy Physics, ed T. Ferbel, Vol. 11(1983)301, New York: Plenum.
- [26] D. Decamp et al., Nucl. Instr. and Meths. **A294**(1990)121.
- [27] A. Oed, Nucl. Instr. and Meths. **A263**(1988)351.
- [28] F. Sauli, Nucl. Instr. and Meths. **A386**(1997)531.
- [29] A. Annenkov et al., CMS NOTE 1998/041 and references therein.
- [30] G. Gratta et al., Ann. Rev. Nucl. Part. Sci. **44**(1994)453.
- [31] E. Auffray et al., Nucl. Instr. and Meth., **A412**(1998)223.
- [32] M. A. Akrawy et al., Nucl. Instr. and Meth., **A290**(1990)76.
- [33] D. Fournier, Nucl. Instr. and Meth., **A367**(1995)5.
- [34] D. Schinzel, Proc. of Intl. Wire Chamber Conference, Vienna, 1998.